Electro-mechanical Reliability of CNT-based Conductive Films on Flexible Substrates

Zur Erlangung des akademischen Grades
Doktor der Ingenieurwissenschaften
von der KIT-Fakultät für Maschinenbau des
Karlsruher Instituts für Technologie (KIT)

angenommene
Dissertation
von

M.Sc. Yuran Kang
aus Baoji, Shaanxi, China

Tag der mündlichen Prüfung:	31. Juli 2020
Referent:	Prof. Dr. Oliver Kraft
Korreferent:	Prof. Dr. Michael Hoffmann

Abstract

Conductive traces or films on flexible substrates are essential components in flexible electronic devices. They have to sustain electrical conductivity and mechanical integrity during external deformation. Conductive traces from conventional materials, such as ITO and metals, have exhibited limited reliability on flexible substrates under large strains.

In this context, carbon nanotubes (CNTs) could be a promising alternative material due to their outstanding mechanical, electrical, and thermal properties. A few studies have reported that CNT-based conductive traces on flexible substrates can sustain very large tensile strains. However, very few systematic studies regarding their electro-mechanical reliability have been conducted. This doctoral study is concerned with the electro-mechanical behavior of CNT-based conductive traces/films under static and cyclic deformation and systematically investigates the correlating mechanisms for their excellent reliability. These findings could be important for the development and optimization of potential flexible devices utilizing CNTs.

CNT-based conductive traces can be fabricated via inkjet printing or spin-coating. As one of the standard substrates for printed electronics, polyethylene terephthalate (PET) foils are used as polymeric substrates. Successful printing of CNT-based conductive traces has been achieved. However, the electrical conductivity is limited by the lower content of CNTs in the ink. Thus, for achieving better electrical conductivity, spin-coating of CNT dispersions has been adopted. By deposition of multiple layers, a sheet resistance as low as 400 Ohms/sq. for CNT-based conductive films has been achieved.

The most important part of this doctoral study is the static and cyclic electro-mechanical testing, as well as the microstructure characterization of CNT-based conductive films on flexible substrates. Micro-tensile tests with *in-situ* resistance measurements have been conducted to test their reliability under large tensile strains, whereas bending fatigue tests with *in-situ* resistance measurements have been performed to evaluate their reliability under cyclic tensile strains. In order to study the electro-mechanical behavior of CNT-based conductive films with applied mechanical strains, their surface morphology and microstructural changes before and after testing have been investigated by combining several microscopic characterization techniques, including scanning electron microscopy, focused-ion-beam microscopy, and helium ion microscopy.

CNT-based conductive films exhibit excellent reliability under large strains up to 50%, as demonstrated by micro-tensile tests. Their resistance-strain relationship showed that their intrinsic conductivities could even be improved by stretching. Their strainability up to 50% has benefited from the bridging effect of CNTs over eventually occurring local cracks. Bending fatigue tests further revealed very high lifetimes of CNT-based conductive films during cyclic bending fatigue. Under small strain amplitudes, such as 1% to 2%, the CNT-based conductive films are free of fatigue damage up to 1 million bending cycles, and their intrinsic conductivities are even improved during cyclic bending due to cohesion effect. For a higher strain amplitude of 3%, CNT-based conductive films can sustain their electrical conductivity up to 200,000 bending cycles, and their failure is only due to fatigue damage and total rupture of the polymeric substrate, which is found to be the bottleneck of the whole system. These results proved that the PET foils used in this study are not the optimal flexible substrates for bending conditions and alternative substrates, which will not fatigue and rupture at higher strain amplitudes (e.g. $> 3\%$), are required.

Kurzfassung

Leitfähige Bahnen oder Schichten auf flexiblen Substraten sind wesentliche Komponenten für die flexible Elektronik. Sie müssen bei äußeren Verformungen ihre elektrische Leitfähigkeit und mechanische Integrität erhalten. Leiterbahnen aus herkömmlichen Materialien wie Indiumzinnoxid (ITO) und Metallen haben auf flexiblen Substraten unter großen Dehnungen nur eine begrenzte Zuverlässigkeit gezeigt.

In diesem Zusammenhang könnten Kohlenstoffnanoröhren (CNTs) aufgrund ihrer hervorragenden mecha-nischen, elektrischen und thermischen Eigenschaften eine vielversprechende Alternative sein. Einige Studien haben berichtet, dass CNT-basierte Leiterbahnen auf flexiblen Substraten sehr großen Zugspannungen standhalten können. Es wurden jedoch nur sehr wenige systematische Studien zu ihrer elektromechanischen Zuverlässigkeit durchgeführt. Diese Doktorarbeit befasst sich mit dem elektromechanischen Verhalten von CNT-basierten Filmen bei statischen und zyklischen Verformungen und untersucht systematisch, die zugrundeliegenden Mechanismen für ihre hervorragende Zuverlässigkeit. Diese Erkenntnisse könnten für die Optimierung potenzieller flexibler Geräte unter Verwendung von CNTs wichtig sein.

CNT-basierte Leiterbahnen können durch Tintenstrahldruck oder Schleuderbeschichtung hergestellt werden. Als eines der Standardsubstrate für die gedruckte Elektronik wird eine Polyethylenterephthalat (PET)-Folie als Substrat verwendet. CNT-basierte Leiterbahnen konnten erfolgreich gedruckt werden. Die elektrische Leitfähigkeit ist jedoch durch den geringeren Gehalt an CNTs in der Tinte begrenzt. Daher wurde zur Erzielung

einer besseren elektrischen Leitfähigkeit eine Schleuderbeschichtung von CNT-Dispersionen angewendet. Durch eine mehrschichtige Abscheidung wurde ein Schichtwiderstand von lediglich 400 Ohm/sq. erreicht.
Der wichtigste Teil dieser Doktorarbeit sind die statischen und zyklischen elektromechanischen Prüfungen sowie die Mikrostrukturcharakterisierung von CNT-basierten leitfähigen Filmen auf flexiblen Substraten. Es wurden Mikrozugversuche durchgeführt, um ihre Zuverlässigkeit unter statischen Zugspannungen zu testen, während Biegeermüdungsversuche durchgeführt wurden, um ihre Lebensdauer unter zyklischen Zugdehnungen zu bewerten. Um das elektromechanische Verhalten von CNT leitfähige Filmen unter Verformung zu untersuchen, wurden ihre Morphologie und Änderungen der Mikrostruktur untersucht, indem verschiedene mikroskopische Charakterisierungsmethoden kombiniert wurden.
CNT leitfähige Schichte zeigen eine ausgezeichnete Zuverlässigkeit bei hohen Dehnungen von bis zu 50%. Ihre Widerstands-Dehnungs-Abhängigkeit zeigt, dass ihre intrinsischen Leitfähigkeiten durch Strecken sogar verbessert werden. Ihre Dehnbarkeit von bis zu 50% wird durch die Überbrückungswirkung von CNTs über eventuell auftretende lokale Risse begünstigt. Biegeermüdungstests ergaben ferner sehr hohe Lebensdauern der CNT Schichten. Bei kleinen Dehnungsamplituden, von 1% bis 2%, sind die CNT leitfähigen Schichten bis zu 1 Million Biegezyklen frei von Ermüdungsschädigung, und ihre intrinsischen Leitfähigkeiten werden sogar während der zyklischen Verformung aufgrund des Kohäsionseffekts verbessert. Bei einer höheren Dehnungsamplitude von 3% können CNT Schichten ihre elektrische Leitfähigkeit bis zu 200.000 Biegezyklen aufrechterhalten, und ihr Versagen ist nur auf die Ermüdung und den Gewaltbruch des Polymersubstrats zurückzuführen, was sich als der limitierende Faktor des ganzen Systems herausstellt. Diese Ergebnisse zeigten, dass die in dieser Studie verwendeten PET-Folien nicht die optimalen flexiblen Substrate für Biegebeanspruchungen sind und alternative Substrate, die bei höheren Dehnungsamplituden (z.B. > 3%) nicht ermüden und brechen, erforderlich sind.

Acknowledgement

This work has been carried out from Nov. 2013 to Jan. 2019 at the Institute for Applied Materials (IAM-WBM) of the Karlsruhe Institute of Technology (KIT) and has been conducted within the framework of the endowed professorship "Nanostructured Functional Materials" of Professor Oliver Kraft funded by the Bosch foundation. This doctoral thesis would not have been possible without the assistance, help, and support from a variety of people, whom I would like to thank heartily here.

First, I would like to give my sincere gratitude to my mentor Prof. Dr. Oliver Kraft for the provision of an interesting research topic, his great interest in my work and constant support during the past few years. Furthermore, I would like to thank Prof. Dr. Michael Hoffmann, who kindly agreed to be the second referee of my thesis and has evaluated my work.

Second, I would like to express many thanks to my supervisor Dr. Patric A. Gruber for his continuous passion and effort in guiding my work. This work and its output would not be possible without his creative ideas, inspirational inputs, and fruitful scientific discussions. Equally important, his vigorous guidance and patient encouragement have motivated me along this journey.

Further, I would like to thank heartily Dr. Joachim A. Binder, who has routinely supervised my work as well. Dr. Binder has also contributed a lot in supporting my work. He has coordinated many resources for providing me an excellent experimental environment. His supervision and helpful discussions have directly driven my progress.

Also, I am very thankful to Prof. Dr. Marc Kamlah for his strong support, and Mrs. Jana Herzog for her kind help and assistance. Their support for

many administrative issues has helped me a lot during the time at the institute.

In addition, my sincere thanks to many dear colleagues: Mrs. Margarete Offermann for her continuous help and support in the laboratory; Dr. Reiner Mönig for his support and discussions on the scanning electron microscopy (SEM) technique, *in-situ* tests inside SEM, and Raman spectroscopy; Dr. Ruth Schwaiger for her support and discussions on the focus-ion-beam and helium-ion-microscope techniques; Mrs. Daniela Exner for assisting me and solving many problems on operating different microscopes; Dr. Thomas Haas and Dr. Andreas Friedrich for their instructions on various experiment instruments and setups; Dr. Seol-Min Yi for his collaborative teamwork and fruitful scientific discussions during his postdoctoral time at IAM-WBM; Dr. Nilesha Mishra for her help, assistance, and excellent teamwork; Mr. Erwald Ernst for his responsive help and assistance on manufacturing mechanical parts; Dr. Heinz Riesch-Oppermann for helpful discussions. Their support has helped me with every little step on my way of pursuing a doctorate.

Last but not least, my thanks to many German friends who have supported me a lot over the past nine years: Family Fischer, Christina Fisher, Oliver Liegemann, and Melanie Liegemann. Their help has made my work and life in Germany a wonderful experience. I have experienced and learned a lot from Germany and its diverse cultures.

Finally, I would like to express my deepest gratitude to my family: my father Jianqiu Kang, my mother Ruiqiong Wang, and my sister Yukun Kang. They always have a strong belief in me and have given endless strength to me. Though we live in two nations, they have accompanied me along this journey.

Baoji, China in Jan. 2020 *Yuran Kang*

Contents

1 Introduction

Background

The human body and biological tissues are soft, elastic, and wavy, while traditional electronics tend to be stiff, rigid, and planar, resulting in a natural mechanical mismatch that limits the adaptability of these devices for everyday life and biological applications. This mechanical mismatch has inspired the creation of an emerging field - "flexible electronics" [1, 2].
Conventional electronics are based on rigid and stiff materials, e.g., integrated circuits (ICs) or printed-circuit-boards (PCBs), whereas flexible electronic components are fabricated on compliant substrates. Though conventional electronics excel in running speed and performance, flexible electronics can enter new application fields, which require flexibility and adaptability. This merit is not achievable by conventional electronics. Therefore, the goal of flexible electronics is not to replace conventional electronics but to create a much broader application spectrum compared to conventional electronics.
As one of the most exciting and most promising information technology, flexible electronics have attracted full attention from academia and industry in the last decade. Making a uniform definition of flexible electronics is challenging. However, flexible devices have several key features in common:

1. Flexible electronics rely on flexible and compliant substrates. Organic polymers are the main substrate material of most flexible electronic devices. Their compliance enables the deformability of the device,

and deformation modes can be bending, rolling, folding, and stretching.

2. Flexible electronics need adaption and further development of existing fabrication technologies. Many fabrication technologies used in flexible electronics were initially borrowed from established semiconductor processes, such as those used to manufacture silicon-based thin-film transistors. The high temperature ($> 120\,^{\circ}\mathrm{C}$) and low pressure ($< 1 \times 10^{-6}\mathrm{Pa}$) conditions from those technologies are not always compatible with polymeric substrates. These limitations have promoted the combination of semiconductor processes and printing technologies, such as those used to manufacture thin-film conductive electrodes or light-emitting diodes (LEDs). Thereby, flexible electronic components can be patterned digitally by the inkjet (IJ) printing technique or fabricated in large-area by roll-to-roll (R2R) processes.

3. No matter the flexible devices are made of organic or inorganic materials, active or passive components, they need to perform without significant degradation during static and cyclic deformation such as bending, folding, and stretching. These requirements demand that also the functional materials should exhibit excellent mechanical durability without losing their electrical properties. This coupled property is termed as electro-mechanical reliability.

In recent years, flexible electronics have developed along two technological routes. The first is in the flexible domain, in which electronic components could maintain their electrical properties up to strains of about 10%. The second route goes beyond flexibility and extends further to the stretchable domain, in which the device should sustain strains more than 50% or even up to 400%. The progress in these two areas is enabling the innovation of Human-Machine-Interface (HMI) [1, 2]. Regardless of the function, one of the fundamental electrical components are the electrical connections within

these devices. The electrical connections are often made in a planar structure and are termed as "conductive traces" or "conductive tracks". For consistency, "conductive trace" is used throughout this dissertation.

Materials that are suitable for fabricating flexible conductive traces are gaining more and more importance. Conventional conductive oxides, such as indium-tin-oxide (ITO), are not suitable due to their brittleness and limited flexibility. Strainable alternatives for ITO include metallic nanomaterials such as silver nanoparticles and silver nanowires as well as carbon nanomaterials, including carbon nanotubes and graphene. Conductive traces fabricated using silver nanoparticles [3] and silver nanowires [4, 5] exhibited excellent electrical conductivity. However, their maximum application strain and lifetime during cyclic deformation is not fully exploited yet. The incorporation of CNTs into conductive traces exhibited further advantages. For example, CNTs have been added into silver nanoparticle dispersions to enhance the mechanical resilience against substantial stretching, or CNTs have been embedded into elastomers to make stretchable sensors that could endure strains up to 300% [6, 7]. In addition, CNT-based devices show less deterioration during fatigue.

Fewer systematic studies have been performed for understanding the electromechanical reliability of CNT-based conductive traces/films on flexible polymeric substrates, and the correlating deformation mechanisms within the CNT network of CNT-based conductive traces/films are not fully understood.

Scope and goals of this study

The goals of this study are targeted as follows:

1. Review on previous experimental and theoretical work related to this study, report of the state-of-the-art on this topic and its newest progress, and definition of a fundamental basis for this doctoral thesis.

2. Fabrication of CNT-based conductive traces and thin-films on polymeric substrates by inkjet printing and by conventional solution processes such as spin-coating.

3. Investigation of the electro-mechanical behavior of CNT conductive traces and thin-films by uni-axial micro-tensile tests, characterization of the morphological and microstructural evolution, and understand possible failure mechanisms under substantial tensile loading.

4. Investigation of the electro-mechanical reliability of CNT conductive traces and thin-films by bending fatigue tests, characterization of the microstructural changes, and identification of the fatigue mechanism during cyclic loading.

2 State-of-the-art

2.1 Strategies for flexible electronics

As the name implies, flexible devices should be compliant, flexible, and conformable. The conformable range for flexible devices is broad: from flexible to stretchable. Each domain corresponds to different deformation behavior for a flexible electronic device. The term "flexible" usually refers to the bendability and foldability of planar structures, whereas the term "stretchable" usually refers to an ideal elasticity of planar structures. Different deformation modes such as bending, folding, twisting, and stretching can lead to deterioration in the electrical performance of the device [8].

Architecture of flexible devices

An ideal strategy to achieve a fully flexible (stretchable and conformable) device is to enable the electronic components themselves to be intrinsically flexible: materials used for the electronic circuits should possess the ability to maintain proper electrical function during mechanical deformation. In reality, this is very challenging to achieve, because different components, active, passive, and underlying substrates consist of different materials. Those who are good at carrying electronic functionality are not intrinsically soft and elastic, but rather stiff and rigid. In contrast, those who are compliant, soft, and stretchable are intrinsically insulators [9].
The common strategies to endow electronics with the capability of large deformation are divided into two main groups. The first group involves optimizing structural and mechanical designs: (1) isolating the active com-

ponents from a large external strain by rigid island designs (island-bridge structure), (2) fabricating interconnects into tortuous shapes (in-plane), (3) making electronic components in a buckled pattern using surface instability (out-of-plane), and (4) fabricating the material into a stretchable structure [10–16]. The essential concept of these strategies is to reduce the maximum strain, which is imposed in metallic or ceramic materials. The second group involves utilizing ductile materials or polymer matrices: (5) direct use of flexible conductive materials (mostly nanomaterials), and (6) embedding of conductive materials into elastic matrices as composites [8].

Flexible substrates

The flexibility of flexible devices is endowed mainly by the compliance of underlying substrates. When the substrates are thin enough and stretchable, they can also reduce the mechanical mismatch between biological tissues and electronic devices. The main polymeric materials for flexible electronics are polyimide (PI or Kapton®), polyethylene terephthalate (PET), polyethylene naphthalate (PEN), while polymers such as polycarbonate (PC), poly(ether sulfone) (PES), and polyacrylate (PAR) have also been reported [6, 17–21]. These thermoplastic polymers are excellent substrates for electronic devices due to their good mechanical properties, easy handling and processing as well as high resistance to oxygen and water penetration [20]. If higher stretchability (100%-400%) of the substrate is required, elastomers such as poly(dimethylsiloxane) (PDMS), Ecoflex®, polyurethane (PU/TPU), and multiblock copolymer styrene-ethylene-butadiene-styrene (SEBS) can be used [18, 22, 23]. Papers and textile fabrics are also important substrates for low-cost devices and wearable electronics.

The main challenge in using polymers as substrates for flexible electronics is their low thermal stability. The glass transition temperature (T_g) of most common polymer film is less than 150 °C, e.g. 60-80 °C for PET, 120-125 °C for PEN, and 140-150 °C for PC. An exception is PI with T_g in the

range of 310-365 °C. The selection of the substrate is determined by the requirement of the target application, the strain range, and the fabrication routes for functional materials.

Flexible conductive materials and traces

Among different components for building flexible electronic devices, conductive traces are one of the most critical and ubiquitous building blocks. Conductive traces are electrodes connecting two or more terminals between different active or passive components in an electrical device. Often, they are also called thin-film electrodes (TFEs), since they are fabricated in a planar thin-film geometry. Flexible conductive traces have to combine flexibility with high electrical conductivity. In other words, they have to sustain their electrical conductivity and mechanical integrity under different mechanical deformations, such as bending, rolling, and stretching. However, damages could form in the conductive traces under these deformations and could further lead to malfunction or complete failure of a flexible device. Thus, the electro-mechanical reliability of conductive traces on flexible substrates is critical for the reliability of the flexible device.

Conventionally, conductive traces are fabricated using bulk materials, such as conductive oxides or metals. However, intrinsic poor mechanical ductility of these materials limits their application as flexible conductive traces. Conductive oxides, such as indium-tin-oxide (ITO), would fail at less than 2% of strain [24]. Thin metallic films on polymer substrates usually rupture at strains of about 10% [25]. In recent years, many research efforts have been devoted to developing alternative conductive materials that could survive substantially higher strains. Alternative candidates include metal grids (MG), metallic nanowires (MNWs), metallic nanoparticles (MNPs), intrinsically conductive polymers (ICPs), carbon nanotubes (CNTs) [26] and graphene [27]. These materials are compared in Table 2.1 [28].

Table 2.1: Strengths and weakness of conductive trace materials

Conductive materials	Conductivity	Flexibility	Printability	Stability	Color	Haze	Stretchability
Conductive oxides (e.g. ITO)	++	–	–	++	–	++	–
Metallic grids (e.g. Ag grids)	++	oo	++	++	++	oo	–
Metallic nanoparticles (e.g. AgNPs)	++	oo	–	++	++	–	–
Metallic nanowires (e.g. AgNWs)	++	++	+	++	++	oo	+
Conductive polymers (e.g. PEDOT: PSS)	oo	++	++	–	–	++	oo
Carbon nanotubes (CNTs)	oo	++	++	++	++	++	++

++ : excellent **oo** : good **–** : poor

With their excellent electrical properties and their outstanding mechanical properties, CNTs have been widely envisioned as ideal building blocks for high-performance engineering materials. CNTs can be compressed or can be stretched to large strains.

Recent studies have shown that conductive traces based on CNTs show superior mechanical performance in comparison with other material systems [29–32]. For example, compared to evaporated metallic film or printed metallic NP or NW films, CNT-based conductive films show notably advantages. It has been shown that incorporating a few percents of CNTs into AgNP film as reinforcement can enhance the mechanical performance of AgNP film under cyclic deformation [29, 33]. Several groups have demon-

strated strain sensors [22, 34–36] in which the conductive traces are fabricated using SWCNTs, which can sustain very large strain (100% to 280%) without degrading their performance. However, due to the use of SWCNTs, high cost and complicated processing impede large scale production.
In this study, MWCNTs are chosen due to their low-cost and higher availability, which is more favored for large scale production, such as for solar panels [37]. However, one disadvantage of MWCNTs is their lower intrinsic conductivity. Typical methods to overcome this drawback is to apply multi-pass processes, for example, S. Azoubel *et al*. [38] has inkjet-printed MWCNTs with multiple-layers as conductive electrodes on PET substrates, which possess an excellent electrical conductivity.

2.2 Solution processing of CNTs

Structure and properties of CNTs

Many unique and superior properties of CNTs have been discovered since 1991 [26] (Table 2.2). This class of materials is an excellent alternative to metal NPs and metal NWs for flexible electronics.

Table 2.2: Properties of carbon nanotubes

Type of CNT	SWCNTs: metallic or semiconducting (p-type), MWCNTs: metallic
Mechanical properties	High elastic modulus: 1 to 5 TPa, very high tensile strength: 10 to 100 GPa [39–42]
Electrical properties	High current density: $10^9 A/cm^2$ vs. $10^7 A/cm^2$ for Copper, very high charge carrier mobility
Thermal properties	High thermal conductivity: 2000 W/mK at room temperature vs. 400 W/mK for Copper at room temperature
Chemical properties	large aspect-ratio (around 1000), hydrophobic, non-polar

CNTs have a tubular structure composed of carbon atoms. The basic structure of a CNT can be imagined by rolling up and closing a graphene sheet [27]. In other words, CNTs can be theoretically characterized as a graphene sheet appropriately rolled into a cylinder along a direction with essentially sp^2 atomic bonding structure between the nearest neighbors. This direction is described by the roll-up vector: $c_h = na_1 + ma_2$ (Fig. 2.1(a)), which connects the crystallographically equivalent sites on a two-dimensional graphene sheet, where a_1 and a_2 are the graphene lattice vectors, and n and m and integers.

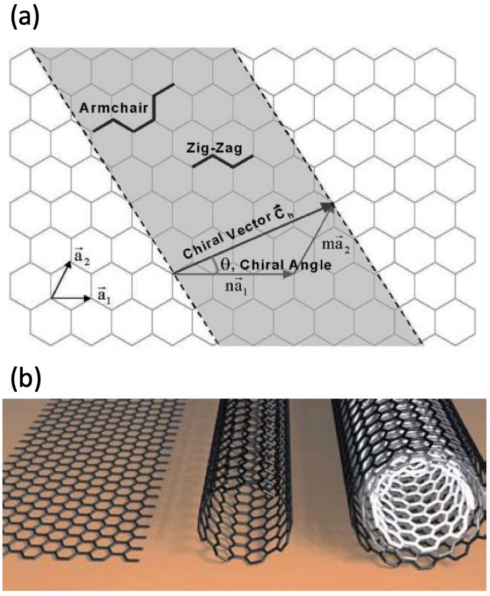

Figure 2.1: Schematic diagram illustrating (a) how a hexagonal sheet of graphene is "rolled" to form a carbon nanotube, the chiral vector indicates the rolling direction; (b) from left to right: the atomic structure of a graphene sheet, a single-walled carbon nanotube (SWCNT), and a multi-walled carbon nanotube (MWCNT) (Adapted from Reference [43]).

CNTs can be metallic or semiconducting [44, 45] depending on their diameter, chirality, and helicity of the arrangement of graphitic rings at their walls. Individual metallic CNTs have intrinsic electrical resistivity close to the resistivity of metals ($10^{-6}\Omega cm$ for SWCNT [46] and $3 \times 10^{-5}\Omega cm$ for MWCNT [47]). However, in most cases, due to the presence of various defects or impurities formed during the CNT synthesis, the resistivity of individual CNTs, and the resistivity of their assemblies (in bulk or thin-films) is much higher [48]. Diameters of SWCNT and MWCNT are in the range of 0.4-4 nm and 1-100 nm, respectively, and their length can be from less than a micron up to 1 mm [45, 49, 50].
The primary methods to produce CNTs are arc-discharge [51,52], laser ablation [53,54], chemical vapor deposition (CVD) from hydrocarbons [55,56], as well as gas-phase catalytic growth from carbon monoxide [57]. After production, a purification process is necessary in order to remove various impurities in the form of catalyst particles, amorphous carbon, and non-tubular fullerenes.

Fabrication of CNT thin-films

Coating techniques

Flexible electronics have received substantial attention as a potential application of printing technologies. A variety of printing technologies can fabricate conductive films and components [58]. The specific printing technique has to be chosen based on the desired property of the functional nanomaterial, requirements for the ink formulation, the pattern geometry, and the choice of substrate.
Two fabrication routes were mainly used in this work. Inkjet-printing offers flexible patterning capability and high lateral resolution (linewidth: 20-70 µm), while spin-coating enables coating of CNT films on PET substrates in a large-area (up to 30 cm^2). Inkjet-printing technology is most typically classified as either continuous (CIJ) or drop-on-demand (DOD). As the name

implies, continuous inkjet technology ejects drops continuously [59]. These drops are then either directed to the substrate or a collector for recirculation and reuse. Drop-on-demand technology ejects droplets only after excitation [60–62], and comprises thermal inkjet and piezoelectric inkjet. In thermal inkjet technology, drops are formed by rapidly heating a resistive element (to 350-400°C) in a small chamber. In piezoelectric inkjet technology, a piezo crystal (commonly lead zirconium titanate) undergoes deformation when an electric field is applied, and this deformation can mechanically create a pressure pulse that causes a drop to be ejected from the nozzle. Thermal inkjet is mostly used in consumer printers, whereas piezoelectric inkjet is the current choice for printing functional materials. Thus, the piezoelectric inkjet is chosen for this work.

Formulation of CNT dispersions

In solution-chemistry, a dispersion usually denotes a system in which particles are dispersed in a liquid phase of a different composition. Once several critical properties of a dispersion meet the requirements of a specific printing technique, a dispersion can be denoted as an ink. The composition of an ink consists typically of filler, binder, additives, and solvent. Metal NPs, metal NWs, CNTs, conductive polymers, and graphene flakes can all be considered as fillers.

For a CNT dispersion, CNTs must be evenly dispersed in a liquid phase through mechanical mixing [63]. Dispersing CNTs is challenging due to the high van der Waals forces between CNTs and their hydrophobicity. Besides, the high aspect ratio of CNTs makes them prone to aggregation and entanglement. From the perspective of inkjet printers, the high aspect ratio of CNTs is problematic, because it is required to limit the CNT length in order to avoid clogging of the printhead nozzle [6, 64]. All these factors have made the formulation of CNT inks challenging.

Physical and chemical dispersing have been used to disperse CNTs. The most common method is ultrasonication, which generates high-frequency vibrations to de-bundle and separate CNT within a liquid. Depending on the need, three different types of sonicators are used: bath, tip, and cup-horn sonicators. Bath sonication is the gentlest form of sonication and does not cause as many sidewall defects, whereas tip or cup-horn sonicator can be far more powerful at de-bundling the CNTs. Sonication can shorten CNTs and damage the sidewalls, so sonication power and time must be chosen carefully. Furthermore, the choice of solvent also affects the sonication power and time, which can influence the dispersion quality and stability.
Chemical dispersion includes both the covalent method and the non-covalent method [63, 65–72]. In covalent methods, the solubility of CNTs in the solvents is improved by chemical functionalization with various chemical agents. By functionalizing the sidewalls with hydrophilic groups such as carboxylic acid, amide, polyethylene glycol, and poly amino benzene sulfonic acid, stable water-based CNT-inks can be prepared [63, 65]. In non-covalent methods, surfactants and polymers are widely applied. The solubility of CNTs in aqueous or in organic solvents can be rendered by the adsorption of surfactants and polymers onto the nanotube surface. The most commonly used surfactants include sodium-dodecyl-benzenesulfonate (SDBS) [66], dodecyl-trimethylammonium-bromide (DTAB) [67], hexadecyltrimethylammonium bromide (CTAB) [68], octyl phenol ethoxylate (Triton X-100) [69, 70], sodium dodecyl sulfate (SDS) [69, 71, 72]. Generally, surfactants should be removed after depositing due to their insulating nature. They can be removed easily by washing with deionized water. The stability of dispersions can be characterized by the zeta-potential and fluidic parameters [73–76].

Ink requirements for inkjet printing

The most important parameters for determining if an ink is printable (or jettable) are the particle size and the rheological properties. It is essential to avoid particle clogging during the printing process. As a thumb of rule, the average particle size should be less than one-hundredth of the printhead's nozzle diameter to ensure smooth and continuous printing [6]. The rheological properties such as viscosity, density, and surface tension dictate the printability of an ink, affect the size and shape of the deposited droplets and determine the wetting on the substrate and the presence of satellite drops. The viscosity of the ink must be low enough to allow the refill of the ink reservoir and the expulsion of droplets out of the nozzle. The surface tension must be high enough to inhibit unwanted dripping from the nozzle but low enough such that the ejected droplet can break away from the nozzle. Generally, the recommended values of the two properties for most inkjet printers are: the viscosity should be within the range of 1-18 $mPa{\cdot}S$ [77–80], and the surface tension should be between 20-70 mNm^{-1} [77–80].
The printability (or jettability) of an ink can be determined using the dimensionless Reynolds (*Re*), Weber (*We*), and Ohnesorge (*Oh*) numbers. The *Reynolds* number *Re* is the ratio of the inertial forces to the viscous forces:

$$Re = \frac{\rho V L}{\eta}, \tag{2.1}$$

the *Weber* number *We* is the ratio of the inertial forces to the surface tension forces:

$$We = \frac{\rho V^2 L}{\sigma}, \tag{2.2}$$

and the *Ohnesorge* number *Oh* describes droplet formation and is the ratio of the viscous forces to the surface tension and inertial forces:

$$Oh = \frac{\sqrt{We}}{Re} = \frac{\eta}{\sqrt{L\rho\sigma}}. \tag{2.3}$$

The parameters ρ, η, σ, L, V represent the density, viscosity, surface tension, characteristic length (typically nozzle diameter) and droplet velocity, respectively.

The Z number ($Z = 1/Oh$), which is the reciprocal of the Ohnesorge number, is commonly used to describe printability. When the Z number is between 1 and 10, a stable droplet formation could be expected [81, 82]. At a lower value of Z, viscous dissipation prevents drop ejection, whereas, at a higher value of Z, the primary drop would be accompanied by a large number of satellite drops. Thus, by adjusting the ink composition, the We and Re numbers can be tailored so that the Z number falls inside the printable window, as shown in Figure 2.2. The validity of this approach has been demonstrated for a variety of inks [82].

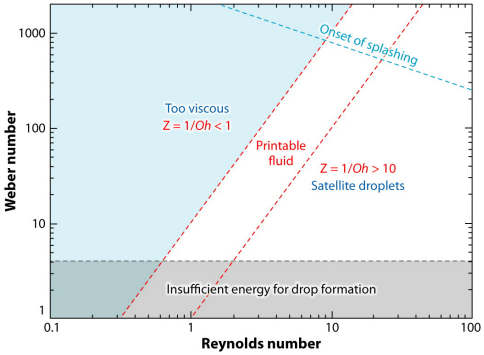

Figure 2.2: Plot of Weber number versus Reynolds number to illustrate the printing window in which printable fluids can be expected (Adapted from Reference [82]).

Post-printing sintering

Usually, a post-printing step has to be conducted to remove the insulating materials such as stabilizers and organic additives that are present in the ink. Such removal can be achieved by de-composition, desorption, or evaporation of the organic material. As a result, the contacts between the particles in the printed layers can be enhanced. For metallic nanoparticles, they need to be sintered in order to form a continuous metallic film with conductivity close to that of the bulk metal [8].

The conventional sintering methods are thermal sintering, where the printed materials are annealed at elevated temperatures. This method is very effective for welding metallic nanoparticles. High surface-to-volume ratio and enhanced self-diffusion of surface atoms at metal NPs result in a drastic decrease in their melting point [83, 84] and it is possible to weld metal NPs at temperatures much lower than the melting point of the bulk metal, typically 250-350 °C [6, 17, 19, 85]. Since most flexible substrates are heat-sensitive and cannot withstand temperatures higher than 150 °C, the current development of sintering techniques focuses on further reducing the sintering temperature.

A promising alternative to thermal sintering is photonic sintering. Photonic sintering utilizes flash lamps, lasers, and other light sources to deliver energy to the target material. It can be classified according to the wavelength range: ultraviolet (UV), visible (intense photonic flash), and infrared (IR) [6, 17, 19, 85]. Photonic sintering induces heat to the surface layer of the printed NPs, and the heat transfer from the surface leads to sintering of the underlying NPs. Precise control of the amount of delivered energy and the duty cycle of the light sources results in the effective sintering of printed materials without destructing the underlying substrates. Other unconventional sintering techniques are plasma [86], microwave [87], electron beam (e-beam) [88] and chemical sintering [89].

Printed CNT patterns or films usually do not require annealing for obtaining high electrical conductivity [90]. It is usually sufficient to heat the printed CNT layer to about 100 °C, so that the organic additives/solvent can evaporate. To reduce the resistance of CNT films further, post chemical treatment by rinsing nitric acid onto CNT films or dipping CNT films inside nitric acid can be applied [91].

2.3 Mechanics of thin-films on compliant substrates

Deformation and failure modes

Interfaces exist intrinsically between films and substrates, and they are susceptible to external mechanical strain. Different failure modes can occur due to the mechanical strain induced by different deformation modes. Flexible electronic components on polymer substrates are often deformed by bending. When a sheet of film and substrate is bent, its two sides are subjected to different types of strain (Fig. 2.3). Tensile strains develop on the convex side, while compressive strains occur on the concave side. This may cause two different failure modes: cracks can form and propagate in the film under tension [24, 92], while delamination from the film/substrate interface tends to occur under compression (or with poor adhesion) [93].
Suo *et al*. [94] have derived a formula based on the beam theory for film-on-foil electronics that considers the elastic properties of both materials:

$$\varepsilon = \pm\left(\frac{d_s + t}{2r}\right)\left(\frac{1 + 2\eta + \chi\eta^2}{(1+\eta)(1+\chi\eta)}\right) \tag{2.4}$$

where d_s is the substrate thickness, t is the film thickness, $\eta = t/d_s$, and $\chi = Y_t/Y_s$. Moreover, η is used to define the ratio between the thickness of film and substrate, and χ describes the ratio between Young's moduli of film and the substrate, respectively. Assuming that Young's moduli of film

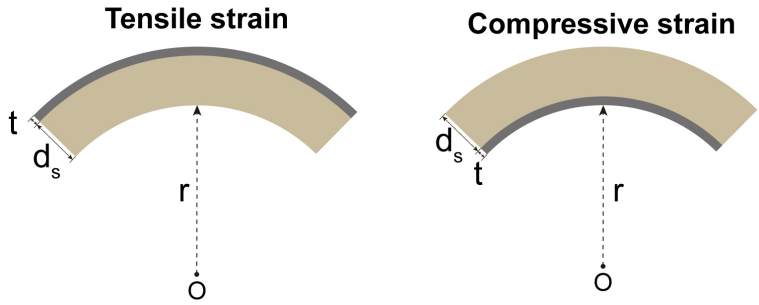

Figure 2.3: Schematic of a thin-film under tensile strain and compressive strain. The film thickness and the substrate thickness are denoted by t and d_s, respectively, whereas the bending radius is denoted by r.

and substrate are equal ($\chi = 1$) and the substrate thickness d_s much higher than the film thickness t ($\eta = 0$), equation 2.4 can be simplified:

$$\varepsilon = \pm\left(\frac{d_s + t}{2r}\right) \tag{2.5}$$

Based on equation 2.4 and 2.5, it is clear that thinner substrates yield lower peak strain at a given bending radius. Therefore, it is preferred to use thinner substrates because they allow for smaller bending radii prior to failure.

Electro-mechanical behavior under tension

Though flexible components are usually deformed by bending, they can also suffer from monotonic tensile strain in many situations, such as being mounted on a curved surface or being stretched during service. Under these conditions, the electrical property of a conductive thin-film, specifically, its total resistance can vary upon straining. This variation of resistance is usually called the relative change in resistance or fractional resistance, and can be theoretically calculated for bulk films based on the lateral changes of the film.

Given a conductor with the length L, width W, and thickness T, the electrical resistance is defined as follows:

$$R = \rho \times \frac{L}{A} = \rho \times \frac{L}{W * T}, \tag{2.6}$$

where ρ is the resistivity of the tested material (e.g. metallic thin-film or CNT thin-film).

As long as no fracture occurs, it can be assumed that the resistivity ($\rho = \rho_0$) and the total volume of the film ($AL = A_0 L_0$) remains constant during tensile loading. Under this assumption, the relative change in resistance is [95]:

$$\frac{R}{R_0} = (\frac{L}{L_0})^2. \tag{2.7}$$

The above expression is also known in a different form. By normalizing the resistance change to zero for the unloaded state and inserting the technical strain, the relationship between the fractional resistance ($\frac{\Delta R}{R_0}$) and the technical strain can be calculated:

$$\frac{\Delta R}{R_0} = \frac{R - R_0}{R_0} = \varepsilon_{tech} \times (\varepsilon_{tech} + 2). \tag{2.8}$$

The above theoretical prediction applies typically for homogeneous bulk materials, such as bulk metals. It has been reported in the work of J. Vlassak *et al*. that the increase in fractional resistance of a sputtered Cu thin-film on a PI substrate agrees well with the theoretical prediction described by equations 2.7 and 2.8 before cracking occurs [95]. However, at larger strains, the increase in fractional resistance deviates from the theoretical prediction. This deviation results from the debonding of the Cu thin-film and subsequent crack formation and propagation in the Cu thin-film due to its poor adhesion on the PI substrate. It has been further shown that if a Cu thin-film is deposited on a PI substrate with a Cr interlayer, the adhesion between the Cu thin-film and the polymer substrate can be significantly improved. Benefited from the good adhesion, the deformation in the Cu

thin-film at a large strain is thereby delocalized. As a result, the Cu thin-film can be stretched to a larger elongation with little debonding or local thinning, preventing the formation of cracks. Correspondingly, the increase in fractional resistance of the Cu/Cr/PI specimen has followed well along the theoretical prediction [95]. In the previous doctoral study from T. Haas, the fractional resistance of the inkjet-printed AgNP film on PET increases according to equation 2.8 at the beginning of the tensile test [30]. If cracking occurs, the relationship between fractional resistance and strain can not be described by equation 2.8 anymore, and the increase in fractional resistance deviates from the theoretical prediction. It has been reported that the increase in fractional resistance of inkjet-printed metallic thin-films is significantly lower than that of the evaporated metallic thin-films [30]. This property is important for improving the electro-mechanical reliability under large strains. Moreover, this property is mostly controlled by the fracture behavior of different metallic thin-films.

The relationship between the piezoresistivity and strain can also be described by:

$$\frac{\Delta R}{R_0} := k * \varepsilon, \tag{2.9}$$

where k is a coefficient, and ε is the applied mechanical strain. By rewriting equation 2.9, it is clear that k represents the ratio between relative change in electrical resistance to the applied mechanical strain. This ratio is termed as "gauge factor (GF)":

$$k = \frac{\frac{\Delta R}{R_0}}{\varepsilon} = GF. \tag{2.10}$$

GF can be de-composed further based on the definition of electrical resistance [96]:

$$GF = \frac{\frac{\Delta R}{R_0}}{\varepsilon} = \frac{\frac{\Delta \rho}{\rho_0}}{\varepsilon} + 1 + 2\upsilon, \tag{2.11}$$

where $\Delta\rho$, ρ_0 and υ denote the relative change of resistivity, the initial resistivity, and the Poisson's ratio, respectively. For a homogenous material, e.g., a metallic film, its resistivity is constant; therefore, $\Delta\rho = 0$, and GF is given by:

$$GF = \frac{\frac{\Delta R}{R_0}}{\varepsilon} = 1 + 2\upsilon. \tag{2.12}$$

Under large strains, the fracture behavior of thin-films plays an essential role in affecting the fractional resistance. Metallic thin-films supported by polymeric substrates exhibit an entirely different fracture behavior under tensile load than free-standing metallic films, due to the small film thickness and the confinement of the substrate [95]. Metallic films, which are not supported by polymeric substrates, will form local necks and cracks and thereby fail at smaller strains (usually <10%). For metallic thin-films on polymeric substrates, necking is constrained by the adhesion to the substrate, and cracking is retarded. When a tensile strain is induced to a thin-film on a compliant substrate, cracks can channel through the film. Channel cracking is often observed for stiff films of metals and ceramics. ITO films often fail at 1%-2% of tensile strain by channel cracking [24, 97]. For larger strains, evaporated metallic thin-films on polymer substrate can also fail by channel cracking. Even nanoparticular silver (AgNPs) films can fail by channel cracking [30]. For CNT thin-films, the assumption of constant volume may not apply anymore, because CNT thin-films consist of loosely packed CNT networks. Unlike bulk metallic thin-films, the fracture behavior of CNT thin-films may differ from that of metallic thin-films on compliant substrates. These microstructural differences have raised four questions: (1) how would the microstructure of the CNT network change upon straining? (2) how would the resistance of the CNT film develop during straining? (3) Is there any damage formation in the CNT network? (4) What is the failure strain of the CNT thin-films, and what is the failure mechanism? These interest-

ing questions on the electro-mechanical behavior of CNT-based conductive thin-films have motivated this doctoral study.

Fatigue of thin-films on polymer substrates

In practical applications, conductive films and traces in flexible devices are not only subjected to monotonic loading but rather to cyclic loading. With an increasing number of cyclic loading, conductive thin-films could fatigue and finally fail in different ways.

Fatigue is the time-dependent deformation of a material due to cyclic loading [98]. Fatigue failure can occur in ductile, brittle, and non-crystalline materials. Since the mechanical properties of thin-films differ from their bulk counterparts [99–101], their fatigue behavior cannot be simply extrapolated from the test data of the bulk material [102]. Fatigue of metallic thin-films has been studied by several groups [102–105]. However, fatigue of conductive thin-films fabricated from metallic and carbon nanomaterials, such as AgNPs, AgNWs, and CNTs, has not yet been studied systematically.

The reliability of conductive thin-films is affected mainly by its fatigue behavior, and can be described by the fatigue lifetime (or cycle lifetime), which is usually denoted by N_f. N_f can be defined in two ways: pure mechanically and electro-mechanically. Pure mechanically, N_f is defined as the number of cycles until fracture for different strain amplitude $\frac{\Delta\varepsilon}{2}$, which is the same as the criterion used in assessing the fatigue lifetime of bulk materials. Electro-mechanically, the reliability of conductive thin-films can be described by a criterion that is based on the change in resistance. Because the resistance change of thin-film reflects a change in the microstructure of the thin-film, it can be used as the fatigue failure criterion [105]. A failure criterion line, which corresponds to a specific fractional resistance value, can be considered as the onset of damage formation during fatigue cycles. However, at the beginning of studies on fatigue behavior of metallic thin-films, they were

not targeted at the applications of flexible conductive electrodes and traces, so their lifetime N_f is most often described pure mechanically.

The fatigue behavior of metallic thin-films supported on polymer substrates differs significantly from bulk metals and freestanding thin-films. Due to the size effect for the strength of thin-films, the dislocation plasticity is reduced, and the formation of fatigue damage in the form of extrusions and intrusions are suppressed [106, 107]. Besides, the supporting polymer substrates prevent strain localization and crack formation [102, 105]. Because of these two characteristics of metallic thin-films on polymer substrates, their lifetime is generally extended and is always higher than that of bulk materials and freestanding thin-films. It has been reported that metallic thin-films on polymer substrates showed an improved lifetime up to 1×10^5 cycles at a lower strain amplitude of less than 1%. These metallic thin-films include sputtered Cu thin-films on PI [102], thin-film Cu traces on a PCB [108], evaporated Ag thin-films on PET [105] and evaporated Cu thin-films on PI [109]. At a higher strain amplitude of larger than 1%, the fatigue lifetime of these thin-films is lower than 1×10^4 cycles because of the high stress amplitudes in these thin-films. At an even higher strain amplitude: e.g., 2%, the fatigue lifetime of these metallic thin-films is further reduced. This is because at a higher strain amplitude, due to the size effect, the stress amplitude in metallic thin-films is higher than that in bulk metallic films at the same applied strain amplitude. Thus, the fracture stress in metallic thin-films can be reached earlier, resulting in their failure at lower fatigue cycles.

The fatigue behavior of thicker metallic films ($t > 200nm$) and thinner metallic films ($t < 200nm$) should be differentiated. Generally, the grain size in metallic thin-films is proportional to the film thickness due to the fabrication process. As the film thickness increases, the grain size also increases, and vice versa. For thicker metallic films ($t > 200nm$) on polymer substrates, they exhibit a ductile failure. Due to the higher thickness and grain size effect, their strength is lower than that for the thinner metallic films. A certain degree of plastic deformation is still possible, extrusions

and intrusions can still form, and subsequent crack initiation and propagation can occur, leading to a ductile failure of the thicker metallic films [105]. In the failure process of thicker metallic film, delamination from substrate and strain localization is involved [105]. Thinner metallic films ($t < 200nm$) on polymer substrates exhibit a brittle failure. Due to the lower thickness and grain size effect, their strength is much higher than that for the thicker metallic films. The plasticity of dislocation in thinner metallic films is strongly suppressed so that extrusions and intrusions can no longer form. Thus, thinner metallic films can endure much higher cycles than thicker metallic films, and their lifetime is further extended than that of thicker metallic films. However, when the strain amplitude is high enough, the stress amplitude in thinner metallic films is much higher than that in thicker metallic films. As a result, cracks at defects and grain boundaries can form immediately, leading to a brittle fracture [102, 110–112]. In the failure process of thinner metallic film, delamination from the substrate is not involved [105, 113]. No matter for thinner or thicker metallic films, when the strain amplitude is high enough, the corresponding stress amplitude is increased so that the fracture stress is quickly reached, resulting in abrupt failure of metallic thin-films. However, good adhesion between the metallic thin-film and the polymer substrate can improve fatigue lifetime for both ductile and brittle metallic thin-films [105]. Good adhesion makes it difficult to induce delamination at the film-substrate interface and to localize plastic deformation. Thus, strain localization and local thinning in the thin-film is retarded, so local crack formation and propagation are inhibited. As a result, metallic thin-films with good adhesion can endure much more fatigue cycles than those with poor adhesion, and their fatigue lifetime is thereby extended.

In structural applications, the fatigue lifetime of the component material is strength-oriented and stress amplitude-controlled. However, in the application of flexible electronics, the fatigue lifetime of the conductive traces and thin-films is deformation-oriented and strain amplitude-controlled. Conduc-

tive traces and thin-films do not have to sustain very high stress for many fatigue cycles. Instead, they have to sustain a specified strain amplitude for a pre-defined fatigue lifetime since they will be deformed at this strain amplitude cyclically. In other words, for satisfying the requirement of flexible devices, not only a pre-defined high lifetime of conductive traces/thin-films should be guaranteed, but also a higher strain amplitude should be sustained. The secret of ensuring the electro-mechanical reliability of conductive traces and thin-films lies not only in extending the fatigue lifetime but also more in sustaining a higher fatigue strain amplitude for the whole film/substrate system. Though metallic thin-films can exhibit significantly prolonged lifetime ($N_f \cong 1 \times 10^5$) at a lower strain amplitude ($\varepsilon_a < 1\%$), their lifetime is severely limited at a higher strain amplitude ($\varepsilon_a > 2\%$). Since the application of flexible devices usually induces more than 2% strain amplitude, evaporated metallic thin-films will not sustain higher fatigue cycles. As previously discussed, the stress amplitude in the metallic thin-films can be very high at a higher strain amplitude, and the high stress amplitude leads to the limited fatigue lifetime. Thus, for ensuring an improved fatigue lifetime of metallic thin-films, the high stress amplitude in the thin-films must be lowered. This insight has motivated the replacement of evaporated metallic thin-films by alternative materials, which can be achieved by several approaches, as reported in the literature [29, 30, 32, 114–118]. Evaporated metallic thin-films can be replaced by nanoporous particles-based thin-films, e.g., AgNPs thin-films [116]. Alternatively, they can be replaced by thin-films based on a network of conductive nanomaterials, e.g., AgNWs and CNTs [32,117,119]. B.-J. Kim *et al.* has reported that inkjet-printed AgNPs thin-films on PI substrates can maintain its resistivity for 5×10^5 cycles [116] at a strain amplitude of 1.1%. In the doctoral study of T. Haas [30], the inkjet-printed AgNPs thin-films on PET substrates have exhibited a lifetime up to 1×10^5 cycles at a strain amplitude of 1.7%. The highly improved fatigue lifetime of AgNPs thin-films is ascribed to the optimized nanoporous microstructure by proper sintering temperature and time. The optimized nanoporous

microstructure ensures the connectivity between the metallic particles and meanwhile delocalizes strain by the nanopores. This leads to a delay in plastic deformation and subsequent fatigue damage [116]. In addition, AgNWs thin-films exhibited a further improved lifetime than that of AgNPs thin-films. It has been reported that AgNWs thin-films on PI substrates showed a fatigue lifetime up to 5×10^5 cycles at a strain amplitude of 4%, which is much higher than the strain amplitude for evaporated metallic thin-films and inkjet-printed AgNPs thin-films [117]. This improvement in strain amplitude and fatigue lifetime is benefited from the nanoporosity and the microstructure of the AgNWs network. Similar to the AgNPs thin-films, AgNWs thin-films are also nanoporous. However, the network of AgNWs is mainly connected via mechanical junctions between individual NWs instead of the sintering necks between neighbouring particles in AgNPs thin-films, and local strains can be easily accommodated without plastic deformation. The AgNWs network only fails locally at the junctions that are randomly distributed, as compared to fatigue-induced crack formations in evaporated metallic thin-films and metallic NPs thin-films [118]. These mechanisms of AgNWs thin-films lead to a significantly improved lifetime at a strain amplitude as high as 4%.

However, the real trick of taking advantage of nanoporous or nanomaterial-based thin-films, such as AgNPs and AgNWs thin-films, is to make the strain amplitudes in the building blocks of the thin-films lower than that in the thin-film and the substrate. These building blocks of the thin-films include nanoparticles (NPs), nanowires (NWs), and nanotubes (NTs). The AgNPs thin-films exhibited a higher lifetime because the local strain in the nanoporous microstructure of AgNPs is not very high. Unfortunately, this aspect was not fully understood and discussed in the literature. In evaporated metallic thin-films, the applied strain on the polymer substrate is completely transferred into the thin-films, which means the strain amplitude in the film and the substrate is the same: $\varepsilon_{film} = \varepsilon_{substrate}$. Whereas in the nanoporous and nanomaterial-based thin-films, the applied strain in

the polymer substrate is transferred into the thin-films but not entirely into their building blocks. Because of the nanoporous structures and the degree of freedom to accommodate strain locally, the strain amplitude in the building blocks can be much smaller than that in the film and the substrate: $\varepsilon_{NPs/NWs/NTs} << \varepsilon_{film} = \varepsilon_{substrate}$. In other words, even at a higher strain amplitude applied in the film/substrate whole system, the realistic strain in the nanoparticles, nanowires or nanotubes is reduced than that in the film and the substrate. Therefore, for the same strain amplitude, the lifetime of nanoporous and nanowires/nanotubes-based thin-films can be highly improved compared to the evaporated metallic thin-films.

In order to significantly improve the fatigue failure strain, thin-films based on CNTs may be even more promising than AgNPs and AgNWs thin-films. It has been reported that CNTs were added into AgNPs and AgNWs as reinforcement to improve the reliability of metallic thin-films further while ensuring the conductivity at the same time, because the addition of CNTs can suppress crack formation in AgNPs/CNTs composite films and junction failures in AgNWs/CNTs composite films, respectively [29, 32]. Inspired by the literature, it is questioned that since CNTs can be used as reinforcement to improve the reliability of metallic thin-films, how long would be the lifetime of thin-films consisting of a network of purely CNTs on polymeric substrates. Moreover, no systematic studies have been done on investigating the electro-mechanical reliability of CNT-based conductive thin-films under bending fatigue conditions. How would the resistance of CNT-based conductive thin-films develop during cyclic bending? Which strain amplitude could the CNT-based conductive thin-films sustain? How many bending fatigue cycles could they sustain? If they fail, what are the fatigue failure mechanisms for CNT-based conductive thin-films? In addition to the strainability of CNT-based conductive traces and films, these open questions have motivated this doctoral study.

3 Methodology

This chapter describes the formulation route of CNT dispersions and inks, and how they are further fabricated to conductive traces and thin-films on polymeric substrates. Micro-tensile tests have been conducted to characterize their electromechanical behavior upon large tensile loading, and bending fatigue tests have been carried out to test their mechanical reliability under cyclic tensile loading. Microstructural characterizations using scanning electron microscopy, focused-ion beam microscopy, and helium-ion microscopy have been performed, in order to reveal the mechanism of how the network of carbon nanotubes responds to the applied strain.

3.1 Sample fabrication

3.1.1 Formulation of CNT dispersions

The as-received CNTs consist of strongly-entangled agglomerates, which result from the very large aspect ratio of the CNTs and the strong van der Waals forces among them. The CNTs used in this study are commercially available multi-walled carbon nanotubes (NC7000™, Nanocyl S.A., Belgium). They have an average of 9.5 nm in diameter and are 1.5 μm long, giving an aspect ratio of about 150. The morphology of the as-received MWCNTs is shown in Figure 3.1.

The fabrication routes in this work are all based on solution processing. The typical starting point is the formulation of dispersions or inks, which contain the functional conductive materials, here the CNTs. A usual and effective practice is mixing CNTs in a solution with additives, and disperse the tubes

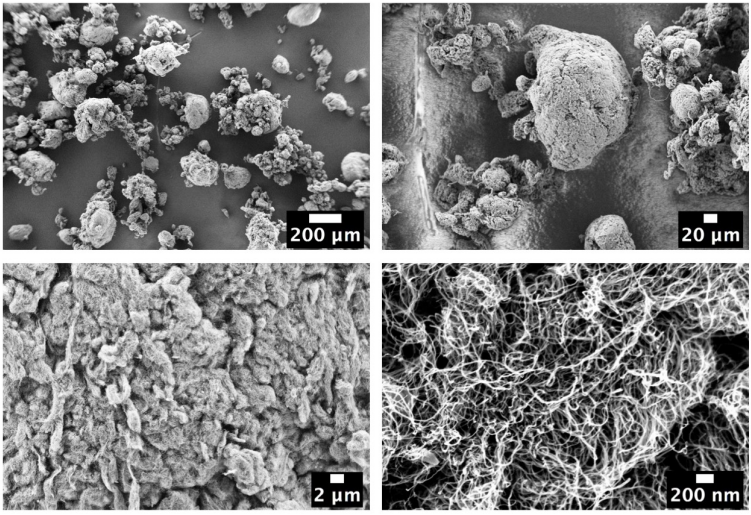

Figure 3.1: Microscopic morphology of as-received Nanocyl® NC7000™ MWCNTs in the form of strongly-entangled agglomerates.

by a high amount of mechanical energy within the liquid mixture. The additives can include dispersing agents, like surfactants such as Triton-X100, SDS, and SDBS or wetting agents and even rheology modifiers, which can increase the viscosity of the dispersion. In this work, the CNT-ink for the inkjet-printing process is water-based, and its formulation route is schematically illustrated in Figure 3.2. The formulation usually starts with mixing the raw CNTs with dispersing agents in de-ionized (DI) water. Afterwards, the mixture is dispersed by a sonication horn, thereby larger agglomerates of CNTs should be reduced to a lower level. When needed, a centrifuge step is added, in order to remove the agglomerates further. The dispersion is then filtered to ensure that the final particle size meets the requirement of the coating or the printing process. Finally, the supernate from the centrifuged or filtered dispersion is collected into a vial, which is sealed for storage.

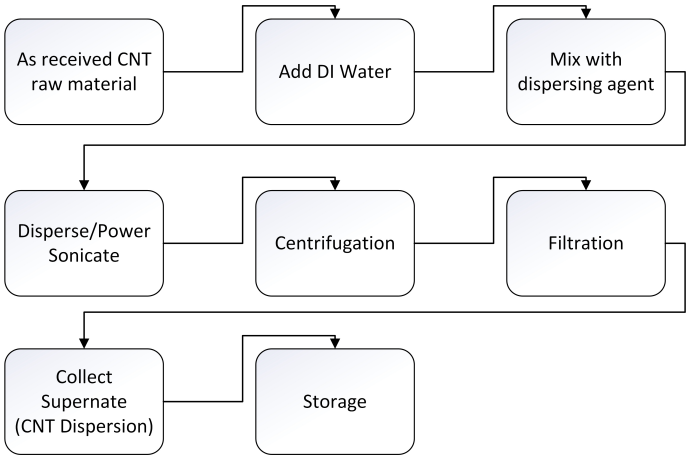

Figure 3.2: Flow chart of preparation steps in dispersing carbon nanotubes.

Many established methods to fabricate conductive traces from CNT dispersions are well-reviewed in [58,120,121]. In this work, two kinds of methods were mainly used. Inkjet-printing was used to fabricate conductive traces as very narrow lines on PET substrates, and spin-coating was used to deposit conductive films on PET substrates.

3.1.2 Inkjet-printing of CNT conductive traces

A commercial drop-on-demand (DOD) inkjet printing system (AD-P-8000, Microdrop GmbH, Germany) was used to fabricate CNT conductive traces. The inkjet printer features a rack for multiple printheads. The printhead is piezo-actuation driven and is usually built with only one nozzle. The diameter of the nozzle is available in 30 µm, 50 µm, 70 µm, and 100 µm. In this work, a printhead with 70 µm nozzle diameter (MD-K-140, Microdrop GmbH, Germany) was used.

Before inkjet-printing, the CNT-ink was formulated as follows. 1.5 gram of SDS (3 wt%) was added into 50 ml DI-water, and the mixture is stirred

until SDS has completely dissolved in water. Then, around 0.05 gram of as-received MWCNTs (0.1 wt%) was added in the mixture and further stirred for 10 minutes. Afterwards, the mixture was dispersed by a horn-sonicator (Bandelin Sonopuls HD2200) for 30 minutes with a duty cycle of 50 % using a power of 220 Watt. The ultra-sonication was done stepwise at room temperature, each step for 5 minutes with enough cooling time before starting the next step. The dispersion was further centrifuged at 6000 rpm for 40 minutes in order to separate the dispersed particles and the agglomerates. In the end, the supernate from the centrifuged dispersion was collected into a vial, which is sealed for storage. The as-prepared CNT-ink is stable for 48 hours. After 48 hours, a new CNT-ink has to be prepared. Before inkjet-printing was carried out, the viscosity of the self-made CNT ink was characterized by a rheometer (Physica MCR300, Anton Paar GmbH, Austria), and its surface tension was measured by a surface tension meter (K100, KRUESS GmbH, Germany).

The fabrication route of inkjet-printing CNT conductive traces on the PET substrate is illustrated in Figure 3.3. The CNT ink droplets are jetted on the PET substrates with specific spacing. When the spacing between the droplets is appropriate, the liquid edges of adjacent droplets can spread into each other. As a result, adjacent droplets can coalesce, thus forming a stable liquid line (or so-called "bead") [122]. After drying and annealing, the organic residuals are evaporated, and solid contents (here CNTs) remained, thus forming a solidified trace. The CNT conductive traces were printed with different droplet spacing (from 55 µm to 90 µm) and drying temperatures (from room temperature to 80 °C). Afterward, the printed conductive traces were further annealed in the oven at elevated temperature (usually above 90 °C). In the end, the printed traces were cut by a precision cutter for further investigation.

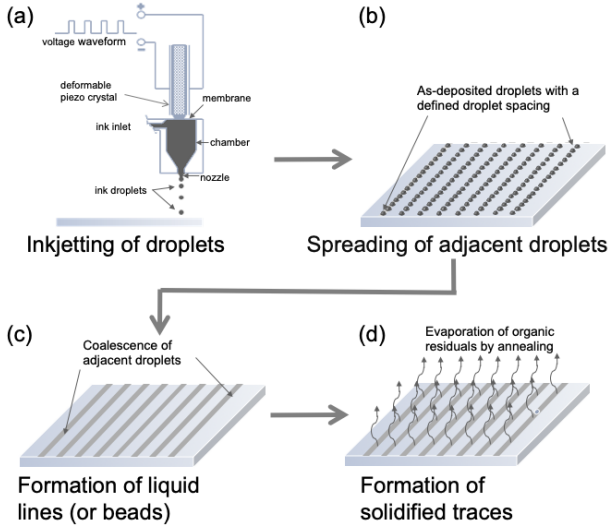

Figure 3.3: Schematic showing the fabrication route of CNT conductive traces via inkjet-printing: (a) droplets are formed and jetted onto the PET substrate; (b) droplets are deposited with a defined droplet spacing, adjacent droplets spread further towards each other; (c) adjacent droplets coalesce into a liquid line (or bead); (d) organic residuals are evaporated by annealing, and solid traces are formed.

3.1.3 Spin-coating of CNT conductive films

Spin-coating is a standard method widely used in the semiconductor industry. It is a very low cost, easy-to-setup, and fast method to achieve homogeneous films on various substrates. Also, it is adopted for overcoming the challenge of coating larger areas. Since the sample size required for the mechanical tests is large, it has been decided to prepare the polymer substrates into the shape of a 7cm×7cm square. In order to fix such a large and flexible substrate onto the spin coater, a larger chuck was designed. It consists of a base made out of polytetrafluoroethylene (PTFE) and a 2 inches silicon wafer, which is glued on top of the PTFE base. The PET substrates were then placed on top of the silicon wafer, and the four edges were fixed with sticky tape.

The viscosity and the concentration of CNTs of the self-made dispersion are roughly 1 mPa·s and 1 mg/ml, respectively. However, both viscosity and concentration are unsuitable for deposing a large area. Thus, it has been decided to use a commercial CNT dispersion (Aquacyl™ AQ0101, Nanocyl S.A., Belgium) for spin-coating, since it is an aqueous dispersion of ionic surfactants and high purity MWCNTs with a high loading of 1wt% (equivalent to 10 mg/ml). The MWCNTs dispersed inside the dispersion are Nanocyl® NC7000™, the same as the ones used previously for formulating CNT inks for printing.

PET substrates (Melinex® ST504, thickness of 125 µm) were first cut into 70mm×70 mm-sized square plates with a precision cutter. Afterwards, to remove dust particles and pollution, both sides of the PET substrates were cleaned in DI-water, isopropanol, and acetone, each for 15 minutes within a bath sonicator. Finally, the cleaned PET square plates were fixed by sticking tapes onto the customized chuck of the spin coater (CPS10, Semitec, Germany).

There are usually four stages during the spin-coating process, as shown in Figure 3.4. In the initial stage, the coating solution is cast onto the middle of the substrate, and then the chuck starts to spin up at a slower speed so that the liquid can be spread to the edges of the substrate and cover the whole surface of the substrate. Afterwards, the chuck continues spinning, but at a much higher speed. During this stage, the excess liquid is spun off, and the thickness of the liquid layer is thinned homogeneously until the spinning is stopped. Finally, the liquid layer is dried in the ambient environment, and a final film with a certain thickness is formed.

Two different batches of MWCNT/PET samples were prepared, which involved two different pretreatment steps and subsequent spin-coating. The first batch of samples (B1) was prepared with direct spin-coating after the sonication. The second batch of samples (B2) was prepared with an additional pretreatment of the coating mixture. The pretreatment included a centrifugation step and a transfer step. The parameters for the centrifugation

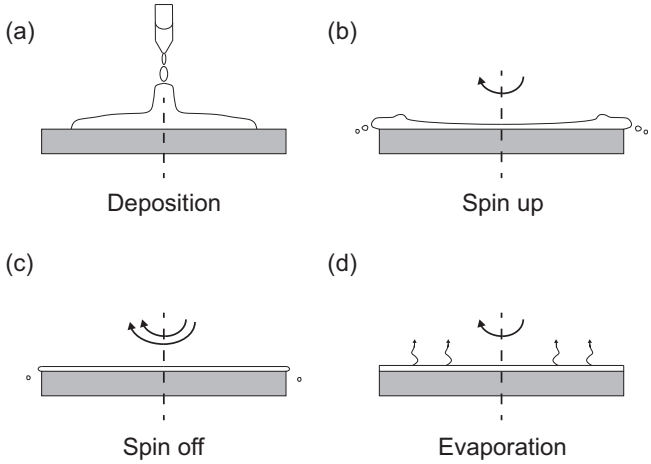

Figure 3.4: Four stages of the spin-coating process.

and filtration were the same as the ones for inkjet printing. The spin-coating procedure is the same for batch B1 and batch B2. The CNT dispersion (about 4 ml) was transferred by a pipette onto the substrate before starting the spin-coating as follows: the first droplet was placed precisely in the center of the substrate, and as the droplet wet the substrate and spread further, more droplets were placed continuously until the CNT dispersion covers the whole surface of the PET substrate. The substrate was then spun with a 2-stage spinning: in the first stage at 600 rpm for 5 seconds and in the second stage at 1200 rpm for 60 seconds. Following the spin cycles, the films were dried in air for 10 minutes. For films with more than 1 layer, each additional layer was deposited, and spun-off after the previous layer was dried for 10 minutes. Films with 1 layer (1L), 2 layers (2L), and 3 layers (3L) of MWCNTs were fabricated for each batch. The coated CNT films were annealed immediately in a vacuum oven after the spin-coating. However, the annealing temperature was different for batch B1 and batch B2. For batch B1, the samples were annealed at 130 °C for 2 hours. For batch B2, the samples

were annealed at 90 °C for 12 hours. The fabricated samples were named according to Table 3.1.

Table 3.1: Sample denotation for the two batches of spin-coated CNT films.

Batch	Number of layers	Sample name
B1	1L (1 layer)	B1_1L
	2L (2 layers)	B1_2L
	3L (3 layers)	B1_3L
B2	1L (1 layer)	B2_1L
	2L (2 layers)	B2_2L
	3L (3 layers)	B3_3L

3.1.4 Characterization techniques

In order to control the quality of the deposited traces and films via inkjet-printing and spin-coating, a series of specific characterization techniques are applied. Firstly, Raman spectroscopy is used to control the quality of the as-received CNTs (reflected by purity) before formulating CNT dispersions. Secondly, laser diffraction spectroscopy is used to measure the agglomerate size in the CNT dispersions, so that the average size of CNT agglomerates can be controlled during the formulation and dispersing process. Moreover, after formulation, the rheological property of CNT dispersion is vital to the printing and coating process. Two critical parameters for evaluating the printability of CNT dispersions are the viscosity and the surface tension. For tailoring the viscosity of the CNT dispersion, the viscosity of the CNT dispersions is characterized by a rheometer. The surface tension of the CNT dispersions is determined by a tensiometer. After depositing, the CNT film quality, such as morphology and homogeneity, shall be examined, which is conducted through characterizing the surface topography of the CNT films.

Finally, the sheet resistance of the CNT films is measured for evaluating their electrical performance.

Raman spectroscopy

Raman spectroscopy, also known as Resonance Raman spectroscopy or Raman scattering spectroscopy, is a fast, selective, and effective method for the identification and characterization of materials. Raman scattering is sensitive to the interatomic distance, and the Raman band frequency shifts indicate the strain that is applied to Raman-active materials. In the case of CNTs, the strain exerted on nanotubes extends or shortens the C-C bond, causing a Raman shift in the spectrum. The Raman spectroscopy of the as-received CNTs (Nanocyl® NC7000™) was carried out on a commercial Raman spectrometer (LabRAM HR Evolution, Horiba, Japan). Major identifiable Raman absorption signatures of CNTs include the radial breathing mode (RBM), the disorder-induced band (D-band), the tangential mode (G-band), and its overtone or D-band's second-order related harmonic (G'-band) [123]. The D and G bands are located at about 1350 and 1580 cm^{-1}, respectively. It should be noted that the G'-band is especially interesting due to its sensitivity to stress and polarization [123]. The ratio of the D to the G band intensities I_D/I_G from the Raman spectra gives a direct measure of the quality of the CNT sample [123, 124].

Laser diffraction spectroscopy

The average size of particles in a dispersion can be measured by laser diffraction spectroscopy, also known as laser diffraction analysis. For measuring the average size of CNT agglomerates, a commercial laser diffraction particle size distribution analyzer (Partica LA-950, Horiba, Japan) is used. The spectrometer is equipped with two light sources, a red laser with a wavelength of 650 nm, and a blue LED light with a wavelength of 405 nm. Laser diffraction spectrometer measures particle size distributions by mea-

suring the angular variation in the intensity of light scattered as a laser beam passes through a dispersed particulate sample. According to the Fraunhofer diffraction theory [125], the intensity of light scattered by a particle is directly proportional to the particle size. Large particles scatter light at small angles relative to the laser beam, and small particles scatter light at large angles. By assuming a volume equivalent sphere model, the particle size distribution can be calculated using the Mie theory of light scattering [126]. The LA-950 is capable of measuring particle sizes in the range of 30 nm to 3 mm. As a rule of thumb, for a printable CNT-ink, the average size of particles should be smaller than a hundredth of the nozzle diameter. The average size of CNT agglomerates in different solutions such as in DI-water, isopropanol, and acetone was characterized at room temperature.

Rheological properties

The rheological properties of CNT dispersions and inks, including dynamic and kinematic viscosity, can be characterized by a rotational rheometer (Physica MCR300, Anton Paar GmbH, Austria). Dynamic viscosity η, also called absolute viscosity, is usually measured. Kinematic viscosity ν is defined as the ratio of the dynamic viscosity η to the density of the fluid ρ:

$$\nu = \frac{\eta}{\rho}. \tag{3.1}$$

CNT dispersions and inks are non-newtonian fluids, in which the viscosity can decrease with increasing shear rates. The cone-plate method is typically applied for measuring the viscosity of non-newtonian fluids. A cone dipped into a fluid that is held on a plate and rotated under different angular velocities. By measuring the torque and the rotational speed, and knowing the cone angle and the radius of the cone, the dynamic viscosity η can be calculated [127]:

$$\eta = \frac{F}{\gamma} = \frac{\frac{3G}{2\pi R^3}}{\frac{\Omega}{\psi}} = \frac{3G\psi cos(\psi)^2(1-\frac{\psi^2}{2})}{2\pi\Omega R^3} = \frac{kG}{\Omega}, \tag{3.2}$$

where F is the shear stress, γ is the shear rate, G is the torque, R is the radius of the cone, Ω is the angular velocity, ψ is the cone angle, and k is the viscometer constant, which is usually supplied by the manufacturer. With the cone-plate method, the viscosity can be measured in a wide range from 0.1 mPa·s up to 1000 mPa·s. During the measurement, the shear rate is increased continuously from 0 to 10000 s^{-1}. Commonly, the dynamic viscosity at the shear rate of 1000 s^{-1} is chosen for evaluation. All measurements of dynamic viscosity were carried out at room temperature.

Surface tension

The surface tension of CNT dispersions and inks is determined with a commercial force-sensitive tensiometer (K100, KRUESS GmbH, Germany). The tensiometer measures the surface tension based on the Wihlemy plate or the ring method [128]. In this method, a thin plate or a ring with a defined contour, usually made of platinum, is used to measure equilibrium surface or interfacial tension at air-liquid or liquid-liquid interfaces. The plate is oriented perpendicularly to the interface, and the force exerted on it is measured. The plate or ring is moved towards the liquid surface until the meniscus connects with it. A precise force sensor or microbalance measure the force acting on the plate due to the wetting of liquid. The surface tension γ is determined by the Wilhelmy equation [128] as follows:

$$\gamma = \frac{F}{(2w+2d)cos(\theta)} = \frac{F}{lcos(\theta)}, \tag{3.3}$$

where F is the force measured by the force sensor, w is the plate width, d is the plate thickness, l is the wetted perimeter $(2w+2d)$, and θ is the contact angle between the liquid phase and the plate. In practice, the contact angle is rarely measured. Instead, either a literature value is used, or complete wet-

ting ($\theta = 0$) is assumed. All measurements of surface tension were carried out at room temperature.

Surface topography

The surface topography of inkjet-printed or spin-coated CNT film can be characterized by confocal microscopy. A commercial 3D laser scanning confocal microscope (VK-9710K, Keyence, Japan) is employed in this study. The VK-9710K is equipped with two light sources: a violet laser (wavelength: 408 nm) light source and a white light source. Firstly, the short waveform laser beams can detect reflecting light intensity and height. The VK-9710K scans the field of the microscope using a laser beam and an optical system. The light-receiving element detects reflecting light from each pixel in the field of view. Driving the objective lens in the Z-axis and scanning repeatedly obtains reflecting light intensity based on the Z position. Height information is obtained and reflecting light intensity detected while focusing on the peak position. Secondly, the CCD camera in VK-9710K can obtain color information. Reflecting light from the white light source is detected with a color CCD camera. The CCD camera obtains color information at the peak (focus point) detected with the laser light source on a pixel basis. Consequently, the VK-9710K obtains not only data for omnifocal light intensity ultra-depth images and high-low images, but also real color images of the examined sample. Thus, it can perform surface topography analysis such as non-contact profile, roughness, and high definition ultra-depth measurement and 3D measurement with a spatial resolution down to 0.001 μm. Nine different locations across the spin-coated CNT films were analyzed.

Sheet resistance

The conductivity of thin-films is most commonly characterized by sheet resistance. The sheet resistance (in Ohms/sq.) can be measured by the Kelvin-

probe-method, or known as the four-point probe method. The working principle of a four-point probe is illustrated in Figure 3.5. Four equally spaced electrodes with the shape of a sharp tip (tip radius: 40 µm) are in contact with the sample surface. A small quantity of current (I) is generated between the outer two tips by a source meter. A precision voltmeter measures the corresponding potential difference (ΔV) between the inner two tips. Thereby the sheet resistance R_{sq} can be calculated:

$$R_{sq} = \frac{\pi}{ln(2)} \frac{\Delta V}{I} = 4.53236 \frac{\Delta V}{I}. \tag{3.4}$$

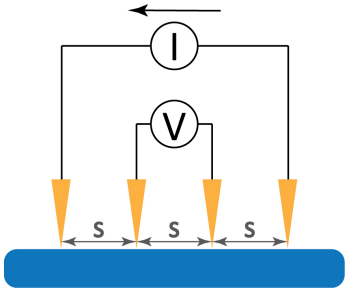

Figure 3.5: Schematic illustrating the working principle of a four-point probe.

The sheet resistance of as-prepared samples is measured by a four-point probe (JANDEL Four-Point Probe, Bridge Technology, USA) connected with a nanovoltmeter (2182A, Keithley Instruments, USA) and a precision current source (6220, Keithley Instruments, USA). The spacing between the tips is 1 mm, and the four tips can cover a measuring field of about 3.68 mm^2. The sheet resistance for the CNT conductive trace or thin-film was measured at nine different locations across the sample.

3.2 Electro-mechanical testing

3.2.1 Micro-tensile tests

Micro-tensile tests were combined with an *in-situ* four-point measurement in order to characterize the evolution of the electrical resistance of the CNT films and traces during straining. A micro-tensile tester (Zug-/Druckmodul 10 kN MZ.Mb, Kammrath&Weiss GmbH, Germany) was used. Four electrodes were connected to a source-meter unit (2614B, Keithley Instruments, USA) for realizing electrical resistance measurement based on the four-point method. The program for the data acquisition was self-written in the TestScriptBuilder (Keithley Instruments, USA) software environment. The whole experimental setup for micro-tensile testing with *in-situ* resistance measurement is shown in Figure 3.6.

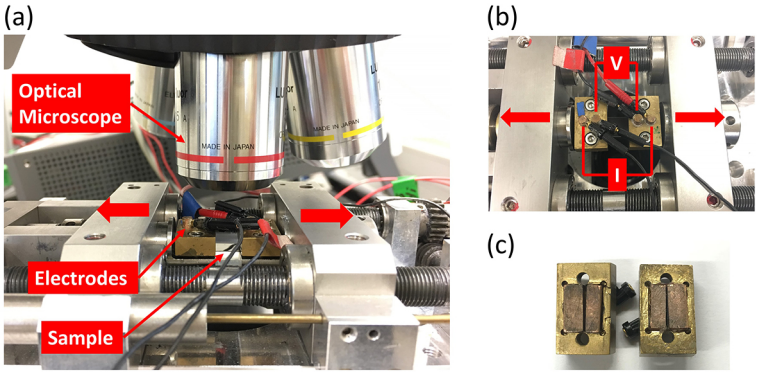

Figure 3.6: Photographs showing the experimental setup for the micro-tensile tests: (a) Positions of the mounted sample and the optical microscope; (b) electrical wiring for the current (I) and voltage (V) connection; (c) the four copper electrodes that are in contact with the sample under test.

The sample under test is prepared into a lateral dimension of 25 mm×8 mm and then mounted underneath the two pairs of copper electrodes. The gauge length L_0 is 8 mm. For a stable electrical contact, four screws on the copper electrodes were carefully tightened. The fabricated 1-, 2-, and 3-

layered CNT thin-films from each batch were stretched continuously from 0% to 50% strain. At the same time, the electrical resistance of the sample is recorded *in-situ* by the source-meter unit. The stretching velocity can be adjusted between 5 µm/s, 10 µm/s, and 20 µm/s. During testing, the moderate stretching velocity: 10 µm/s was chosen. For a cyclic tensile test, the CNT thin-films were firstly loaded from 0% to a specific strain with a stretching velocity of 10 µm/s and then unloaded from the stretched state to a force of around 0 N.

3.2.2 Bending fatigue tests

Bending fatigue tests were conducted, in order to simulate cyclic bending deformation, and to investigate the reliability of CNT-based conductive traces. A commercial instrument (Endurance flexure tester: CK-770FET, CK Tradings Co., South Korea) was deployed [109, 116]. The testing method of this tester is based on the IPC-TM-650 standard, which is described in detail in Appendix 8.4.

The sample size for bending fatigue tests is defined as 4 mm×62 mm. The samples are mounted between two parallel plates; each end of the sample is clamped with a pair of copper contacts to enable electrical contact. During testing, the bottom plate moves horizontally by 10 mm at a frequency of 5 Hz, while the top plate is fixed (Fig. 3.7(a)+(b)). The tester can run up to 1×10^6 bending cycles, and the change in the electrical resistance was measured using a digital multimeter (34410A, Agilent Technologies, USA), a dual-channel digital switcher (7007, Keithley Instruments, USA), and a self-written LabVIEW-based data acquisition program.

The type of strain on the sample can be chosen either as compressive or tensile, if the film side is facing inwards or outwards, respectively. The strain amplitude ε_a can be calculated by (refer to equation 2.5 in Chapter 2.3):

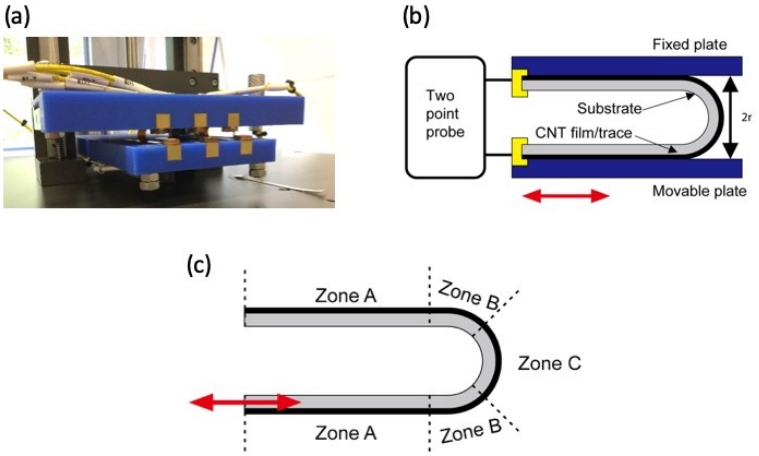

Figure 3.7: (a) Photograph of the bending fatigue tester, (b) Schematic illustrating the sample and electrical connection, and (c) Three different deformation zones forming during bending fatigue testing. Three samples can be tested at the same time, and the applied strain amplitude is imposed by adjusting the gap distance between the fixed plate and movable plate.

$$\varepsilon_a = \frac{d_s + t}{2r}, \tag{3.5}$$

where d_s, t, and r are substrate thickness, film thickness, and the bending radius, respectively. The gap between the two plates corresponds to $2r$ and can be adjusted. A look-up table for the relationship between the imposed strain amplitude and the gap distance is provided in Appendix 8.5. The linear motion of the bottom plate induces three different deformation zones in the sample (Fig. 3.7(c)) [109, 116]. Two undeformed Zones-A are located close to the copper contact, where no deformation occurs. The fatigue damage Zones-B are under cyclic strains during the bending cycles and hence are expected to exhibit fatigue damage. The center part Zone-C remains under a constant bending strain and hence does not show any fatigue damage [109, 116].

3.3 Microstructural characterization

3.3.1 Electron and ion beam microscopy

Due to the complexity of the CNT network, the dimension of carbon nanotubes, and the insulating nature of polymeric substrates, a variety of electron-based and ion-based microscopy techniques were used in this work. These microscopy techniques include scanning electron microscopy (SEM), focused-ion-beam (FIB), and helium-ion-microscopy (HIM). A dual-beam microscope (Nova Nanolab 200, FEI, USA) equipped with SEM and FIB was deployed to conduct *in-situ* straining tests and cross-sectional cutting, respectively. The HIM (Orion NanoFab, Zeiss AG, Germany) was used for high-resolution analysis and to realize direct surface morphology characterization of polymeric substrates without the need for sputtering thin metallic layers.

The surface property of PET substrates plays a vital role in the surface quality of CNT conductive traces and films. Recently, it has been reported in Reference [129] that the surface quality of commercial polyester films has a considerable influence on the film quality; therefore, the surface condition of the as-received PET substrates are required to be characterized.

A variety of methods for characterizing the surface morphology of polymers using electron microscopy have been well summarized in [130]. Since PET is an insulating polymer, a unique SEM microscopy technique (or mode) called "Low-voltage Scanning Electron Microscopy" (LV-SEM) is applied, in order to resolve the surface morphology of the PET with surface charging as less as possible. Many commercial SEMs can realize this imaging technique for polymers. In this work, LV-SEM was performed with different combinations of voltage and current settings on the SEM (Nova Nanolab 200, FEI). It has been suggested that a very low acceleration voltage (< 2.0 kV) and a small current (< 1.0 nA) will cause less charging on the sample surface, resulting in images with fewer artifacts and better contrast [131].

Besides, keeping the distance between the sample surface and the electron gun small enough and activating the TLD (through-the-lens-detector) mode (also known as immersion mode) could help to obtain better images as well. In this work, the as-received PET substrates have been tested in micro-tensile tests and with different strain amplitudes in cyclic bending fatigue tests. Afterwards, the surface morphology of the tested PET substrate has been characterized using the LV-SEM technique, in order to investigate whether any microstructural change occurred in PET by stretching or cyclic deformation.

For characterizing the CNT thin-films tested by micro-tensile tests and bending fatigue tests, SEM and FIB were both involved. SEM is mainly used for observing the top view and tilted view (in 52°) of the surface morphology of CNT films before and after testing. Usually, the SE (Secondary Electron) mode is applied, and a low acceleration voltage (3.0 kV to 5.0 kV) and a small current (< 0.5 nA) are appropriate for resolving micrographs of the CNT film with excellent resolution and contrast. For observing more details of the CNT network at a higher magnification, the TLD (Through the lens Detector) (or In-Lens) mode on the SEM can be activated. In the TLD mode, the working distance between the specimen and the electron gun should be no smaller than 5 mm, and the specimen can only be observed from the top view. FIB was only used for cutting cross-sections in the CNT thin-films. After the deposition of a protection Pt layer in the desired area, the FIB cross-section cut was usually done with two steps. The first step is the rough cutting, in which a high ions acceleration voltage of 30.0 kV and a current of 30-100 pA is usually applied. The second step is the fine cutting with a smaller ions acceleration voltage and a smaller current. After the FIB cutting, the cross-sectional view of the CNT film is imaged by SEM. Sometimes, due to poor contrast between the CNT layer and the PET substrate in the cross-sectional area, the CNT films were not cut by the standard FIB cutting technique. Instead, it was found that the cross-sections cut by a direct FIB milling without the Pt layer can better reveal the interface between the

CNT layer and the substrate. However, this customized technique should be carefully applied. If the voltage or current is large, the surface would be so strongly bombarded that no detailed microstructures can be revealed. Also, if the voltage or current is too small, the CNT film may not be cut through. HIM offers many advantages over traditional SEM (details in [132–134]), such as higher resolution and higher contrast. HIM is typically equipped with a flat gun that can neutralize the electron charging and thus is especially suitable for insulating samples and samples of light elements. Therefore, HIM was used for imaging the CNT samples after fatigue testing, cross-sections of CNT films, and also the surface of bending fatigue tested PET substrates.

No matter by SEM or HIM, the sample morphology was mainly investigated before and after the test for comparison. However, to investigate the sample morphology in the strained state, the tested sample had to be re-loaded. The re-loading has been done with a custom-built setup, which involves a self-made manual straining frame inside the SEM (Fig. 3.8).

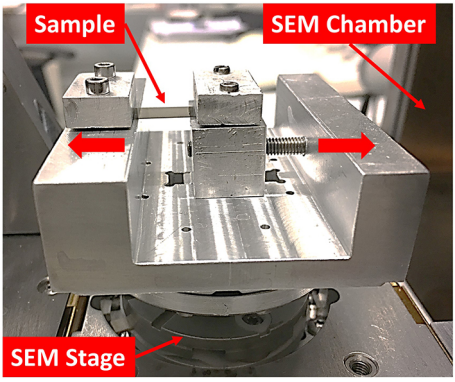

Figure 3.8: Photograph showing the custom-made manual micro-tensile stage used for re-loading the sample in the SEM.

The clamping has been designed the same as the ones on the micro-tensile tester, including the same diamond pads to prevent sample slip. The initial

distance between the stationary and slidable block is kept at 8 mm, which is the same as the gauge length on the micro-tensile tester. In this way, the same sample can be transferred from the micro-tensile tester and mounted on the manual device. The sample can be stretched to a defined strain by a screw mechanism (refer to Appendix 8.6). Finally, the setup with the loaded sample could be mounted inside the SEM.

3.3.2 *In-situ* micro-tensile testing inside the SEM

Though the manual *in-situ* stage is beneficial to reproduce the loading condition, it was impractical for observing continuous microstructural evolution in the film. In order to overcome this limitation, *in-situ* micro-tensile testing inside the SEM has been applied. It allows the observation of the sample during straining and is a very effective method to reveal the microstructural evolution in the sample.

The *in-situ* micro-tensile testing is realized by using a piezo-driven linear nano-translation stage (M-112.1VG, Physical Instruments, Germany) inside the SEM. The whole setup, including the mounted sample before stretching, is shown in Figure 3.9.

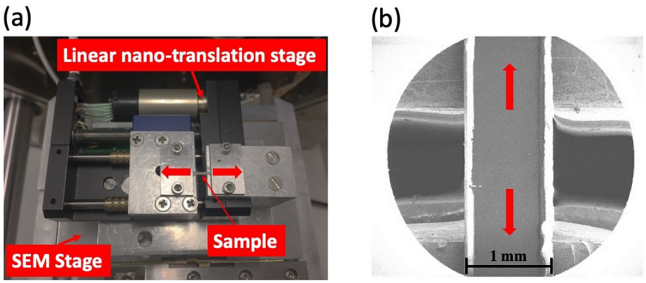

Figure 3.9: (a) Photograph of the micro-translation stage used for the *in-situ* tensile testing inside the SEM; (b) SEM micrograph of a CNT film sample (20mm×1mm) before straining in the tensile direction, which is indicated by the red arrow.

The specimen was precisely cut into a thin stripe of 20 mm$\times$1 mm. The sample is significantly smaller than the ones in the standard micro-tensile tests because the maximum load capacity of the linear motor is only 10 N. The initial gauge length of the specimen is around 4 mm, and it is measured by a caliber every time before testing. The strain was then calculated from the linear movement controlled by software (provided by Physical Instruments, Germany). The sample was strained stepwise to increasing tensile strains of 5%, 10%, 15%, 20%, 30%, 40%, and 50%, and the sample morphology under each strain was investigated by SEM.

4 Fabrication of CNT conductive traces and films

This chapter presents the results of CNT conductive traces fabricated by inkjet-printing and CNT conductive films fabricated by spin-coating. Though there are many advantages of the inkjet printing technique, the printing of CNT-inks is challenging. Different types of CNT-inks, including commercial and self-made CNT-inks, have been tested. The CNT-ink properties, such as weight loading of CNTs, viscosity, and surface tension, have to be optimized in order to meet the printing requirement. For obtaining the best printing result, a variety of printing parameters has to be adjusted. However, inkjet-printing exhibits a few limitations as well. In order to remedy this problem, spin-coating is applied as a scaled-up method for fabricating larger area CNT conductive films. In the discussion, the results from the two methods are summarized and compared in detail.

4.1 Inkjet-printing of CNT conductive traces

4.1.1 Optimization of CNT-ink properties

Before formulating a CNT-ink, the properties of the as-delivered CNTs (Nanocyl® NC7000™ MWCNTs) were investigated. The Raman spectrum of the raw CNTs is shown in Figure 4.1. Typical Raman peaks for MWCNTs can be found: D band at around 1350 cm^{-1}, G Band at around 1600 cm^{-1}, and G' (2D) Band at around 2650 cm^{-1}. The measured positions of Raman peaks for NC7000™ are identical with the reported values in the literature [124]. The surface area of MWCNT was measured by the gas

adsorption method (Gemini VII WIN2390, Micromeritics, USA) based on the Brunauer-Emmett-Teller (BET) theory [135–137]. The measured surface area for NC7000™ is 256 m^2/g, which agrees well with the value in the technical data sheet (DM-TI-02-TDS-NC7000-V08, Nanocyl S.A., Belgium) provided by the manufacturer.

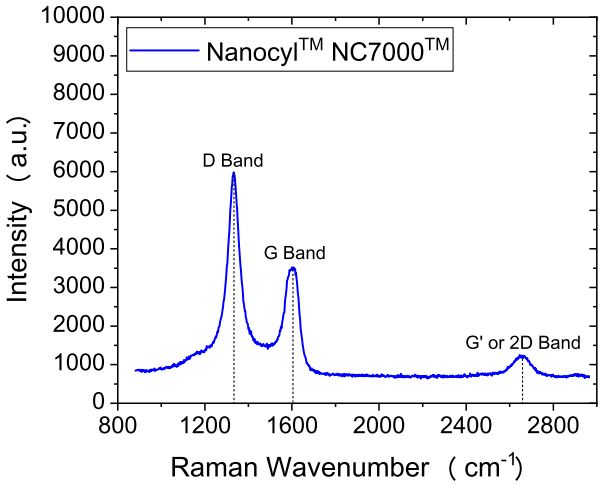

Figure 4.1: Raman spectrum of Nanocyl® NC7000™ MWCNTs.

The CNT-inks were formulated according to the standard route introduced in Figure 3.2. The most crucial step is the ultra-sonication step. The ultra-sonication could lead to foaming when the weight loading of the surfactants is too high. The microscopic foaming of a dried CNT dispersion, as well as CNTs in a well-dispersed state, are shown in Figure 4.2 (a) and (b), respectively. Since the printhead used in this work has a nozzle diameter of 70 µm, the average size of CNT agglomerates should be smaller than 7 µm. Therefore, the effect of sonication power amplitude and sonication time duration on the average size of CNT agglomerates in different solvents has been investigated.

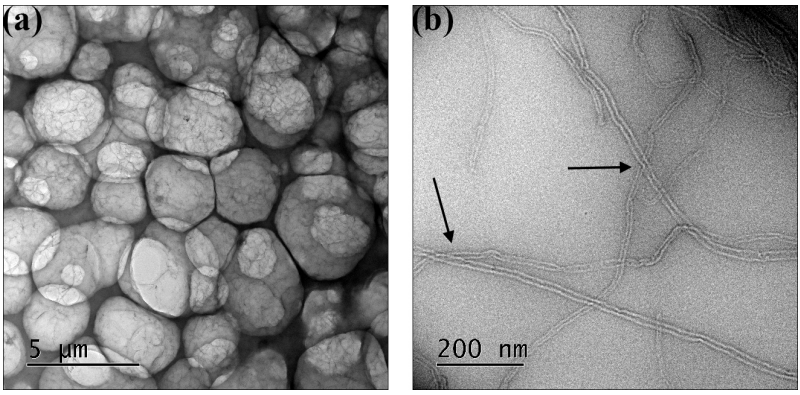

Figure 4.2: TEM micrographs showing (a) microscopic foaming and (b) well-dispersed tubes in the CNT dispersion after ultrasonication.

The particle size distribution of CNTs dispersed in three different solvents is shown in Figure 4.3. It can be seen that increasing sonication power amplitude and sonication time can significantly reduce the average particle size. In a polar organic solvent such as isopropanol, a 30-minutes long sonication with 20% power amplitude can reduce the average particle size down to 10 μm. However, it is harder to disperse CNTs in a non-polar solvent such as cyclohexane. No matter how long and how strong the sonication is, the average size of CNT agglomerates can only be reduced by two orders of magnitude. Though CNTs are non-polar and have strong hydrophobicity, the particle size of CNT agglomerates in deionized water can only be reduced down to 30 μm after ultrasonication.

To stabilize CNTs in aqueous solutions, SDS has been added to disperse CNTs more effectively in deionized water. With the assistance of SDS, the average particle size of CNT agglomerates in deionized water can be further reduced to roughly 2.7 μm (Fig. 4.4(a)). Besides, the addition of SDS can adjust the viscosity of the CNT-ink. A series of CNT-inks with different weight loadings (in wt%) of SDS was prepared to compare the effect of SDS content on the viscosity of the CNT-ink. The loading of MWCNTs is

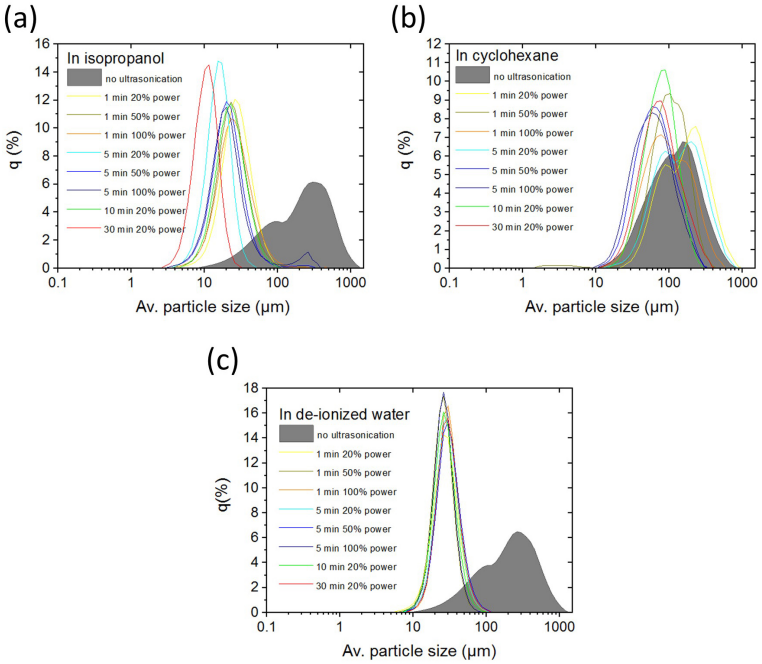

Figure 4.3: Particle size distribution before and after ultrasonication of CNTs dispersed in (a) isopropanol, (b) cyclohexane, and (c) de-ionized water, respectively. The duty cycle for all ultrasonication is kept at 50%. A 100% power is 220 Watt.

kept at 0.1 wt%, while the SDS loading has been increased from 0.1 wt% to 3.0 wt%. By increasing the SDS loading to 3.0 wt% (Fig. 4.4(b)), the viscosity can be increased to 1.95 cP (mPa·s), which approaches the lower limit of the viscosity requirement for inkjet printing (refer to Chapter 2.2). However, a higher loading of SDS than 3.0 wt% will lead to foaming, which is detrimental for inkjet printing.

In addition, different as-prepared CNT-inks have been acquired, including semiconducting SWCNT-ink, metallic SWCNT-ink, and MWCNT-ink (provided by Frank Heinrich, INT, KIT), a commercial CNT-ink (CNTRENE^{TM} 3015 A3R, Brewer Science, Inc.), and two self-made MWCNT-inks. The

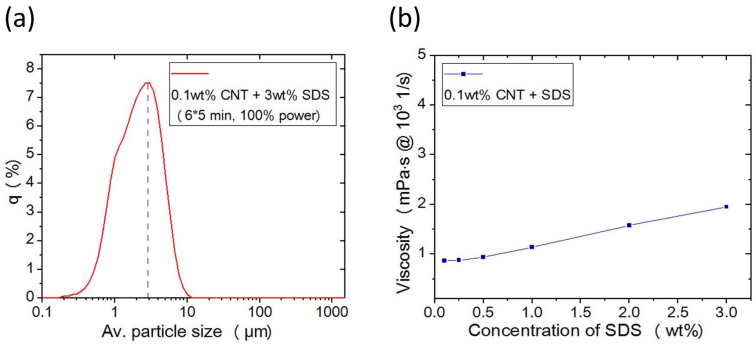

Figure 4.4: (a) Particle size distribution for a self-made MWCNT-ink with 0.1 wt% loading of NC7000™, which is dispersed for 30 mins (6×5*mins*) under 100% power (220 Watt); (b) Effect of the SDS loading (in wt%) on the dynamic viscosity of the self-made MWCNT-ink.

chemical composition of these CNT-inks is listed in Table 4.1. Except for the commercial CNT-ink A3R, which is ethanol-based and has a higher loading of 3 wt% of mixed metallic SWCNTs and MWCNTs, all the other CNT-inks are water-based and possess a weight loading of CNTs only up to 0.3 wt%. For the five non-commercial CNT-inks, the type and manufacturer of the dispersed tubes are completely different. Expensive research-grade tubes (95% carbon purity): HiPco^{TM} SWCNTs and HiPco^{TM} MWCNTs (NanoIntegris, Inc.) are used in the CNT-inks provided by INT, KIT. In comparison, inexpensive industrial-grade tubes (90% carbon purity): NC7000™ MWCNTs (Nanocyl S.A.) are used in the two self-made MWCNT-inks. However, the chemical composition of the five non-commercial CNT-inks is comparable, since the same surfactant-SDS is used to disperse CNTs in deionized water. Due to these commonalities and differences, for verifying the printability of the listed CNT-inks and comparing the performance of the self-made MWCNT-inks with other inks, all six inks have been characterized and systematically tested for inkjet printing.

Table 4.1: Basic information of all tested CNT-inks

Short name	Inks	Source	CNT Type	Weight loadings	Solvent	Dispersing agent
SemiSWInk	Semiconducting SWCNT-ink	Frank Heinrich, INT, KIT	HiPco™ SWCNT	0.1 wt%	deionized water	SDS, wt% n.a.
MetSWInk	Metallic SWCNT-ink	Frank Heinrich, INT, KIT	HiPco™ SWCNT	0.1 wt%	deionized water	SDS, wt% n.a.
MWInk	MWCNT-ink	Frank Heinrich, INT, KIT	HiPco™ MWCNT	0.1 wt%	deionized water	SDS, wt% n.a.
A3R	CNTRENE™ 3015 A3R	Brewer Science	Mixture of metallic SWCNTs and MWCNTs	3.0 wt%	ethanol	Not available (n.a.)
SelfMade01	MWCNT-ink 01	Self-made	Nanocyl® NC7000™	0.1 wt%	deionized water	1.0 wt% SDS
SelfMade02	MWCNT-ink 02	Self-made	Nanocyl® NC7000™	0.1 wt%	deionized water	3.0 wt% SDS

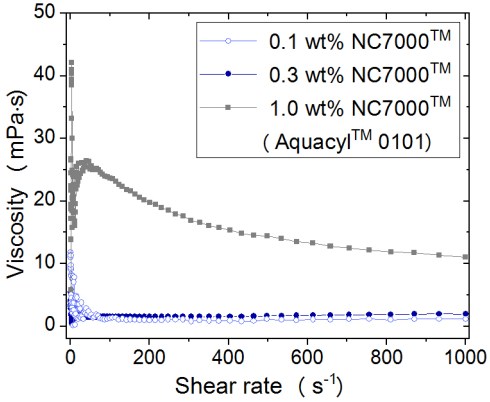

Figure 4.5: Dynamic viscosity as a function of the shear rate measured for inks with different loadings (in wt%) of MWCNTs (NC7000™).

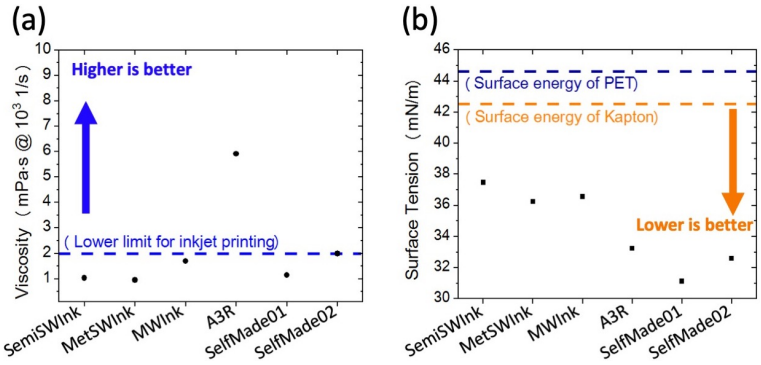

Figure 4.6: (a) Viscosity and (b) surface tension of all tested CNT-inks.

The pre-requisite for successful droplet jetting is that the viscosity should be between 2-15 cP [8, 77, 80]. Except for adjusting the loading of the surfactant, the viscosity of the self-made MWCNT-ink can be increased by increasing the loading of CNTs themselves. As shown in Figure 4.5, the viscosity of the self-made MWCNT-ink can be increased when the loading of CNTs is increased from 0.1 wt% to 0.3 wt%. In the commercial CNT

dispersion (Nanocyl® Aquacyl™ AQ0101), the loading of the same type of CNTs (Nanocyl® NC7000™) is as high as 1.0 wt%, and its corresponding dynamic viscosity (at 1000 s^{-1} shear rate) is roughly 11 cP, which is almost ten times higher than the dynamic viscosity of the self-made MWCNT-ink with 0.1 wt% loading. For better comparison and the prevention of large CNT agglomerates, the loading of CNTs in self-made MWCNT-inks is fixed to 0.1 wt%.

The viscosity and surface tension of all six inks are compared in Figure 4.6. It can be seen that only "A3R" and "SelfMade02" suffice the requirement for viscosity. The viscosity of the commercial CNT-ink "A3R" is in the safe zone, while the viscosity of the self-made MWCNT-ink "SelfMade02" is on the lower limit, which is indicated by the blue dashed line (Fig. 4.6(a)). The surface tension of the ink not only influences the jettability of ink droplets but also determines if the ink droplet will wet the substrate thoroughly. The optimum surface tension for inkjet printing should be in the range of 20-70 mN/m (refer to Chapter 2.2). In addition, an empirical rule for sufficient wetting is that the surface tension of the ink must be lower than the surface energy of the substrate [58]. The lower the surface tension of the ink, the easier it is for the ink to wet the substrate [58]. The orange and blue dashed lines (Fig. 4.6(b)) indicates the surface energy of the Kapton substrate and the PET substrate, respectively. It can be seen that the surface tension of all six inks meet the requirement, which implies they can wet both the Kapton and PET substrate thoroughly.

All six inks were loaded onto the printing system and tested with different printing parameters using a 70 µm printhead (MD-K-130, Microdrop GmbH, Germany). Only "MWInk","SelfMade01", and "SelfMade02" provided stable droplet formation. It must be pointed out that for the commercial ink "A3R", even its viscosity and surface tension perfectly meet the printing requirement, an immediate clogging of the printhead was obtained, possibly due to the very high loading of CNTs. Thus, for fabricating the CNT conductive traces, the self-made MWCNT-inks were adopted. In this

study, the printing tests were firstly performed on Kapton substrates and subsequently transferred on PET substrates.

4.1.2 Post-printing treatment

A stable droplet formation is essential for continuous inkjet printing, whereas post-printing treatments determine the solidification and final structure of printed patterns. The primary influence factors include droplet spacing, coffee-stain effect, and sintering temperature. Since the printing tests were performed on Kapton and PET substrates, the printed patterns on both substrates have been characterized.

The droplet spacing is defined as the distance between the center of two adjacent droplets. Variation of droplet spacing could lead to different morphology of the printed line, such as individual drops, scalloped (or wavy) line, uniform line, bulging line, and stacked coins. All these morphologies have been reported when printing PEDOT: PSS patterns [138]. Different morphologies formed after printing the self-made MWCNT-ink "Self-Made01" are shown in Figure 4.7. It can be seen that individual drops, uniform lines, or bulging lines formed on the PET substrate after printing. When the droplet spacing is larger than the nozzle diameter, it tends to form individual drops. With an appropriate droplet spacing, a line with uniform edges can form. When the droplet spacing is too small, individual droplets tend to overlay each other, the overlapped volume of a droplet tends to wet the substrate further, thus leading to a varying width of the line: bulging line.

The influence of droplet spacing becomes even more critical when parallel lines are printed sequentially at ambient temperature. It can be seen in Figure 4.8 when the droplet spacing was decreased from 75 µm to 55 µm, the corresponding printed films consisted of parallel lines showing different morphologies. With the droplet spacing decreasing from 75 µm to 60 µm, the film morphology can be improved on Kapton substrates. However,

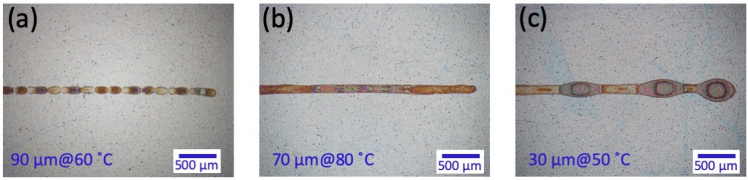

Figure 4.7: Optical images of printed lines from the self-made MWCNT-ink on PET substrate with different morphologies: (a) individual drops, (b) uniform line, and (c) bulging line, printhead nozzle diameter: 70 µm.

with a droplet spacing of 55 µm and a sintering temperature of 30 °C, the appearance of stacked coins again led to an inhomogenous film on Kapton substrates. Thus, it can be concluded that, for a printhead with a nozzle diameter of 70 µm, a droplet spacing around 60 µm is an appropriate value on Kapton substrate. However, due to the slow evaporation rate of water at room temperature and the coffee stain effect, the morphology was still not perfect. The same tests were also performed on PET substrates, and it was found that the appropriate droplet spacing is again around 60 µm.

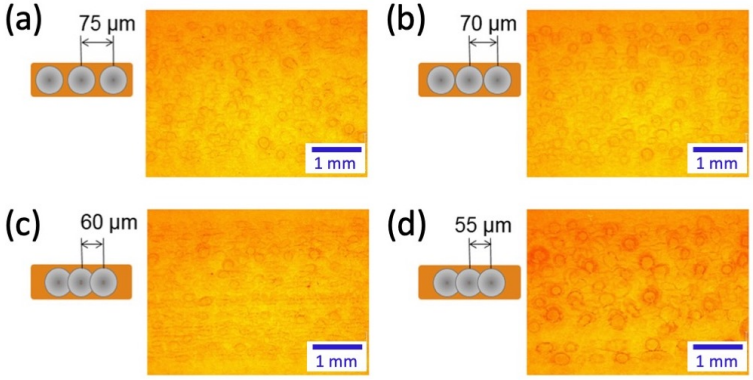

Figure 4.8: Influence of the droplet spacing on film morphology consisting of parallel lines on Kapton substrate at 30 °C.

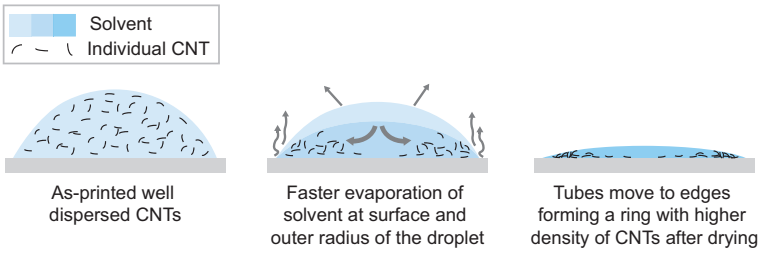

Figure 4.9: Schematic representation of the coffee stain effect after drying of a CNT-ink droptlet.

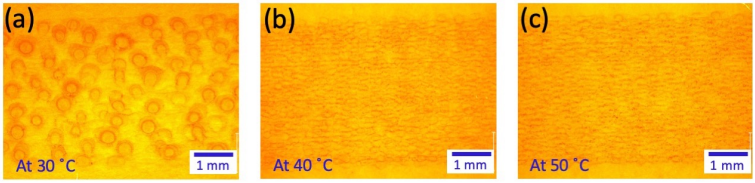

Figure 4.10: Influence of the sintering temperature on the coffee stain effect. Increasing temperature (from (a) to (c)) leads to suppression of the coffee stain effect and a more homogenous film.

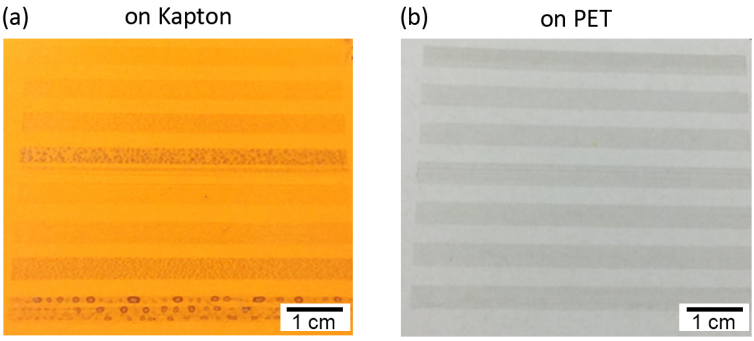

Figure 4.11: Optical images of printed lines from the self-made MWCNT-ink on (a) Kapton and on (b) PET substrate. Best resutls obtained using a droplet spacing of 55 µm and a sintering tempreature of around 60 °C on Kapton substrate, and a droplet spacing of 60 µm and a sintering temperature of 50 °C on PET substrate.

The coffee stain effect (or coffee ring effect) is a phenomenon that occurs during the drying of a droplet on a surface. After drying, a characteristic ring-like deposit forms along the perimeter of the droplet. It is commonly seen in a spill of coffee, or after spilling red wine. A schematic representing the formation process of a coffee-ring for a CNT dispersion is shown in Figure 4.9. The coffee stain effect cannot be avoided entirely. However, the coffee stain effect can be minimized if the evaporation of the CNT-ink is accelerated by higher sintering temperatures. The elevated temperature accelerates the evaporation of the droplet solvent, thus reducing the chance of the migration of CNT particles to the edges. This effect has been observed in the printing tests both on Kapton and PET substrates. Several lines were printed at a fixed droplet spacing of 55 µm, and if the heating temperature was increased from 30 °C to 50 °C, it could be seen that the coffee stain effect was greatly minimized, resulting in improved parallel lines at elevated temperatures (Fig. 4.10). Successful printing has been achieved on Kapton and PET substrates by optimizing the droplet spacing and sintering temperature (Fig. 4.11), since an appropriate droplet spacing can form stable uniform lines, and elevated sintering temperature can reduce the coffee stain effect. A homogenous film consisting of parallel lines with a dimension of 62 mm$\times$4mm on Kapton substrates can be achieved with a droplet spacing of 55 µm and sintering temperature of 60 °C. A homogenous film with the same size on PET substrates can be achieved with a droplet spacing of 60 µm and a sintering temperature of 50 °C.

4.1.3 Sheet resistance of inkjet-printed CNT traces

The sheet resistance or total resistance of the CNT conductive trace is a function of the density of the percolating CNT network. By printing more layers of CNTs, the density of the CNT network can be increased, and the sheet resistance can be further reduced. Thus, the higher the number of printed layers (or printing passes), the lower is the sheet resistance. It is

usually insufficient for good conductivity of CNT conductive traces with printing only one layer of CNTs. For CNT conductive traces consisting of MWCNTs, due to the lower intrinsic conductivity of MWCNTs, more than one layer of CNTs are commonly printed [38].

In this work, stable printing of MWCNTs as conductive trace without clogging can be obtained up to 3 passes (or layers). The average sheet resistance was reduced from 6.3 Megaohms/sq. for 1 pass, to around 2.4 Megaohms/sq. for 2 passes, and further to around 400 Kiloohms/sq. for 3 passes (Fig. 4.12). For practical use, the sheet resistance of the MWCNT conductive traces should be at least smaller than 1000 Ohms/sq., which could be achieved by sequential printing of 5 passes, if the trend in Figure 4.12 is extrapolated to the desired sheet resistance. Unfortunately, it was not possible to print 5 passes for the self-made MWCNT-ink without clogging of the printhead.

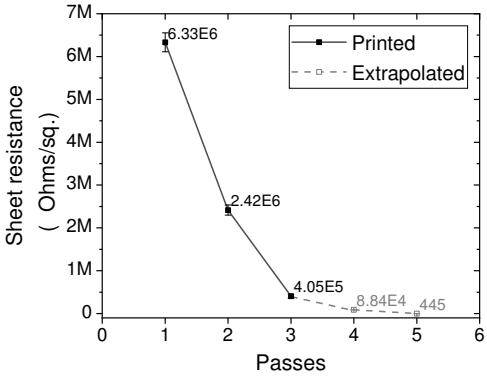

Figure 4.12: Sheet resistance of a printed MWCNT trace as a function of the printing passes.

4.2 Spin-coating of CNT conductive films

4.2.1 Microstructural and cross-sectional characterization

The surface morphology of the spin-coated CNT films is shown in Figure 4.13. Optical images are taken by a confocal laser scanning microscope at nine different locations on the square substrate from the center to the edges and corners. When the nine images are viewed as a whole assembly, it can be seen that circular ridges were formed around the center of rotation (marked with 1). Those ridges were formed due to the rotational shear during the spin-coating process [139].

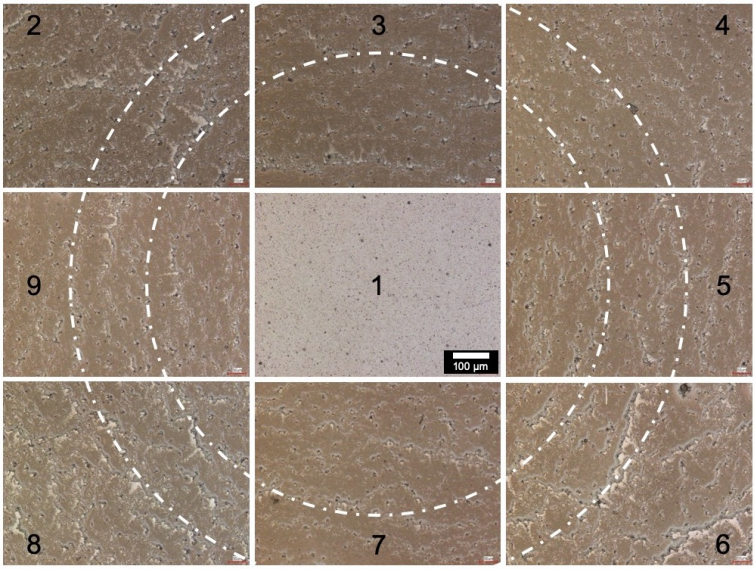

Figure 4.13: Surface morphology of the spin-coated CNT film at nine different locations (marked with numbers from 1 to 9) across the square-shaped substrate.

Before mechanical testing, the surface morphology of the CNT films from batch B1 and B2 (see Table 3.1) was investigated by SEM at higher magnification. Based on the difference in surface morphology, batch B1 and

Table 4.2: Denotation of spin-coated CNT film samples from batch B1 and B2.

Batch	Layer	Batch Name	New name
B1	1	B1_1L	w/ Agg_1L
	2	B1_2L	w/ Agg_2L
	3	B1_3L	w/ Agg_3L
B2	1	B2_1L	w/o Agg_1L
	2	B2_2L	w/o Agg_2L
	3	B2_3L	w/o Agg_3L

B2 are renamed as "w/ Agg" (with agglomerates) and "w/o Agg" (without agglomerates), respectively. Samples with a different number of layers are also renamed accordingly (Table 4.2).

The surface morphologies of 1, 2, and 3-layered CNT films from batch "w/ Agg" and "w/o Agg" are shown in the left and right column of Figure 4.14, respectively. The surface quality of the "w/ Agg" samples was inhomogeneous, and CNT agglomerates can be observed irrespective of the layer number. The CNT agglomerates are bigger and denser on the 3-layered sample than on the 1-layered sample. In comparison, the surface quality of the "w/o Agg" samples has been improved significantly, as shown by the more homogeneous surface. It can be seen that whether on 1-, 2- or 3-layered CNT film, no obvious CNT agglomerates can be found.

In order to determine the thickness of each layer, cross-sections have been prepared by FIB cross-sectional cutting. The cross-sectional micrographs of "w/ Agg_1L", "w/ Agg_/2L", "w/ Agg_/3L", "w/o Agg_1L", "w/o Agg_/2L", and "w/o Agg_/3L" are shown in Figure 4.15. In addition, the thickness of all samples was measured and calculated by ImageJ software and is shown in Figure 4.16. The average thickness for the w/ Agg samples increased from around 285 nm for "w/ Agg_1L", to around 840 nm for "w/ Agg_2L", and further to 1400 nm for "w/ Agg_3L". In comparison, the thickness of

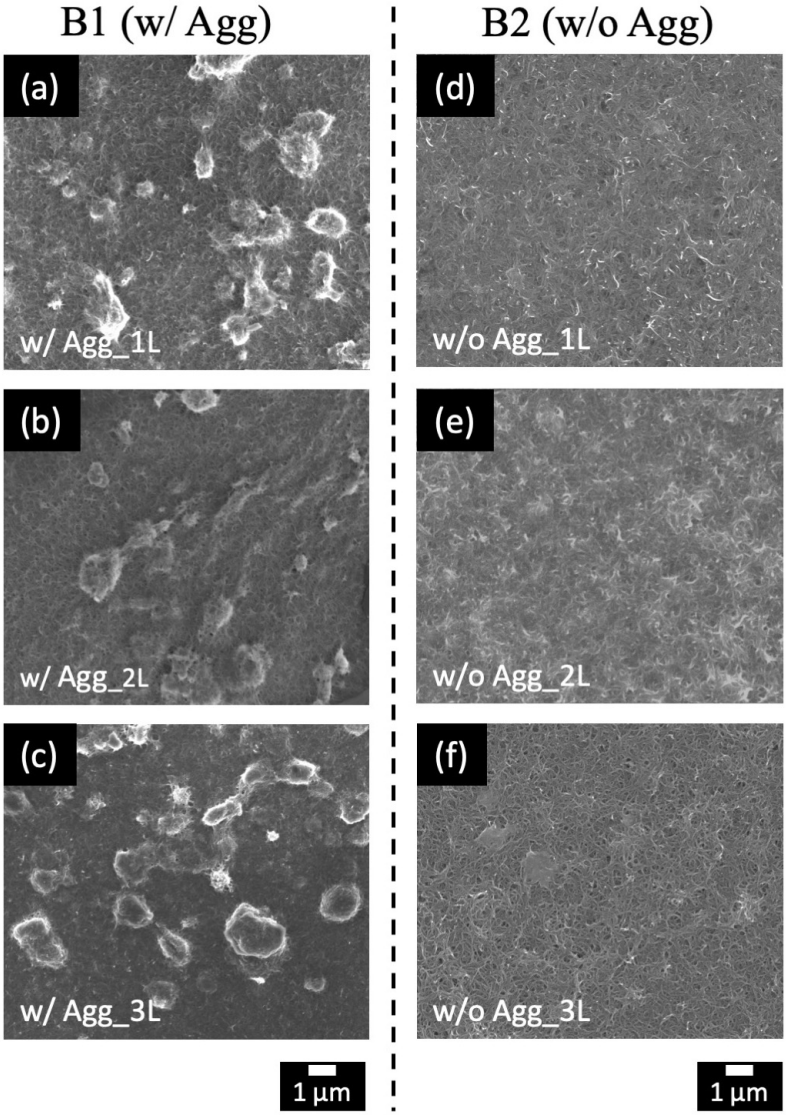

Figure 4.14: Surface morphology of 1, 2, and 3-layered CNT films from batch "w/ Agg" and batch "w/o Agg".

the "w/o Agg" samples increased from around 149 nm for "w/o Agg_1L", to around 159 nm for "w/o Agg_2L", and further to around 168 nm for "w/o Agg_3L". It can be concluded that the overall thickness of "w/o Agg" samples has been significantly reduced due to the elimination of the CNT agglomerates.

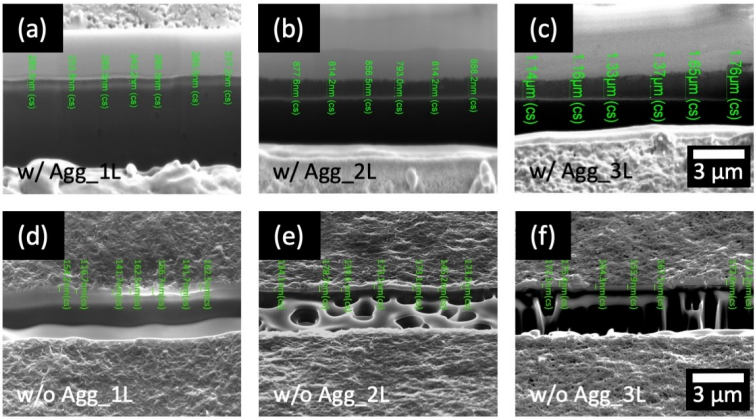

Figure 4.15: Cross-sectional micrographs of (a) w/ Agg_1L, (b) w/ Agg_2L, (c) w/ Agg_3L, (d) w/o Agg_1L, (e) w/o Agg_2L, and (f) w/o Agg_3L.

4.2.2 Sheet resistance of spin-coated CNT films

The sheet resistance of CNT films from batch "w/ Agg" and "w/o Agg" is shown in Figure 4.16. For "w/ Agg" samples, the sheet resistance can be reduced from roughly 3500 Ohms/sq. for "w/ Agg_1L" to roughly 400 Ohms/sq. for "w/ Agg_3L". For "w/o Agg" samples, the sheet resistance of "w/o Agg_1L" is around 6500 Ohms/sq., which is almost two times higher compared to that of "w/ Agg_1L". However, the sheet resistance decreases from "w/o Agg_1L" to "w/o Agg_3L" by a factor of 7, which is similar to the improvement in sheet resistance for the "w/ Agg" samples. It is evident that, whether for CNT films from batch "w/ Agg" or "w/o Agg", the sheet resistance can be significantly reduced by depositing up to 3 layers.

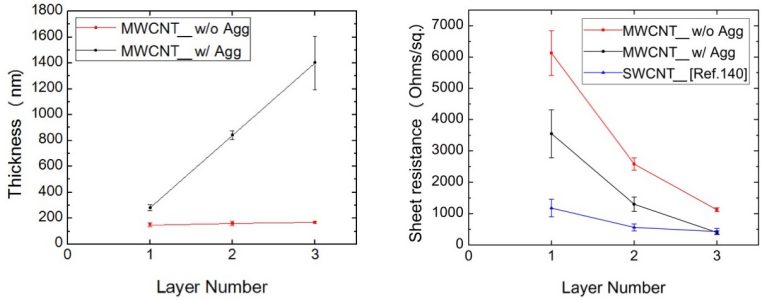

Figure 4.16: Thickness and sheet resistance of the "w/ Agg" samples and the "w/o Agg" samples.

Due to the about 30 times higher intrinsic resistivity of MWCNTs compared to that of SWCNTs (refer to Chapter 2.2), CNT films consisting of SWCNTs possess better conductivity than CNT films consisting of MWCNTs, at least if they are fabricated by a comparable process. However, when comparing the results of this study with literature results, it was found that the sheet resistance of "w/ Agg_3L" can even match the sheet resistance of 3-layered SWCNT films from Kim *et al.*, which were fabricated by inkjet-printing [140].

Table 4.3: Resistivity for each sample from batch "w/ Agg" and batch "w/o Agg".

Sample	**Sheet resistance** ($Ohms/sq.$)	**Av. thickness** (nm)	**Resistivity** ($\Omega \cdot m$)
w/ Agg_1L	3548.07	285.46	0.101
w/ Agg_2L	1299.16	840.62	0.109
w/ Agg_3L	401.89	1401.67	0.056
w/o Agg_1L	6125.63	149.41	0.091
w/o Agg_2L	2579.11	159.54	0.041
w/o Agg_3L	1123.33	168.66	0.018

Based on sheet resistance and average thickness, the corresponding resistivity can be calculated for each sample. It can be seen in Table 4.3 that the resistivity has been decreased from 1 layer to 3 layers for both the "w/ Agg" and "w/o Agg" samples. This comparison manifests that although the sheet resistance of the "w/o Agg" sample is higher than that of the "w/ Agg" sample, their intrinsic resistivity has been significantly improved.

4.3 Discussion

As have been shown in the previous sections, two different fabrication routes have been established for depositing CNTs as patterned lines or thin-films on PET substrates. The commonalities and differences obtained from the two fabrication methods are now summarized and discussed.

4.3.1 Challenges and solutions for inkjet-printing of CNTs

Inkjet printing has been applied as an attempt to fabricate conductive traces from inexpensive industrial-grade MWCNTs. The highlight of this study is that it is the first of its kind where inkjet printing was used as a technique to not only fabricate thin conductive traces from inexpensive and water-based MWCNT-ink but also to extend the print size to a larger pattern (up to 62 mm$\times$4 mm). In this study, the inkjet printing of CNTs has encountered many challenges and exhibited a few limitations. Valuable findings along the complete fabrication route of CNT conductive traces, e.g., from the formulation of CNT-inks to the post-printing treatment, have been achieved. Various aspects affecting the printing results are discussed below in order to explain the reasons why some problems remain challenging.
The final printed results are affected by several aspects, such as average particle size, ink printability, film-forming ability, and conductivity. However, these aspects are interrelated, and trade-offs among them have to be made.

1. **Average particle size**

This first challenge is the control of the average particle size of CNT agglomerates. As a rule of thumb, the average size of particles should be at least 100 times smaller than the nozzle diameter of the printhead. Otherwise, the nozzle of the printhead will be clogged. This problem can be solved in two ways, either reducing the particle size further or choosing a printhead which has a larger nozzle diameter.

The average particle size can be reduced by increasing the power amplitude and time duration of ultra-sonication. In this work, the best result for dispersing CNTs in deionized water was obtained with 5 min long sonication using 100% power amplitude (220 Watt), resulting in average particle size of around 3 µm (Fig. 4.4(a)). Nevertheless, this was not small enough since the printhead used in this work has a nozzle diameter of 70 µm (MD-K-130, Microdrop GmbH, Germany). For a perfect condition, the average particle size of CNT agglomerates should be smaller than 0.7 µm (700 nm). However, the average length of the tubes (Nanocyl® NC7000™ MWCNTs) is already 1.5 µm. The length of the tubes could cause clogging since some tubes could be even longer than 1.5 µm. Partial clogging of a few tubes can readily cause instable jetting of droplets. One solution would be cutting the length of the tubes further by applying much higher sonication energy and longer sonication time, but there is no guarantee that most tubes would be cut into a length that is less than 0.7 µm. Moreover, the reduction in length of the tubes would effectively reduce the average particle size of CNT agglomerates in the ink, but would adversely reduce the aspect ratio of the CNTs, which instead brings disadvantages for the conductivity of the printed traces. When the average particle size of CNT agglomerates cannot be further reduced, a printhead with a larger nozzle diameter can be considered. For example, for solving the clogging issue in this work, a printhead with 100 µm nozzle diameter (MD-K-140, Microdrop GmbH, Germany) would be recommended. However, the rheological properties of the CNT-ink would have to be readjusted again. For a stable droplet formation, it would require

a much higher viscosity of the CNT-ink to be compatible with a 100 µm printhead. Otherwise, the CNT-ink fluid would drip out the nozzle rather than jet out from the nozzle. In order to meet the requirement of a printhead with a larger diameter, increasing the viscosity of the CNT-ink is even more challenging. This was the essential reason why the printhead with 70 µm was chosen in this study.

2. **Ink printability**

The second challenge is the tailoring of the ink printability. The ink printability can be quantitatively calculated by the Ohnesorge number or the Z number (refer to Chapter 2.2). The printability is mainly influenced by the ink fluidic properties such as viscosity and surface tension.

The viscosity determines whether an initial droplet can be jetted. For the chosen printhead with 70 µm nozzle diameter, the viscosity should be at least larger than 2 cP. In the tested inks shown in Table 4.1, only "A3R" and "SelfMade02" suffice this requirement (Fig. 4.6(a)). For an aqueous ink of CNTs, the viscosity can be increased in three ways. Firstly, the viscosity of water-based CNT-inks can be increased by increasing the weight loading of the surfactant, as shown in Figure 4.4(b). In this work, the self-made MWCNT-ink-"SelfMade02" (0.1 wt%) has a viscosity of 1.95 cP, due to the increased loading of SDS to 3 wt%. However, higher loadings of SDS than 3 wt% can lead to severe foaming (Fig. 4.2(a)). Secondly, increasing the loading of CNTs can also increase the viscosity. When the loading of CNTs is increased higher than 0.1 wt%, the viscosity of the self-made MWCNT-ink can be further increased (Fig. 4.5). However, increased loading of CNTs would make the dispersing challenging. An ultra-sonication power up to 750 Watt would be required to disperse MWCNT-inks with loading as high as 1.0 wt% effectively [38]. Unfortunately, a sonication setup with such a high power was not available in this work. Besides, if the average particle size of CNT agglomerates is still large, it would also aggravate the clogging issue. The third way to increase the viscosity of CNT-inks is to add rheol-

ogy modifiers, which can densify the aqueous solution. However, rheology modifiers are mostly organics and are hard to remove after printing. This will deteriorate the conductivity of the CNT film.
The surface tension determines whether an ink would break apart from the perimeter of the nozzle and wet the substrate sufficiently. The surface tension further influences the contact angle and the wetting behavior of the droplet on the substrate. In this work, the surface tension of the tested inks is always smaller than the surface energy of the Kapton and PET substrate (Fig. 4.6(b)).

3. **Film-forming ability**
The third challenge is related to adjusting of the film-forming ability, or the solidification of the printed traces after drying. The solidified morphology is influenced by the droplet spacing, coffee-stain effect, and sintering temperature. An optimal morphology can only be obtained when all these parameters are optimized.
It has been shown that a droplet spacing of roughly 60 µm result in uniform lines at a sintering temperature of 30 °C (Fig. 4.8). When an elevated sintering temperature higher than 30 °C is applied, the droplet spacing can be reduced accordingly. Because water molecules evaporate faster at a higher temperature, the droplets can be placed closer to each other. The coffee-stain effect can also be greatly suppressed by elevating the sintering temperature. After systematic printing tests, it has been found that an appropriate sintering temperature for water-based CNT-inks is around 50-60 °C (Fig. 4.10) depending on the chosen polymer substrate. These experimental results have proven that when the right combination of droplet spacing and sintering temperature is applied, a uniform line with straight edges can form. Moreover, this optimal formation of a single line is necessary for printing larger patterns, as shown by the two samples printed on Kapton and PET in Figure 4.11. A homogenous film consisting of parallel lines with a dimension of 62 mm×4mm on Kapton substrate can be achieved with a

droplet spacing of 55 µm and a sintering temperature of 60 °C, whereas a homogenous film with the same size on PET substrate can be achieved with a droplet spacing of 60 µm and a sintering temperature of 50 °C.

4. **Conductivity versus the number of printed layers**

The fourth challenge is to increase the electrical conductivity of the printed CNT conductive traces. When the previous factors, such as loading of CNTs, average particle size, ink printability, and film-forming ability are optimized, the resulting conductivity for a single printed layer of CNT is predetermined. The only way to increase the conductivity is by printing more passes (or layers) of CNTs on top of the initial layer. This method has also been adopted in the literature for fabricating conductive traces and electrodes from SWCNTs [140] and MWCNTs [38] using the inkjet printing technique.

In this work, it has been shown that stable printing of CNTs can be obtained up to 3 layers. However, the sheet resistance of the 3-layer printed CNT trace is still too high (Fig. 4.12). The reasons for the poor conductivity can be explained as follows (Fig. 4.17). With only 1 pass printing, the sheet resistance is exceptionally high, due to the low loading of only 0.1 wt% of CNTs in the ink. Because of the low loading, the density of the CNT network is very low, and no percolating network of CNT is formed. With 2 passes of printing, the sheet resistance is still close to an insulator, and the CNT network was still not conductive. With 3 passes of printing, the sheet resistance is still around 400 Kiloohms/sq. (Fig. 4.12). This trend indicates that the sheet resistance can be continuously reduced if more CNT layers could be printed. Unfortunately, time-dependent clogging of the printhead was unavoidable, and the number of layers to be printed was limited to 3. However, an extrapolation based on the printed results shows that a sheet resistance of smaller than 440 Ohms/sq. can be realistically achieved if more than 5 passes (or layers) of CNTs can be printed without the clogging issue.

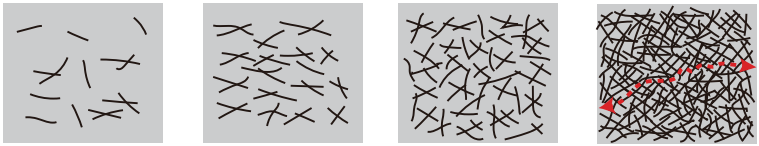

Figure 4.17: Schematic illustrating the formation of a percolating CNT network with increasing CNT density (from left to right). The CNT density increases with the number of printed layers. A conducting path (marked by the red dashed line) can be established when the number of printed layers is high enough.

4.3.2 Issues concerning spin-coating of CNTs

As an established method, spin-coating has resulted in stable and consistent results, which are advantageous for large-area coating. However, some essential aspects of depositing CNT films by spin-coating are summarized in the following.

1. Tolerant to CNT-ink properties

Spin-coating is tolerant to the properties of CNT-inks, such as average agglomerate size, viscosity, and weight loading. Firstly, though agglomerates of CNTs in the ink should be avoided, they do not deteriorate the spin-coating process itself. Secondly, it was not necessarily required to increase the viscosity of the CNT-ink too much. The rotation velocity can be adjusted according to the viscosity of the CNT-ink. If the viscosity is low, then the rotation velocity can be reduced. Thirdly, higher weight loading of CNTs up to 3 wt% can be coated. In this work, a loading as high as 1 wt% of CNTs (Nanocyl® Aquacyl™ AQ0101) can be successfully coated, even on an area as large as 70 mm$\times$70 mm.

2. Surface morphology improvement

Inherent to the spin-coating process, the film morphology of spin-coated CNT films is not perfectly homogeneous but is radially oriented [139]. This inhomogeneity mainly appeared on the edges and corners of the spin-coated film. This effect is unavoidable during the spin-coating of CNT-ink and would be further enhanced if large CNT agglomerates are existing in the CNT-ink. If the large CNT agglomerates in the CNT-ink can be removed, the homogeneity of the spin-coated CNT film would be significantly improved. This improvement was evidenced by a comparison of the surface morphology between batch "w/ Agg" and batch "w/o Agg". Since no pre-treatment was carried out for the "w/ Agg" samples before spin-coating, many CNT agglomerates, which formed during the storage of the commercial ink, were deposited onto the PET substrate during spin-coating. After spin-coating, many apparent CNT agglomerates in the size of 0.5 µm to around 10 µm appeared within the CNT film (Fig. 4.14 left). Compared to that, if the pre-treatment, including ultra-sonication and centrifugation of the commercial ink, was carried out before spin-coating, large CNT agglomerates could be removed, and no CNT agglomerates were found within the CNT film of the "w/o Agg" samples (Fig. 4.14 right). Even in the border and corner regions of the PET substrate, a homogenous CNT film without agglomerates was achieved.

3. Conductivity versus the number of layers

The CNT films can be over-coated multiple times, which can significantly reduce the sheet resistance, or equivalently increase the total conductivity (Fig. 4.16). For the "w/ Agg" samples, the sheet resistance can be reduced to around 400 Ohms/sq. with up to 3 layers of coating. In comparison, for the "w/o Agg" samples, the sheet resistance was reduced to around 1.1 Kiloohms/sq. with up to 3 layers of coating (Table 4.3). The difference in sheet resistance between the "w/ Agg_3L" sample and the "w/o Agg_3L" sample is due to the much higher thickness of the "w/ Agg_3L" sample. The

existence of CNT agglomerates contributes to the lower sheet resistance of the "w/ Agg" samples.

Table 4.4: The ratio of the resistivity of the "w/ Agg" sample to the resistivity of the "w/o Agg" sample for the same number of layers.

Layer number	$\rho_{w/Agg}$ $(\Omega{\cdot}m)$	$\rho_{w/oAgg}$ $(\Omega{\cdot}m)$	$\frac{\rho_{w/Agg}}{\rho_{w/oAgg}}$
1L	0.101	0.091	1.11
2L	0.109	0.041	2.66
3L	0.056	0.018	3.11

The resistivity of the CNT films from both batches is shown in Table 4.4. It can be seen that, for both batches, the resistivity $\rho_{w/Agg}$ and $\rho_{w/oAgg}$ decreased from 1-layer up to 3-layers. This implies that, although the thickness of 3-layered CNT films is the highest within each batch, their intrinsic resistivity is the lowest. In other words, the intrinsic conductivity of the CNT films can be significantly improved through multiple layer coating.

The ratio of the resistivity of the "w/ Agg" sample to that of the "w/o Agg" sample $\frac{\rho_{w/Agg}}{\rho_{w/oAgg}}$ has been also compared (Table 4.4). It can be seen that the ratio becomes larger, with an increasing number of coated layers. This comparison has quantitatively proven that, for the same number of layers, the "w/o Agg" samples possess higher electrical conductivity than that of the "w/ Agg" samples. Thus, it can be concluded that the removal of large CNT agglomerates is not only beneficial to the film homogeneity but also improves the intrinsic conductivity of the spin-coated CNT films. The improvement of intrinsic conductivity due to more coating layers is correlated with the density of the CNT network. By depositing more layers, the density of the CNT network in thicker films is much higher than that in the thinner films, resulting in a reduction of both intrinsic resistivity and sheet resistance.

5 Micro-tensile testing of CNT conductive films

5.1 Mechanical behavior of polymeric substrates in tension

5.1.1 Surface quality of polymeric substrates

The surface quality and morphology of polymeric substrates play an important role in the coating process and electro-mechanical testings, including micro-tensile tests and bending fatigue tests [141]. Therefore, the surface condition of the PET substrate was investigated in order to assess the quality of the as-received commercial PET substrates.

PET films are usually prepared by a process whereby the amorphous cast is drawn in both the forward direction (machine direction) and transverse direction [21]. The type of PET substrates used in this work is DuPont Melinex® ST504 (thickness: 125 μm), and the substrates are delivered in the size of A4 paper. The long side of the substrate is in the forward direction, and the short side of the substrate is in the transverse direction. In addition, an adhesion primer layer consisting of inorganic particles on the surface has been coated by the manufacturer, to offer several benefits, such as improved wettability due to surface roughness and enhanced adhesion [21].

The surface condition of the top face treated with the primer layer on Melinex®ST504 has been investigated by A. Pietrikova, *et al.*, and a surface roughness of 0.045 μm has been reported [129]. The same type of PET substrates was also characterized in this work. The micrographs of their surface

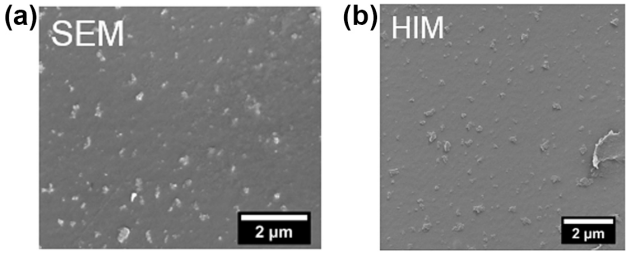

Figure 5.1: Surface morphology of as-received commercial PET films (DuPont Melinex® ST504, 125 µm thickness) under (a) SEM and (b) HIM, respectively.

morphology by SEM and HIM are shown in Figure 5.1. The presence of small particles on the surface can be observed [21]. The micrographs show that the surface morphology of the as-received PET films is not perfectly homogeneous.

5.1.2 Tensile behavior of polymeric substrates

In order to investigate the stretchability of PET substrates, they have been tested by tensile testing. Two batches of bare PET substrates (Melinex® ST504 with 125 µm thickness) were cut into 25mm×8mm rectangular stripes. The first batch was stretched along the forward direction, whereas the second batch was stretched along the transverse direction. The tensile test results for both batches are shown in Figure 5.2.

The results showed that PET substrates could be stretched over 50% strain along the forward direction and up to 40% strain when stretched along the transverse direction. However, the elastic limit of the PET substrate is found to be only around 3%. It was shown that the stretchability of the PET substrates is dependent on the stretching direction. The PET substrates are more ductile in the forward direction than in the transverse direction, whereas the fracture load of the PET substrates is higher due to a stronger hardening of PET in the transverse direction. Irrespective of the direction, they can be stretched to an average strain of roughly 40%. For ensuring a stretchability

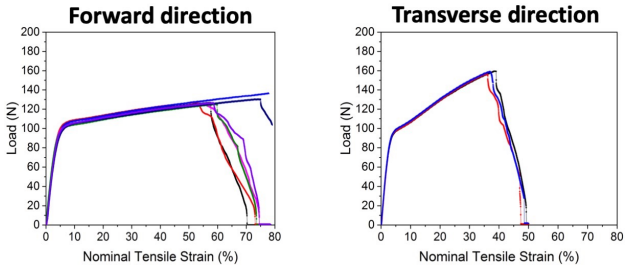

Figure 5.2: The load-strain curves of PET substrates stretched along the forward direction (left), and the transverse direction (right). The PET substrates show more ductility in the forward direction and stronger hardening effect in the transverse direction.

up to 50% strain, electro-mechanical testings of CNT conductive films have always been conducted along the forward direction of the PET substrates. To characterize the surface morphology evolution of bare PET substrates during stretching, *in-situ* tensile tests along the forward direction have been conducted inside the SEM (Fig. 5.3). The observed area on the PET substrate has always been kept the same, and the surface morphology has been recorded by applying the LV-SEM mode (refer to Chapter 3.3.1). It can be seen that the surface of the PET substrate remains intact up to 50% strain, and no strain localization and crack formation could be found.

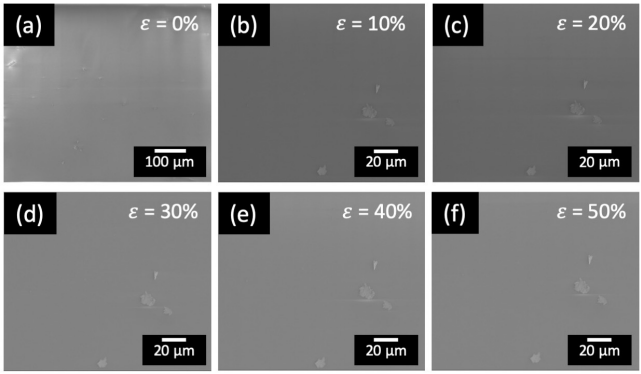

Figure 5.3: Surface morphology evolution of a PET substrate recorded *in-situ* for different tensile strains.

5.2 Tensile behavior of CNT conductive films

Micro-tensile tests with *in-situ* electrical resistance measurement have been conducted on samples from batch "w/ Agg" and batch "w/o Agg", in order to investigate their electro-mechanical behavior at large tensile strains. For avoiding the influence of the drawing direction in PET substrates, the samples have always been stretched along the forward direction of the PET substrates (refer to Chapter 5.1.2). After testing, their surface morphologies were characterized by SEM imaging for comparison and analysis. Furthermore, *in-situ* micro-tensile testing inside the SEM has been conducted for revealing the microstructural evolution of the CNT films during tensile loading.

5.2.1 Electro-mechanical testing

Samples from both "w/ Agg" and "w/o Agg" batches were stretched to 50% strain, while their corresponding resistance change was measured simultaneously. Thereby, the relative change in resistance (or fractional resistance) $\frac{\Delta R}{R_0}$ versus applied tensile strain ε can be determined. This relationship can

be described by the resistance-strain curve ("R-S curve"). The R-S curves for the "w/ Agg" and "w/o Agg" samples are shown in Figure 5.4.

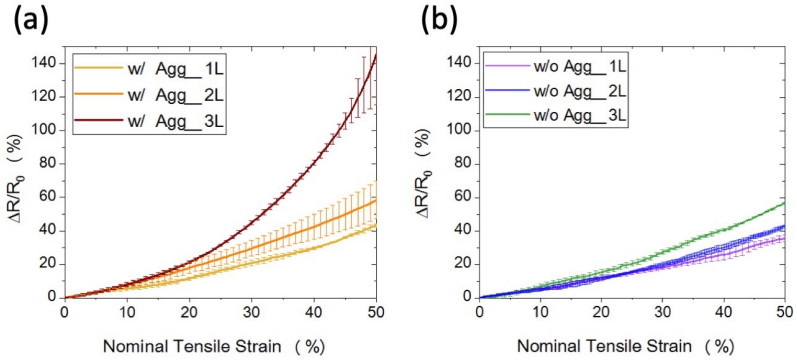

Figure 5.4: Resistance-strain curves for the 1-, 2-, and 3-layered "w/ Agg" and "w/o Agg" samples stretched from 0% to 50%.

The change in fractional resistance of the "w/ Agg" samples (Fig. 5.4(a)) is different from that of the "w/o Agg" samples (Fig. 5.4(b)). The R-S curve of the "w/ Agg_1L" sample evolved linearly and showed around 40% increase in fractional resistance at 50% strain. The R-S curve of the "w/ Agg_2L" sample also evolved linearly to 10% and started to deviate from the R-S curve of the "w/ Agg_1L". The "w/ Agg_2L" sample showed 60% increase in fractional resistance at 50% strain. The R-S curve of the "w/ Agg_3L" sample exhibited the most dramatic behavior. Its fractional resistance increased non-linearly, starting from roughly 19% strain, and showed more than 140% increase in fractional resistance up to 50% strain. Likewise, the R-S curves of the "w/o Agg" samples exhibited a similar trend for 1-, 2-, and 3-layered samples. However, the increase in fractional resistance of the "w/o Agg" samples are much lower than that of the corresponding "w/ Agg" samples. For the "w/o Agg_1L" sample, its R-S curve evolved linearly and showed only around 35% increase in fractional resistance at 50% strain, which is considerably lower compared to that of the "w/ Agg_1L"

sample. For the "w/o Agg_2L" sample, its R-S curve also evolved linearly and increased slightly higher above the R-S curve of the "w/o Agg_1L" sample at roughly 30% strain. The "w/o Agg_2L" sample showed around 42% increase in fractional resistance at 50% strain, which is again lower than that of the "w/ Agg_2L" sample. The R-S curve of the "w/o Agg_3L" sample evolved linearly from the beginning and increased higher above the R-S curves of the "w/o Agg_1L" and "w/o Agg_2L" samples starting from roughly 10% strain. The R-S curve of the "w/o Agg_3L" increased further in a non-linear fashion and showed around 58% increase in fractional resistance at 50% strain. For this batch, the "w/o Agg_3L" sample exhibited the highest increase in fractional resistance but is still lower than that of the "w/ Agg_3L" sample.

Interestingly, it should be noted that the "w/ Agg" and "w/o Agg" samples exhibited three characteristic electro-mechanical behaviors during tensile straining. First, the R-S curves coincided with each other below 10% strain and started to deviate from each other at higher strains. Also, the deviation of the R-S curves is different for 1-layered, 2-layered, and 3-layered samples. Second, for 1-layered and 2-layered samples in both batches, their R-S curves increased linearly. At 50% strain, the increases in fractional resistance of these samples are smaller than 50%, resulting in a GF smaller than one, which is a very astonishing result. Lastly, for the "w/ Agg_3L" and "w/o Agg_3L" samples, their R-S curves both deviated from the R-S curves of the 1-layered and 2-layered samples and increased non-linearly at higher strains. Moreover, they both exhibited the highest increase in fractional resistance within their batch. The stronger increase in fractional resistance at higher strains for the "w/ Agg_3L" and "w/o Agg_3L" samples is ascribed to local damage formation in the CNT network.

5.2.2 Microstructural characterization

The surface morphologies of 1-, 2-, and 3-layered samples from the "w/ Agg" and "w/o Agg" batches were analyzed in the SEM after micro-tensile testing up to 50% strain. The SEM micrographs of the "w/ Agg" samples after testing are shown in the left column of Figure 5.5. Formation of many open cracks can be found on the samples from batch "w/ Agg". The cracks were oriented orthogonal to the tensile direction and were formed at the edges and within CNT agglomerates. The SEM micrographs of the "w/o Agg" samples after testing are shown in the right column of Figure 5.5. Their surface morphologies revealed no open cracks or damage after testing up to 50% strain. Compared to the open cracks in the "w/ Agg_3L" sample (Fig. 5.5(c)), the appearing tiny dimples in the "w/o Agg_3L" sample (Fig. 5.5(f)) are not cracks but result from local necking.

The CNT films fabricated in this study consist of the CNT network itself and the matrix, which is the remained organics from the commercial CNT dispersion. This feature of the CNT films can be better revealed from their cross-sections. Cross-sections through the crack location have been prepared by FIB milling (refer to Chapter 3.3.1), to reveal and compare the difference in cross-sectional crack morphology between the "w/ Agg_3L" sample and the "w/o Agg_3L" sample. The cross-section of a representative major crack formed in an agglomerate of the "w/ Agg_3L" sample is shown in Figure 5.6(a). Its cross-section revealed that the crack width is about 0.2-0.5 μm wide, and the crack formed through the cross-section of the CNT film (marked by the white arrow), where a CNT agglomerate was previously located. The crack opening is so large that only a few CNTs bridged across the crack (marked by red arrows). In comparison, the cross-section of a tiny dimple found in the "w/o Agg_3L" sample is shown in Figure 5.6(b). Its cross-section showed that the tiny dimples only formed on the surface due to the local necking underneath (marked by white arrows). The width of the tiny dimple is in the range of 100 nm to 200 nm. Moreover, it can

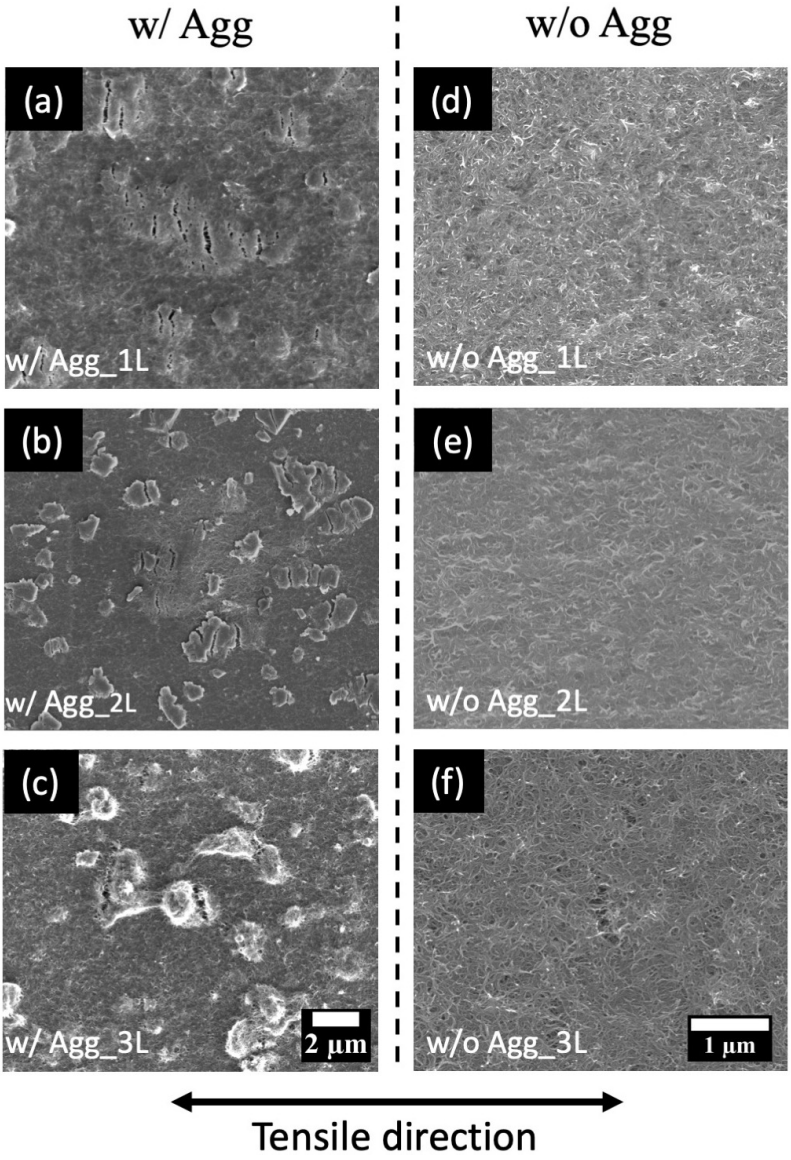

Figure 5.5: Surface morphology revealed by SEM imaging after tensile testing up to 50% strain for (a)-(c) "w/ Agg" samples and (d)-(f) "w/o Agg" samples, respectively. The scale bar for the left and the right column is 2 μm and 1 μm, respectively.

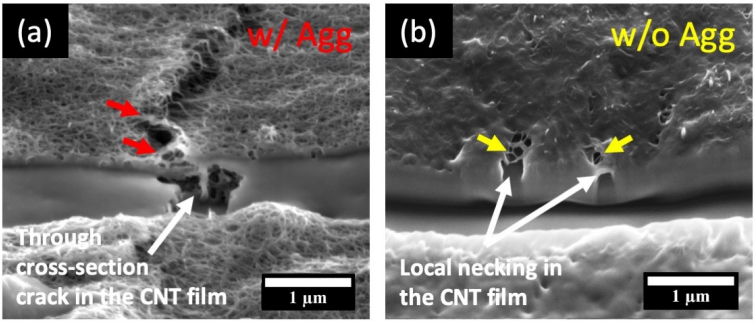

Figure 5.6: FIB cross-sections of (a) a crack in a "w/ Agg_3L" sample and (b) tiny dimples in a "w/o Agg_3L" sample, respectively.

be observed that the CNTs are still intact and bridge across the tiny dimple (marked by yellow arrows).

5.2.3 *In-situ* micro-tensile testing inside the SEM

In order to investigate the mechanism of the rapid increase in fractional resistance of the "w/ Agg" batch, and to correlate the microstructural change with a specific strain level, *in-situ* micro-tensile testing inside the SEM on the "w/ Agg_3L" sample has been conducted. The microstructural evolution has been recorded while the sample was being stretched by the micro-translational stage (refer to Chapter 3.3.2). SEM micrographs were taken stepwise from 0% to 60% tensile strain.

The surface morphologies of the "w/ Agg_3L" sample at each strain level are shown in Figure 5.7. It can be seen that no crack formation occurred up to 5% strain. Starting from 10% strain, a few tiny cracks (marked by red arrows) were formed orthogonal to the tensile direction, mainly within individual and larger agglomerates. The cracks grew larger when the sample was stretched further to 20% strain. At 30% strain, the cracks grew not only larger but also additional cracks were formed. The very bright contrast inside a few cracks (marked by red circles) is due to the increasing crack

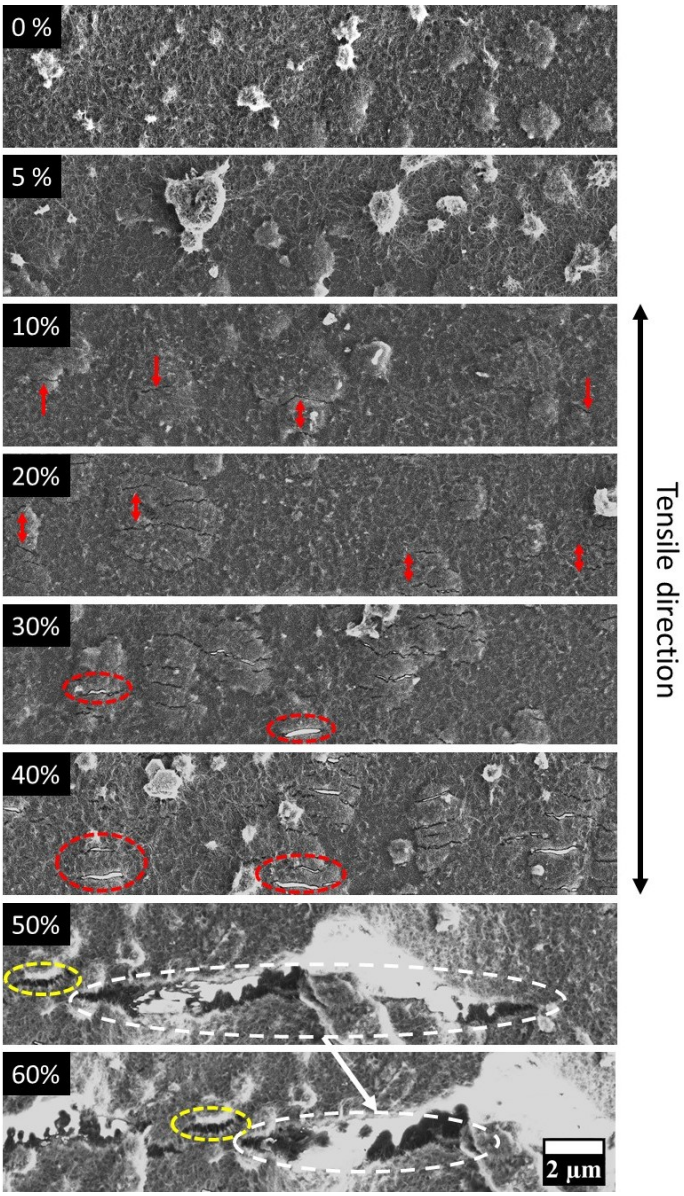

Figure 5.7: Microstructural evolution of the "w/ Agg_3L" sample recorded *in-situ* inside the SEM during straining from 0% to 60%.

opening and charging of the polymer substrate at the bottom of the crack. At 40% strain, more such cracks with the charging effect can be observed. It is worth noting that not every crack will grow bigger and longer at higher strains. This is evidenced by the crack morphology at 50% strain. A very large crack (marked by the white circle) was found in the sample. Its length is more than 10 μm, and its width is roughly 1 μm. Next to this huge crack, a much smaller crack (marked by the yellow circle) was found. Inside this crack, CNTs were found to bridge across both sides of the crack. At 60% strain, the same huge crack has grown even bigger, as shown by the wider opening. Such huge cracks were only found to exist locally on the sample and did not channel through the sample width (perpendicular to tensile direction). Thus, these local cracks did not shut down the electrical conduction of the CNT network. The conductivity of the sample did not alter significantly (roughly 1.4 times higher than the initial value at 50% strain, Fig. 5.4), even with the existence of these huge cracks and many tiny cracks. During the *in-situ* micro-tensile testing inside SEM, the microscopic view of the whole straining area of the sample was also recorded stepwise from 0% to 50%, and the transverse width can be measured. The width of the sample at 0% strain and 50% strain were compared against each other in Figure 5.8. It can be seen that the width in the middle section of the sample has been reduced from 1.10 mm at 0% strain to 1.02 mm at 50% strain. This minimization in width is due to the plastic deformation and necking of the PET substrate under large tensile strains. The necking process has caused a transverse contraction of the PET substrate and a reduction in width. It will be discussed later, whether if the necking process of the PET substrate affects the electrical conductivity of the CNT network.

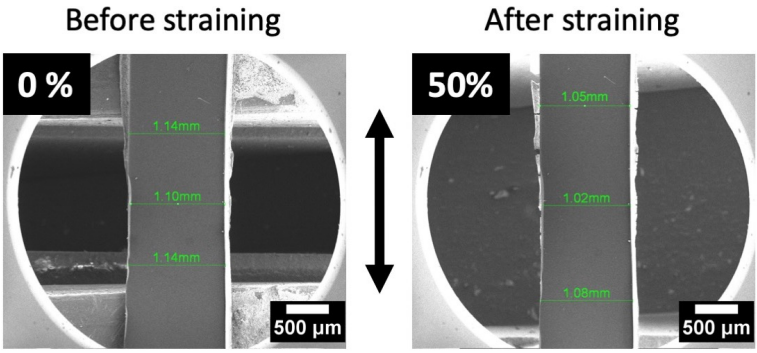

Figure 5.8: Transverse contraction of the PET substrate after straining to 50%, the straining direction is represented by the black arrow.

5.2.4 Electro-mechanical behavior during loading and unloading

In order to investigate the influence of strain on the reversibility of the electrical conductivity, micro-tensile tests with loading and unloading segments were conducted for three different strain ranges: 0%-3%, 0%-5%, and 0%-50%, respectively. Firstly, the reversibility of a "w/o Agg_1L" sample under repetitive loading-unloading condition below 5% strain was investigated, since the elastic limit of the PET substrate is below 5% (Fig. 5.2). Afterwards, the reversibility of the same sample was tested within 50% strain, which is far beyond the elastic limit of the PET substrate.

Two "w/o Agg_1L" samples were stretched and released from 0% to 3% strain and from 0% to 5% strain for six times, respectively. The corresponding R-S curves are shown in Figure 5.9. It can be seen that upon each loading, the fractional resistance increased linearly, and upon each unloading, the fractional resistance decreased again but never recovered entirely to the initial value. No matter for stretching cycles between 0% to 3% strain or between 0% to 5% strain, the final fractional resistance had migrated stepwise

to a slightly higher resistance value, when the load was released from every cycle.

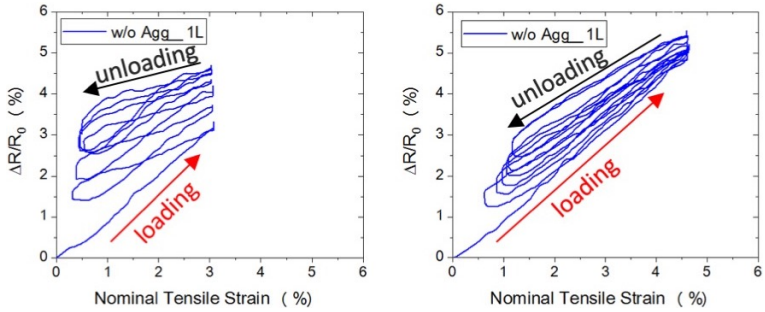

Figure 5.9: Resistance-strain curves for a "w/o Agg_1L" sample under repetitive loading and unloading from 0% to 3% strain and from 0% to 5% strain, respectively.

Five "w/o Agg_1L" samples were stretched from 0% to 50% strain, and then they were immediately reversed to 40% strain, at which the load on the samples was released entirely. Their corresponding R-S curves are plotted in Figure 5.10. All five samples showed reproducible electro-mechanical behaviors, as indicated by the overlapping R-S curves during loading. The fractional resistance upon loading to 50% strain increased almost linearly. Upon unloading from 50% strain to around 48% strain, the fractional resistance followed along the R-S curve during loading, indicating that the fractional resistance can be partially recovered. However, during continuous unloading below 48% strain, the decrease in fractional resistance stagnated and remained at around 38% increase after the samples were completely unloaded.

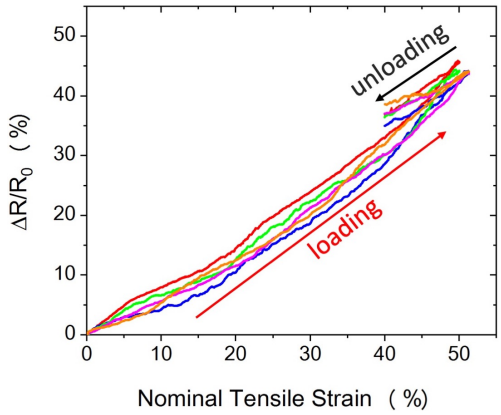

Figure 5.10: Resistance-strain curves for a "w/o Agg_1L" sample during loading and unloading between 0% to 50% strain.

5.3 Discussion

5.3.1 Resistance-strain relationship during straining

The resistance-strain relationship of the "w/ Agg" and "w/o Agg" samples during straining differ from that of typical metallic conductive films on compliant substrates [30, 95]. Two different theories are discussed here, in order to explain the specific electro-mechanical behavior of CNT-based conductive films. Two curves representing the two theories are shown in Figure 5.11. The first theory based on the assumption of a constant resistivity and sample volume during elongation was already introduced as equation 2.8 in Chapter 2.3. Its corresponding curve is named as "Constant volume" and is represented by the red curve.

Due to the low bending stiffness of individual CNTs and the CNT network, CNTs are only shifted laterally upon tensile elongation. Even if the cross-section of the entire CNT film decreases, the cross-section of individual CNTs should remain constant in the cross-section of the CNT film. Thus, a new assumption for CNT thin-films can be made: the resistivity of the

whole CNT network is constant ($\rho = \rho_0$), and the effective cross-section of the whole CNT network (all CNTs) does not change ($A = A_0$) during tensile straining.

Based on the definition of electrical resistance, the fractional resistance $\frac{\Delta R}{R_0}$ can be written as:

$$\frac{\Delta R}{R_0} = \frac{R - R_0}{R_0} = \frac{\rho \frac{L}{A} - \rho_0 \frac{L_0}{A_0}}{\rho_0 \frac{L_0}{A_0}}. \tag{5.1}$$

Since $\rho = \rho_0$ and $A = A_0$, $\frac{\rho}{A}$ equals to $\frac{\rho_0}{A_0}$, and these two terms in equation 5.1 are cancelled out, given:

$$\frac{\Delta R}{R_0} = \frac{L - L_0}{L_0} = \frac{\Delta L}{L_0} = \varepsilon_{tech}. \tag{5.2}$$

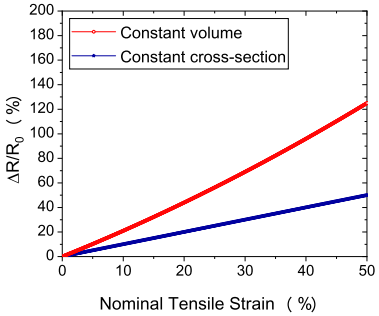

Figure 5.11: Two theoretical curves representing the relationship between the fractional resistance $\frac{\Delta R}{R_0}$ and the nominal tensile strain based on two different assumptions: "Constant volume" (red curve) and "Constant cross-section" (blue curve), respectively.

Besides, the intrinsic resistance of an individual CNT can be assumed constant: $R = R_0$, since the effective length and the cross-section of an individual CNT do not change upon stretching. However, this does not imply that the total resistance of the whole CNT network does not change upon stretch-

ing. In a realistic CNT film, no matter how individual CNTs are deformed, the whole CNT network is elongated due to the streching of the substrate. Equation 5.2 gives a linear relationship between the fractional resistance $\frac{\Delta R}{R_0}$ and the applied strain ε_{tech}, and the corresponding curve is named as "Constant cross-section" and is represented by the blue curve. Under the "Constant cross-section" assumption and if equation 5.2 is described in terms of gauge factor (GF), then the GF value of CNT-based conductive films equals to one. It should be noted that equation 5.2 is originally proposed in this doctoral study and has not been reported yet in the literature. The "Constant volume" and "Constant cross-section" curves set two boundary conditions for the "w/ Agg" and "w/o Agg" samples, respectively. The "Constant volume" curve has a gauge factor of 2 and fits better with crystalline materials, such as metal films or semiconductor films, and it is the theoretical limit for such films [30, 95]. Any higher measurement value means that damage formation occurs in the film. The "Constant cross-section" curve indicates the lower limit for the CNT film, as long as its intrinsic resistivity remains constant. When a measured curve lies above this curve, it means that there would be damage formation in the CNT network. However, when a measured curve lies below this curve, it indicates that the intrinsic resistivity of the CNT network must have been decreased during tensile straining.

The resistance-strain (R-S) curves of the "w/ Agg" and "w/o Agg" samples are compared with each other and also to the two theoretical curves. The comparison for the whole strain range and the strain range between 0%-20% are shown in Figure 5.12. Two phenomena regarding the R-S relationship during loading can be observed.

Firstly, it is surprisingly found that the R-S curves of most samples evolved even blow the "Constant cross-section" curve (marked by the blue-dashed line in Fig. 5.12(a)). Only the R-S curves of a few samples: including "w/ Agg_2L", "w/ Agg_3L" and "w/o Agg_3L", showed a deviation higher above the "Constant cross-section" curve at larger tensile strains. The R-S curve of the "w/ Agg_3L" sample started to deviate from the theoretical

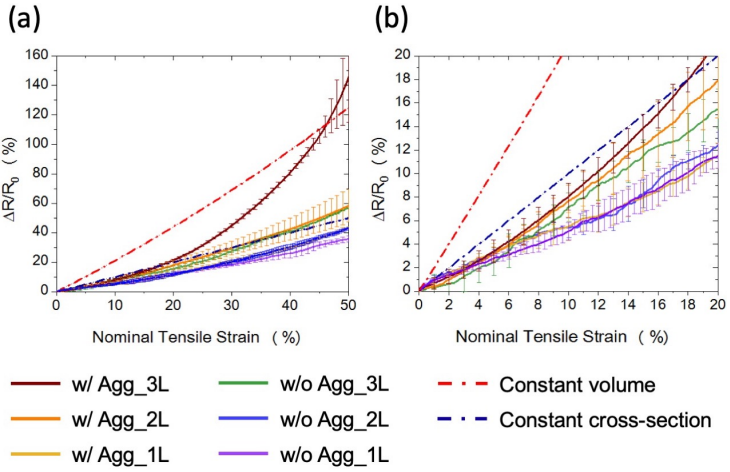

Figure 5.12: Comparison of resistance-strain curves for the "w/ Agg" and "w/o Agg" samples with two theoretical curves in (a) the whole strain range of 0%-50%, and (b) the enlarged strain range of 0%-20%.

curve at around 19% strain and showed the most dramatic increase among all the tested samples up to 50% strain. For the "w/ Agg_2L" and "w/o Agg_3L" samples, their R-S curves deviated from the blue theoretical curve at around 40%, and the increase in fractional resistance is much lower than that of the "w/ Agg_3L" sample. The deviation of the R-S curves above the theoretical curve for the three samples is related to the damage formation in the CNT network. The difference between the R-S curves of the above samples indicates that the damage formation in the "w/ Agg_3L" sample could be more severe than that in the "w/ Agg_2L" and "w/o Agg_3L" samples, which will be further discussed later.

Secondly, the strain range below 20% raised special interests (Fig. 5.12(b)). It has been found that the R-S curves of all samples evolved below the theoretical "Constant cross-section" curve within this range. However, the trend of the R-S curves for all samples should still be distinguished in the strain range of 0%-3% and 3%-20%. In the strain range of 0%-3%, the R-S curves

of all samples followed along the "Constant cross-section" curve. However, in the strain range of 3%-20%, the R-S curves of all samples started to evolve significantly below the "Constant cross-section" curve. In other words, upon straining above 3%, the electro-mechanical performance of the CNT thin-films becomes better than the theoretical prediction described by the "Constant cross-section" curve. Since 3% is the elastic limit of the PET substrates used in this study, the PET substrates start to yield and deform plastically above 3% strain. Thus, the surprisingly lower increase in fractional resistance appears to be related to the plastic deformation of the PET substrates. This means that the R-S curves of all samples have followed the theoretical curve within 3% strain because the elastic deformation of the PET substrates did not modify the intrinsic electrical resistivity of the CNT network. Once the PET substrates enter the plastic deformation domain, the CNT network must be significantly modified so that it leads to an improvement in the intrinsic conductivity of the CNT films in all tested samples. The relating mechanisms causing this improvement are further discussed in 5.3.2.

5.3.2 Mechanisms of resistance change during straining

With increasing strain, different mechanisms contribute to the total resistance change of the CNT films. These mechanisms are related to the interplay of microstructural changes within the CNT network and the plastic deformation behavior of the PET substrate. A schematic of the unstrained CNT network is shown in Figure 5.13. It can be observed in the SEM image that a realistic CNT network is not composed of perfectly straight tubes but is composed of curled and entangled tubes (Fig. 5.13(a)). This prevailing feature of the CNT network is called waviness. The wavy morphology of the CNT network can be attributed to their very large aspect ratio and low bending stiffness [142].

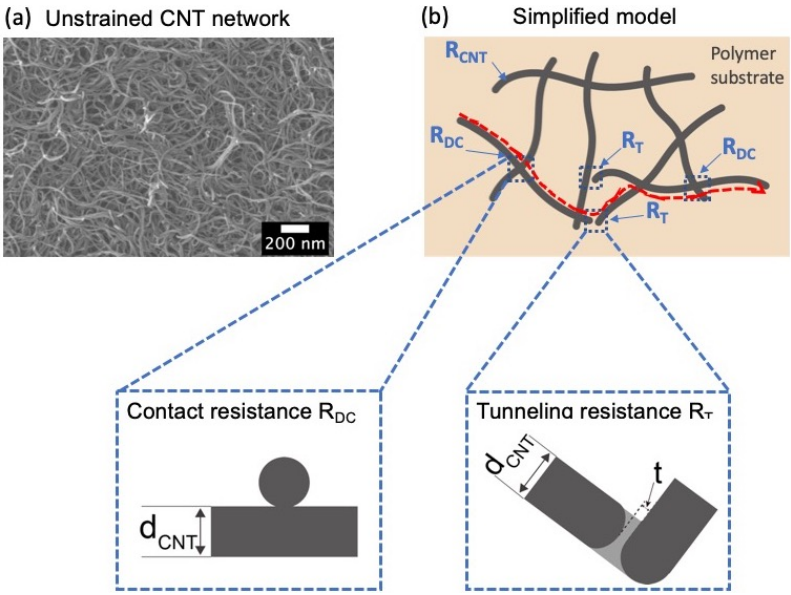

Figure 5.13: (a) SEM micrograph of a "w/o Agg_1L" sample, and (b) Schematic illustrating the resistance components in a simplified model of a CNT network, based on the contact resistance and the tunneling resistance between individual CNTs.

Three types of resistance contribute together to the total resistance R_{tot} of a wavy CNT network. The first is the intrinsic resistance of individual CNTs, R_{CNT}. The second is the intertube (or tube-tube) resistance $R_{intertube}$ (Fig. 5.13(b)). The intertube resistance of CNTs $R_{intertube}$ can be divided into two types: the direct contact resistance R_{DC} (resistance between tubes that are physically in contact) and the tunneling resistance R_T (resistance between tubes that are separated by a small gap) [143, 144].

It has been reported that the resistance value of each component differs significantly. A single CNT can act as good conductors due to the one-dimensional structure, in which the ballistic transport of electrons occurs. MWCNTs have been reported to have a R_{CNT} of 0.2-0.4 $k\Omega/\mu m$ [145, 146]. Despite the intrinsically high conductivity of CNTs, the electrical conduc-

tion of a wavy CNT network is not correspondingly efficient. This is because $R_{intertube}$ is much higher than R_{CNT}. For R_{DC}, the CNTs are physically in contact, which allows the electrical conduction through electron diffusion. However, R_{DC} depends greatly on the contact region and can vary from in the range of 90-360 kΩ [147, 148]. When there is a gap between CNTs, electrical conduction occurs by a tunneling mechanism [149, 150]. The tunneling resistance R_T is a few orders of magnitude higher than that of R_{CNT} and R_{DC}. The reported value of R_T is usually on the order of megaohms [151].

In order to explain the relevant mechanisms, a theoretical resistance model for a wavy CNT network is proposed. Four prerequisites should be made for modeling the total resistance of a CNT network.

First, in a realistic CNT network, there are several conducting paths. Suppose the total number of conducting paths is i, the resistance of a single conducting path can be described by R_p, $p = 1, 2, ..., i$, where p denotes the number for an individual conducting path.

Second, in a single conducting path, electrons have to be transported through tubes and intertube contacts. The resistance R_p of a single conducting path in the CNT network can be modeled as a serial circuit and is represented as the sum of the intrinsic resistance of individual CNTs R_{CNT} and the intertube resistance $R_{intertube}$ between CNTs [143, 144]. Thus, the resistance of a single conducting path R_p can be decomposed as:

$$R_p = R^p_{CNT} + R^p_{intertube} \tag{5.3}$$

Third, in a realistic CNT film, as shown in Figure 5.13(a), both direct contacts and tunneling have to take part in the electrical conduction. For instance, along the conducting path indicated by the red-dashed line in Figure 5.13(b), electrons have to firstly tunnel through and then go through one direct contact to the other end. Not as in an ideal percolating network, a conducting path cannot be built up only via R_{CNT} and R_{DC} within such a

network. Electrons have to be transported not only through individual tubes and direct contacts but more often through tunneling [151]. Thus, in a wavy CNT network, the contribution of direct contacts to the total resistance is much smaller when compared to tunneling contacts [143, 144]. Based on these facts, the resistance R_p of a single conducting path "p" is described as:

$$R_p = R^p_{CNT} + R^p_{intertube} = R^p_{CNT} + R^p_{DC} + R^p_T \tag{5.4}$$

Correspondingly, the change in R_p for a single conducting path upon tensile straining can be represented as:

$$\Delta R_p = \Delta R^p_{CNT} + \Delta R^p_{intertube} = \Delta R^p_{CNT} + \Delta R^p_{DC} + \Delta R^p_T \tag{5.5}$$

Fourth, in terms of the equivalent circuit, these conducting paths are connected in a parallel circuit. Thus, the total resistance of a CNT network consists of many parallel resistors of these conducting paths, described by:

$$\frac{1}{R_{tot}} = \frac{1}{R_1} + \frac{1}{R_2} + \cdots + \frac{1}{R_i} \tag{5.6}$$

$Rtot$ can be further rewritten as:

$$R_{tot} = (\frac{1}{R_1} + \frac{1}{R_2} + \cdots + \frac{1}{R_i})^{-1} \tag{5.7}$$

Correspondingly, the change in R_{tot} upon straining is also a parallel resistor of ΔR_p for each conducting path and can be represented as:

$$\Delta R_{tot} = (\frac{1}{\Delta R_1} + \frac{1}{\Delta R_2} + \cdots + \frac{1}{\Delta R_i})^{-1} \tag{5.8}$$

As can be seen, the contributions of the intrinsic resistance R_{CNT}, the direct contact R_{DC}, and the tunneling resistance R_T to every single conducting path are all comprised in equation 5.8. It is evident that since R_T has the highest value, the tunneling resistance dominates the resistance of every single conducting path and the total resistance of the wavy CNT network [151].

These insights on the parallel circuit of conducting paths and the role of R_T were not thoroughly discussed yet in the literature. In contrast, it has been discussed in the literature that the effect of strain on the intertube resistance $R_{intertube}$ is less severe than that of the intrinsic resistance R_{CNT} [143]. However, this aspect does not apply to the CNT film samples in this study. During tensile straining of the CNT films, only the wavy CNT network as a whole is deformed, and individual CNTs are not strained at all. Therefore, the change in total resistance ΔR_{tot} of a wavy CNT network results from microstructural changes by deforming the CNT network but not by straining individual CNTs and the intertube contacts.

Now, the change in the total resistance ΔR_{tot} of a wavy CNT network is explained based on the influence of each resistance component on ΔR_p of a single conducting path.

ΔR_{CNT} is mainly affected by the wavy morphology of the CNT network and is valid only when individual CNTs are strained. In a wavy CNT network consisted of randomly curled and entangled CNTs, individual CNTs are not strained under small strains but rather deformed gradually from curled shape to less curled shape with increasing tensile strains. Thus, the contribution of ΔR_{CNT} to ΔRp and ΔR_{tot} of a wavy CNT network can be neglected [152].

It has been reported that the resistivity of a CNT film is not constant upon straining, and the change in fractional resistance due to dimensional changes is smaller than that due to the change in the resistivity [153]. When a wavy CNT network is changed by external mechanical deformation, there is a change in the resistivity of the CNT network. This change in the resistivity is associated with modification of contact arrangements and the tunneling resistance between CNTs [143]. Moreover, the change in ΔR_{DC} and ΔR_T can be caused by the microstructural change of the wavy CNT network and the deformation induced by the PET substrate. For a total strain below 3%, the PET substrate is only elastically deformed, and there is almost no microstructural change in the CNT network (Fig. 5.7). Above the elastic limit of PET, the substrate starts to deform plastically. Due to the low bending

stiffness of CNTs and the strain induced by the plastic deformation of the substrate, individual curled CNTs start to be de-curled gradually. In addition to de-curling, two crossing CNTs can slide at the contact region at larger tensile strains [154–156]. As a result, individual CNTs are elongated and straightened, and thus the waviness of the whole CNT network is reduced. Along with this process till the end of stretching at 50% strain, the PET substrates are elongated in the tensile direction and contracted in the transverse direction. The reduction of the waviness of the CNT network and the bi-directional plastic deformation of the PET substrate cause a variation of the intertube contact arrangements and intertube distance within the CNT film. These coevolving mechanisms result in the improvement of the intrinsic conductivity, or equivalently, the reduction of the intrinsic resistivity of the CNT film during straining.

A schematic illustrating these coevolving mechanisms is shown in Figure 5.14. The left side illustrates the initial state before stretching. After stretching and accompanying transverse contraction, the CNT network is modified in two ways, as shown on the right side. First, a few tube-tube contacts (marked by yellow-dashed circles) are shifted due to the de-curling of individual CNTs and sliding between neighboring CNTs. As shown in the cross-sectional view, the tube-tube contacts (marked by red-edged black circles) have been decreased within the cross-sectional area. Second, the intertube distance d (marked by blue double arrows) between neighboring CNTs have also been reduced within the cross-sectional area due to the transverse contraction of the CNT network.

Since the waviness of the CNT network is changed by the geometrical change during straining, the contact arrangments of the CNT network are changed. It has been reported that the electrical conductivity of films with wavy nanotubes is lower than that of films with straight nanotubes [142]. According to references [142, 157], increasing waviness tends to increase the total resistance of the CNT network. Upon straining of CNT networks, the waviness tends to be reduced. Waviness is correlated with the entan-

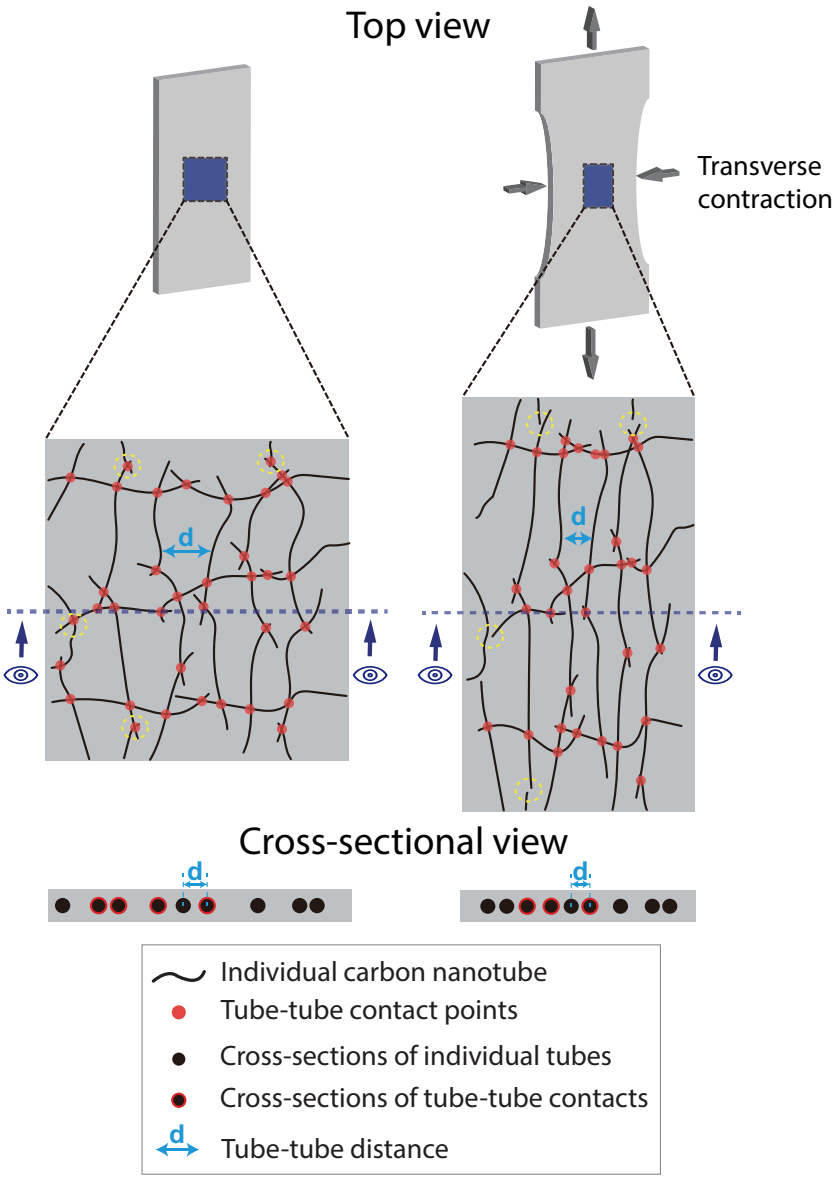

Figure 5.14: Schematic illustrating the microstructural change of a CNT network upon tensile straining. After stretching, the tube-tube contacts are shifted within the cross-sectional area, and tube-tube distance is reduced.

glement of CNTs, curling of CNTs, tube-tube distance, and the number of tube-tube contacts. Upon straining, the waviness in both the tensile and transverse direction is reduced. In this procedure, the tube-tube contacts can be shifted along the tensile direction. For a slice of the cross-section of the CNT network, the tube-tube contacts appear to be reduced, as shown in Figure 5.14. However, the total number of tube-tube contacts within the whole cross-section of the CNT film could be constant. This has two implications: (1) R_{DC} along a single conducting path does not change a lot; (2) The contribution of ΔR_{DC} to ΔR_p of a single conducting path and ΔR_{tot} of a wavy CNT network is small.

ΔR_T is significantly influenced by the plastic deformation of the PET substrate. The wavy CNT network is sensitive to compressive strain. It has been reported that compression can reduce the network resistance [158]. In this study, it has been previously shown that the CNT film samples experience a transverse contraction due to the necking of the PET substrate upon large tensile strains (Fig. 5.8). The geometrical change of the substrate is transferred into the CNT network and forces neighboring CNTs to approach each other. This leads directly to the reduction in the tunneling resistance of the CNT network. The tunneling resistance R_T is a function of the distance between neighboring CNTs, and can be estimated by [144, 151, 159]:

$$R_T = \frac{V}{AJ} = \frac{h^2 d}{Ae^2\sqrt{2m\lambda}} \exp\left(\frac{4\pi d}{h}\sqrt{2m\lambda}\right) \tag{5.9}$$

where J is the tunneling current density, V is the electrical potential difference, e is the single-electron charge, m is the mass of an electron, h is the Planck's constant, d is the mean distance between CNTs, λ is the height of energy barrier, and A is the cross-sectional area of the tunnel, which is assumed to be the same as the cross-sectional area of a single CNT. It has been reported that the change in tunneling distance d between CNTs results in an exponential change in ΔR_t. Thus, when the tunneling distance d is reduced, ΔR_T decreases exponentially. According to equation 5.5, when ΔR_T

is significantly reduced upon straining, ΔR_p of a single conducting path is also reduced. ΔR_T dominates the electrical conduction of the wavy CNT network [151], the reduced ΔR_T facilitates better electrical conduction, and the intrinsic resistivity of the CNT network is thereby decreased. Since there are many parallel conducting paths in a wavy CNT network, according to equation 5.5 and 5.8, the reduction in ΔR_p for every single conducting path leads to a reduced ΔR_{tot}. Therefore, the fractional resistance of the tested samples shows a much lower increase than the theoretical "Constant cross-section" curve, which is based on the assumption of a constant volume and a constant intrinsic resistivity during straining (see Fig. 5.12).

5.3.3 Crack bridging and pull-out of CNTs

For the "w/ Agg_3L" sample, it has been shown that there was an abrupt and stronger increase in fractional resistance above 19% strain. The sudden increase in fractional resistance for the "w/ Agg_3L" sample can be attributed to crack formation in the CNT network, which can be further correlated with the results of the *in-situ* micro-tensile testing inside the SEM (Fig. 5.7). In contrast, the "w/o Agg_3L" sample showed only a slight increase in fractional resistance above the "Constant cross-section" curve at around 40% strain. Thus, the difference in fractional resistance between these two samples can be traced back to the significant difference in surface morphology, as shown in Figure 5.15.

The micro-tensile tests on the more homogeneous "w/o Agg_3L" sample have shown almost no crack formation after being stretched to 50% strain, whereas several major cracks formed in the inhomogeneous "w/ Agg_3L" sample. In Figure 5.15(a), a major crack can be observed, whose length is longer than 20 µm. Near this major crack, several minor cracks are also found. This SEM image is representative as there are more such cracks found within the "w/ Agg_3L" sample. The tilted view of the same major crack is shown in Figure 5.15(b). It can be seen that both edges of this

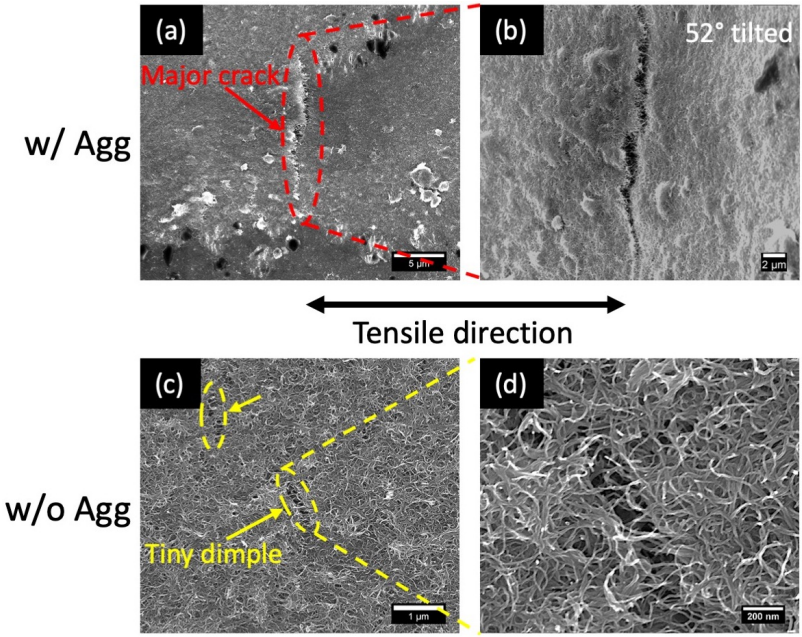

Figure 5.15: Comparison between the crack morphology of (a, b) the "w/ Agg_3L" sample and (c, d) the "w/o Agg_3L" sample after straining to 50%, the tensile direction is indicated by the black arrow.

crack are not on the same height, and there is no bridging of CNTs across the crack. The morphology of the "w/o Agg_3L" sample shows a different scenario. In Figure 5.15(c), not a single major crack can be found except a few tiny dimples (marked by yellow arrows). At higher magnification (Fig. 5.15(d)), it can be seen that the tiny dimples are caused by local necking on the surface of the CNT network. It can be observed that many CNTs still bridge across the tiny dimple.

From this comparison, it can be confirmed that the abrupt and stronger increase in fractional resistance of the "w/ Agg_3L" sample above 19% strain (Fig. 5.4) was caused by the formation of the large cracks, whose length is longer than 20 µm. Without bridging by individual CNTs, those large

cracks can deteriorate the conducting path in the CNT network. As a result, the total resistance of the whole sample has increased significantly. In contrast, for the "w/o Agg_3L" sample with improved homogeneity, no significant cracks formed even at larger strains. Due to the bridging effect of CNTs across the local necks, the conducting path in the CNT network is only slightly modified, and the resistance of the "w/o Agg_3L" sample increased almost along the theoretical curve for samples without damage.
The ability of CNTs to bridge across a crack is limited by the average length of the CNTs. Once the crack opening is larger than the average length of the CNTs, individual CNTs will be pulled out at one side of the crack opening, or individual CNTs will be fractured once they are strained up to their fracture strain of less than 3% [160]. Among the tested samples in this study, two phenomenological results were found. The SEM micrographs in Figure 5.16 show the detailed structure of CNT bundles inside two cracks in a "w/ Agg_3L" sample, which was stretched far beyond 50% strain until the PET substrate fractured completely. Inside the crack on the left, since the crack opening is smaller than the average length of CNTs (1.5 µm), almost all CNTs can fully bridge across the crack opening (marked by yellow arrows). Whereas inside the crack on the right, some CNTs can bridge across the crack (marked by yellow arrows) due to either longer tube length or narrower crack opening, but a few CNTs can not bridge the crack anymore and are pulled out of the crack front (marked by red arrows). These indicated that the bridging effect always occurs at the onset of crack formation. However, partial bridging and partial pull-out of CNTs can co-exist at different crack locations during crack formation. With further increasing crack opening, more CNTs will be pulled out, leading to unbridged cracks eventually.
The difference in the electro-mechanical behavior between the "w/ Agg" and "w/o Agg" samples is mainly ascribed to different homogeneity and surface morphology. In the "w/ Agg_3L" sample, due to the large CNT agglomerates and inhomogeneous film thickness, stress concentrations arise locally within and around the CNT agglomerates. With increasing strains,

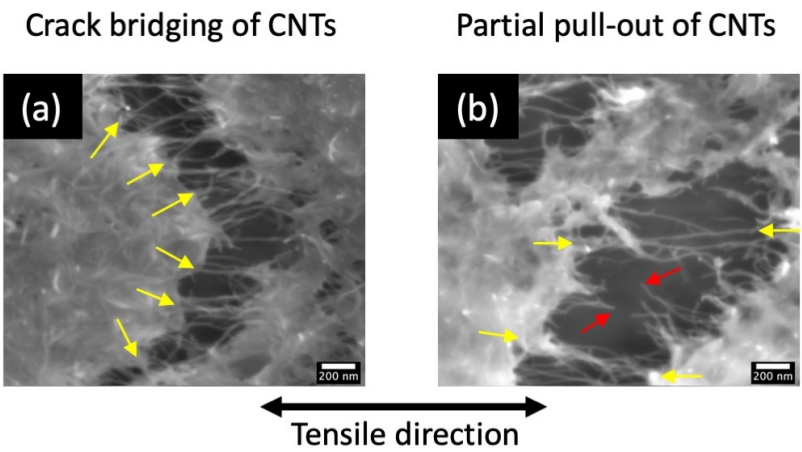

Figure 5.16: SEM micrographs showing different mechanisms: (a) A crack fully bridged by straightened CNTs (marked by yellow arrows); (b) Partial bridging (marked by yellow arrows) and partial pull-out (marked by red arrows) of CNTs.

cracks form in order to release the highly-localized stress. In the local region within the cracks, the CNTs start to be deformed from curled shape to elongated shape. At the onset of crack formation, the crack size is small, and the CNTs can bridge cross the cracks without being strained along their axis. Along with the growth of the cracks, the crack size expands further and can approach the average length of the CNTs. As a result, the CNTs, which readily bridge across the cracks, are strained in their axial direction. Only till this moment, the CNTs are strained into straight shapes. When the local strain in the crack further increases and the crack opening becomes larger than the average length of the CNTs, the CNTs cannot bridge the cracks anymore. Once CNTs are straightened and strained in their axial direction, two failure modes of CNTs can occur, which are fracture (or tensile failure) of the CNTs or the pull-out of the CNTs [161]. However, the interface between CNTs is weaker compared to the high fracture strength of individual CNTs, so the tensile failure of the CNTs is unlikely, and the pull-out effect occurs predominantly [161]. Pull-out of CNTs is also the dominant failure

mode of CNTs observed in the "w/ Agg_3L" sample. The pull-out process of CNTs continues as the cracks further expand until all CNTs inside the large cracks are pulled away from each other. Finally, many large cracks without any bridging of CNTs form in the CNT film, causing a significant increase in fractional resistance of the "w/ Agg_3L" sample. Different from the "w/ Agg_3L" sample, the "w/o Agg_3L" sample is much more homogeneous. Thus, at large strains (>20%), stresses are not localized but evenly distributed in the CNT network. Until stretching to 50% strain, no significant cracks but only a few tiny dimples form due to local necking in the CNT network. Since there is no highly-localized strain, the CNTs are not strained at all and are still in contact with each other inside the tiny dimples. Therefore, it can be concluded that the electro-mechanical behavior of CNT films on PET substrates can be significantly enhanced by improving their homogeneity, which reduces stress concentration. Although strain hardening of PET substrate occurs during stretching (Fig. 5.2), no strain localization in the PET substrate has been found (Fig. 5.3). Thus, no matter in the "w/ Agg_3L" or "w/o Agg_3L" sample, cracks or local necking formed only in the CNT network itself but not resulted from strain transfer of the PET substrate.

5.3.4 Resistance-strain hysteresis

The results from micro-tensile tests involving loading and unloading cycles (Fig. 5.9 and Fig. 5.10) have shown that the electrical resistance of a CNT network increases with increasing strain but does not fully recover during unloading and remains constant during unloading from higher tensile strains. This electro-mechanical behavior of the CNT network is termed as resistance-strain hysteresis and has also been reported recently [22, 162–166]. The change in fractional resistance with strain indicates that the microstructure of the CNT network must have been altered during strain-

ing. However, the microstructural explanation for this strain dependence of electrical resistance is not yet fully understood [156, 167–171].
Similar hysteretic behavior is also found in the "w/o Agg_1L" sample, which was loaded and unloaded cyclically from 0% to 3% strain and from 0% to 5% strain. It has been found that the resistance-strain hysteresis behavior of the CNT films in this study is related to the mechanical property of the PET substrate. PET substrates are not purely elastic but rather viscoelastic, and they exhibit hysteresis in the stress-strain curve during cyclic loading. Even when a conductive thin-film is coated on the PET substrate, the hysteretic stress-strain curve of a thin-film/PET system shows almost no difference from that of a bare PET substrate [172]. In other words, the hysteretic behavior of the PET substrate can affect the resistance evolution of conductive thin-films, including the CNT films in this study.
During the initial unloading, though the fractional resistance did not fully return to the initial value, it decreased only to a slightly higher value than the initial value. This shows that there is still a large portion of recovery in fractional resistance within the strain range of 0%-3% and 0%-5%. However, during subsequent loading-unloading cycles, the fractional resistance increased stepwise. The irreversibility in fractional resistance indicates the microstructure of the CNT network must be readily altered during loading-unloading cycles. Though 3% is within the elastic limit of the PET substrate, small shares of plastic deformation can be triggered upon initial unloading and accumulated during subsequent cyclic straining due to the viscoelasticity. Thus, the PET substrates can not be immediately fully restored to the original state upon the initial unloading. As a result, the microstructure of the CNT network is also not restored to the initial state and readily modified. Upon further loading and unloading cycles, the shape of the PET substrate keeps on being changed, and the electrical resistance of the CNT film still can not be recovered. Therefore, the fractional resistance remained higher than the initial value and increased stepwise with subsequent loading and unloading cycles.

In contrast, the five samples, which were loaded to 50% tensile strain and subsequently unloaded, showed different resistance-strain behavior. During loading from 0% to 50% strain, the R-S curves for all five samples evolved below the "Constant cross-section" curve, consistent with the improvement in intrinsic resistivity discussed earlier. It has been discussed that the reduction in intrinsic electrical resistivity at larger strain was due to the plastic deformation of the PET substrate, including longitudinal elongation and transverse contraction of the CNT network. During unloading, only a small amount of recovery of about 2% strain was found. With further unloading, the resistance stayed almost constant or decreased only very slightly. The total resistance increase after complete unloading is around 38%, resulting from the irreversible plastic deformation of the substrate. In other words, during unloading, the microstructure of the CNT network cannot be recovered to the initial microstructure before loading. Therefore, the total resistance R_{tot} of the CNT network during unloading is always higher than the initial resistance R_0 of the CNT network: $R_{tot} > R_0$, resulting in hysteresis of the electro-mechanical behavior. However, even after unloading, the intrinsic resistivity of the CNT network has been improved during loading and is still better compared to the initial resistivity of the CNT network: $\rho_{unloaded} < \rho_0$. Moreover, the increase in fractional resistance of the CNT network is only due to the geometrical change by stretching.

5.3.5 Comparison with literature results

In order to generalize the electro-mechanical behavior of the tested samples, a schematic is shown in Figure 5.17. Three groups of representative CNT samples are chosen for illustrating the relationship between the change in fractional resistance and correlating mechanisms. A "w/o Agg" sample without any damage after straining is represented by CNT Film 1 (marked by the blue curve), whereas a "w/o Agg" sample with local necking is represented by CNT Film 2 (marked by the green curve). A "w/ Agg" sample

with crack formation after straining is represented by CNT Film 3 (marked by the dark red curve). For all three types of samples, the first mechanism- "transverse contraction of the PET substrate" occurs at the onset of the plastic deformation of the PET substrate and lasts till the end of stretching. This mechanism leads to the deviation of the R-S curves for the CNT films below the theoretical prediction. It can be seen that the R-S curves of CNT Film 1, 2, and 3 evolve below the "Constant cross-section" curve (marked by the blue dashed line) until 50%, 40%, and 19% strain, respectively. Their gauge factors within these strain ranges are smaller than 1, indicating an improvement in intrinsic conductivity during straining, which is mainly due to the reduction in tunneling resistance R_T of the CNT network by the transverse contraction. The second mechanism involves the bridging effect of CNTs, in response to the local damage formation in the CNT network. For CNT Film 2, at higher strains above 40%, only local neckings form, and the size of the local necking is small compared to the length of individual CNTs, so the CNTs can still bridge across the necking site. In the case of CNT Film 3, at a strain of around 19%, cracks form in the CNT network. However, the crack opening is not very large, and most of the individual CNTs can still bridge across the crack. The last occurring mechanism involves the pull-out of CNTs and is only active for CNT Film 3. With ongoing crack growth at higher strains, the crack opening is becoming larger than the average length of individual CNTs. The CNTs are thus pulled out at one side of the crack. This pull-out process can occur gradually until most of the CNTs are pulled out. Till this moment, the crack length can be longer than 20 µm (Fig. 5.15), and the electrical conductivity of the CNT network is significantly deteriorated.

For benchmarking the performance of the CNT films in this study, the electro-mechanical behavior of the "w/ Agg_3L" and "w/o Agg_3L" samples are compared with literature results (Fig. 5.18). It has been shown that except for the "w/ Agg_3L" sample, all CNT films in this study have exhibited a lower increase in fractional resistance than the "Constant cross-

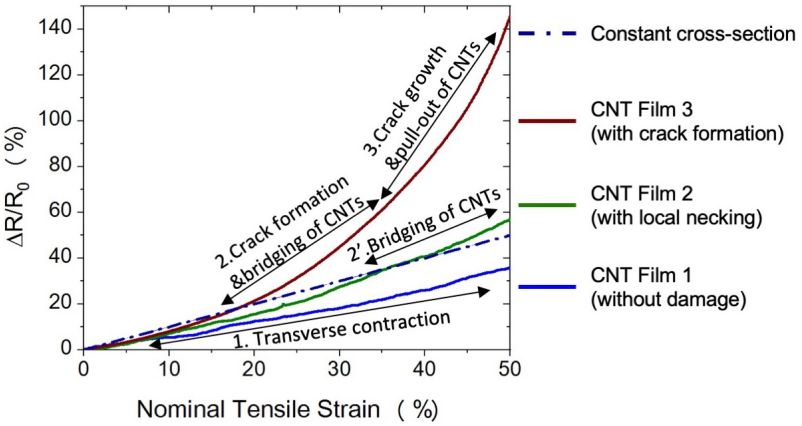

Figure 5.17: Schematic illustrating the sequence of mechanisms causing microstructural changes and damage formation within the CNT network during straining to 50%.

section" curve during stretching up to 50% strain. This implies that their conductivity is not only maintained but also improved during straining. Though the "w/ Agg_3L" and "w/o Agg_3L" samples exhibited higher increase in fractional resistance within each batch, their fractional resistance is still lower compared to the literature samples at the same strain level, such as ITO films on PET (ITO/PET) and AgNPs films on PET (AgNPs/PET) from previous work [30]. When compared to AgNPs-CNT composite films on PDMS substrate (AgNPs-CNT/PDMS) [31], the increase in fractional resistance of the "w/ Agg_3L" sample is slightly higher than that of AgNPs-CNT/PDMS, whereas the increase in fractional resistance of the "w/o Agg_3L" sample is still significantly lower than that of AgNPs-CNT/PDMS. In comparison with AgNWs films on PDMS substrate (AgNWs/PDMS) [165], the increase in fractional resistance of the "w/ Agg_3L" sample is lower than that of AgNWs/PDMS at the strain (< 30%) but higher than that of AgNWs/PDMS at the strain (> 30%), whereas the increase in fractional resistance of the "w/o Agg_3L" sample is again lower than that of AgNWs/PDMS from 0% to 50% strain. The stretchability of the

AgNW/PDMS is limited to 50% strain due to the poor stretchability of the sample [165]. In the last case, the "w/ Agg_3L" and "w/o Agg_3L" samples have been compared to MWCNTs-PDMS composite films (MWCNTs-PDMS) [36]. The MWCNTs-PDMS sample exhibited even lower GF than that of the "w/ Agg_3L" and "w/o Agg_3L" samples due to the very high loading of MWCNTs in the composites, and it is the only known sample showing a slightly better performance. Although the samples in this study showed advantages against many systems with respect to the increase in fractional resistance, it should be noted that the initial resistance R_0 of the "w/ Agg_3L" and "w/o Agg_3L" samples is 1.07 kOhms and 2.25 kOhms, respectively, which is still higher than that of the metallic counterparts, including AgNPs/PET, AgNPs-CNT/PDMS, and AgNWs/PDMS. Because the intrinsic resistivity of MWCNTs is significantly higher than that of AgNPs and AgNWs, it is reasonable that the resistance of MWCNT-based conductive films cannot be on par with that of the metallic counterparts. Nevertheless, there is still room to improve further the electrical conductivity of the CNT-based conductive films in this study.

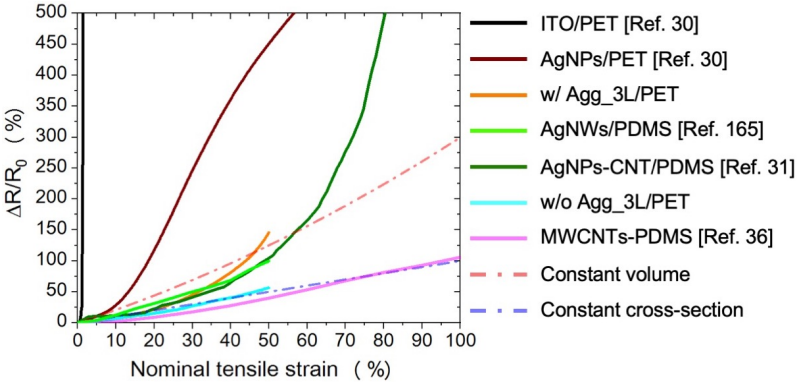

Figure 5.18: Comparisons among the electro-mechanical behavior of "w/ Agg_3L", "w/o Agg_3L", ITO/PET, AgNPs/PET, AgNPs-CNT/PDMS, AgNWs/PDMS, and MWCNTs-PDMS.

5.3.6 Concluding remarks

Based on the shown results and the above discussions, the significant findings for CNT-based conductive films are summarized in the following.

Firstly, the assumption of a constant resistivity and effective cross-section for a CNT network during elongation has been originally proposed in this work. This theory reveals that CNT-based conductive films should exhibit a linear relationship between the fractional resistance and the applied strain, which results in a gauge factor of 1. However, it is surprisingly found that the intrinsic conductivity of the CNT network even improves upon tensile straining, which results from the decreased tunneling resistance between CNTs by the tensile elongation and transverse contraction of the PET substrate. Specifically, the R-S curves of CNT-based conductive films fabricated in this study evolve below the "Constant cross-section" curve.

Secondly, the homogeneity and surface morphology of the CNT-based conductive films play important roles in their electro-mechanical reliability under tensile loading, since the "w/o Agg" samples exhibited an improved electro-mechanical behavior compared to that of the "w/ Agg" samples. The "w/ Agg" samples exhibited a higher increase in fractional resistance due to the significant crack formation within individual CNT agglomerates and subsequent crack propagation in the CNT network. In comparison, the "w/o Agg" samples exhibited a lower increase in fractional resistance, as crack formation and growth are retarded due to the more homogeneous deformation within the CNT network. Moreover, even with the existence of crack formation, CNT-based conductive films can still maintain their conductivity at higher strains because of the wavy microstructure of the CNT networks and the ability of CNTs to bridge across individual cracks.

Lastly, it is viable to fabricate flexible conductive films with MWCNTs, which combine the advantages of both economic and technological aspects. Economically, MWCNTs are much cheaper than SWCNTs, graphene, silver nanowires, and silver nanoparticles. The technological advantages of CNT-based conductive films can be viewed from two perspectives. From the electrical point of view, if the process is well controlled, multiple layers of MWCNTs can be deposited so that an excellent conductivity (< 400 Ohms/sq. or even < 100 Ohms/sq.) can be obtained. From the mechanical point of view, the influence of large tensile strain on the conductivity of the CNT films is much less significant than that on metallic films. These advantages render MWCNTs as a promising candidate for cheap and large-scale production of CNT-based conductive films.

6 Bending fatigue testing of CNT conductive films

During the application of flexible electronics, active and passive layers undergo a large number of repetitive deformations, such as stretching, bending, or rolling. Therefore, in addition to monotonic tensile testing, cyclic testing is also necessary for assessing the reliability and lifetime of CNT conductive films. For characterizing the electro-mechanical behavior of CNT conductive films under cyclic loading, cyclic bending fatigue tests on CNT conductive films have been conducted.

6.1 Bending fatigue testing

The working principle of the bending fatigue tests has been described in 3.2.2. The samples were divided into four sets, and every set was tested with a different tensile strain amplitude. The gap between the two parallel plates was set to 12.5 mm, 8.33mm, 6.25 mm, and 4.17 mm to induce tensile strain amplitudes of 1%, 1.5%, 2%, and 3%, respectively. The "w/o Agg_1L", "w/o Agg_2L", and "w/o Agg_3L" samples have been tested up to 1×10^6 (1 million) bending fatigue cycles. The relative change in resistance (or fractional resistance) $\frac{\Delta R}{R_0}$ for all three samples in every set is plotted as a function of the number of bending fatigue cycles N_{cycles}, as shown in Figure 6.1.

In the first set of tests, the samples were tested at a tensile strain amplitude of 1% (Fig. 6.1(a)). All three samples have sustained 1 million bending cycles and did not show any increase in fractional resistance. In fact, they all

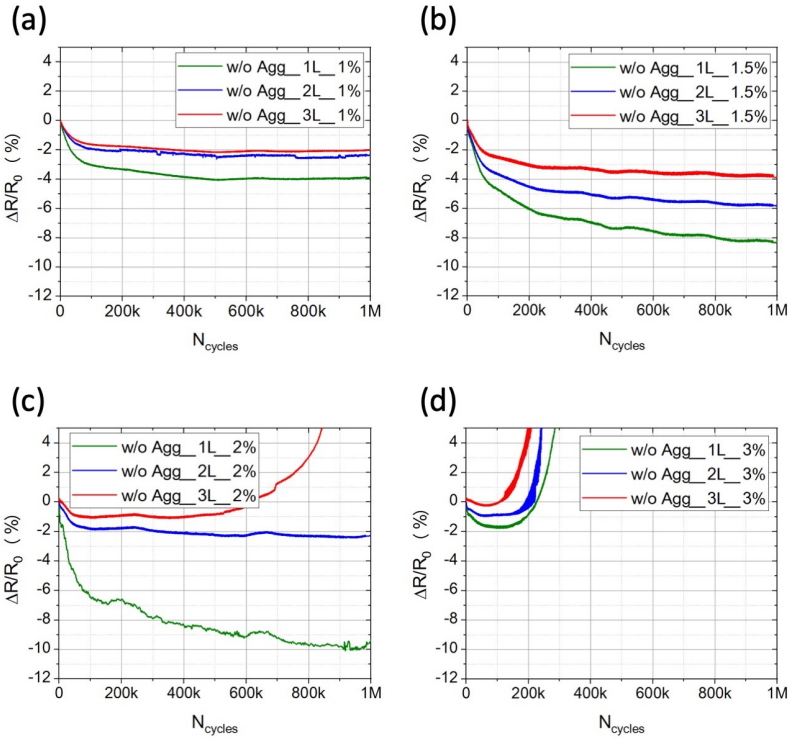

Figure 6.1: Fractional resistance evolution versus the number of bending cycles for the "w/o Agg_1L", "w/o Agg_2L", and "w/o Agg"_3L samples tested at a tensile strain amplitude of (a) 1%, (b) 1.5%, (c) 2%, and (d) 3%, respectively.

showed a continuous decrease in fractional resistance, and the degree of reduction in fractional resistance for each sample was different. For the "w/o Agg_1L" sample, a sharp decrease in fractional resistance down to -3% was observed within the first 100,000 cycles. For higher cycle numbers above 100,000, the decrease in fractional resistance of the "w/o Agg_1L" sample was only from -3% to around -4%. Similarly, a sudden decrease in fractional resistance for the "w/o Agg_2L" and "w/o Agg_3L" samples occurred within the first 100,000 cycles, but the corresponding decrease was only

around -2% and -1.6%, respectively. Up to 1 million cycles, the decrease in fractional resistance of the "w/o Agg_2L" and "w/o Agg_3L" samples was down to -2.5% and -2%, respectively.

In the second set of tests, the tensile strain amplitude has been slightly increased to 1.5% (Fig. 6.1(b)). All three samples have also sustained 1 million bending cycles and showed a continuous decrease in fractional resistance. Different to the results at 1% strain amplitude, the slope of decrease in fractional resistance is different for cycles within 0 to 400,000 cycles and within 400,000 to 1 million cycles. Up to 400,000 cycles, the fractional resistance of the "w/o Agg_1L", "w/o Agg_2L", and "w/o Agg_3L" samples was decreased significantly down to -7%, -5%, and -3.2%, respectively. Up to 1 million cycles, their corresponding fractional resistance was reduced down to -8.5%, -5.8%, and -3.8%, respectively.

In the third set of tests, the tensile strain amplitude has been increased to 2% (Fig. 6.1(c)). The "w/o Agg_1L" and "w/o Agg_2L" samples have both sustained 1 million cycles. Though at higher strain amplitude, the "w/o Agg_1L" and "w/o Agg_2L" samples showed continuous decreases in fractional resistance, and their corresponding fractional resistance up to 1 million cycles is down to -9.5% and -2.5%, respectively. However, the "w/o Agg_3L" sample failed to sustain 1 million cycles. It showed firstly a continuous decrease in fractional resistance down to roughly -1.0% and subsequently a continuous increase in fractional resistance starting from 500,000 cycles. At 600,000 cycles, its fractional resistance increased readily above 0% and kept on increasing further above 800,000 cycles. Up to roughly 900,000 cycles, an abrupt and substantial increase in fractional resistance for the "w/o Agg_3L" sample was found.

In the fourth set of tests, the samples were tested at a tensile strain amplitude of 3%. Here, a different behavior is observed (Fig. 6.1(d)). The "w/o Agg_1L" and "w/o Agg_2L" samples have both sustained only 250,000 and 280,000 cycles, respectively, whereas the "w/o Agg_3L" sample has sustained fewer than 200,000 cycles. A continuous reduction in fractional re-

sistance up to roughly 50,000 cycles was observed for all samples. The fractional resistance of the "w/o Agg_1L" sample started to increase starting from roughly 150,000 cycles, whereas the fractional resistance of the "w/o Agg_2L" sample started to increase above roughly 100,000 cycles. The increase in fractional resistance of the "w/o Agg_3L" sample started much earlier, which was around 50,000 cycles. The fractional resistance of the "w/o Agg_1L", "w/o Agg_2L", and "w/o Agg_3L" samples increased continuously and rose above 0% at roughly 220,000, 200,000, and 100,000 cycles, respectively. After these corresponding cycles, the fractional resistance for all three samples exhibited an abrupt and substantial increase.

6.2 Characterization of surface morphology

The surface morphology of all samples has been characterized by SEM after the bending fatigue tests at different strain amplitudes. Usually, when the sample is cyclically bent between two parallel plates, three types of deformation zones form along the length of the entire sample (refer to Chapter 3.2.2), including two cyclically deformed zones (Zone-B-Left and Zone-B-Right) and one statically bent zone (Zone-C). The tested sample was unfolded and placed on the sample stage for further characterization. The corresponding position of the three zones in the bent state and the flat sample state is illustrated in Figure 6.2. Since fatigue damage forms only in the two cyclically deformed zones of the 1, 2, and 3-layered CNT films, the surface morphology in Zone-B-Left and Zone-B-Right has been characterized.
Different types of damages can be found in the samples, which were bending fatigue tested at a tensile strain amplitude of 2%. The SEM micrographs of the damages, which are found in Zone-B of the "w/o Agg_1L", "w/o Agg_2L", and "w/o Agg_3L" samples, are shown in Figure 6.3. An open crack in the CNT network of the 1-layered sample can be seen (Fig. 6.3(a)). Due to the crack formation, the CNT network was torn apart, and many CNTs were left suspended on each side of the crack (marked by blue arrows

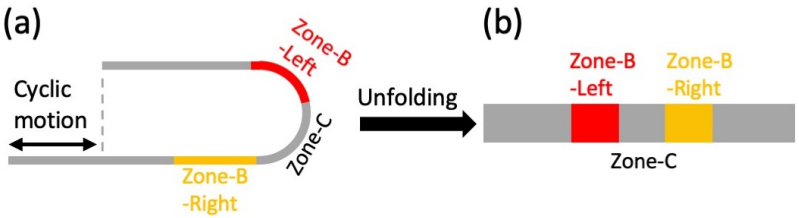

Figure 6.2: Positions of the strained regions during bending fatigue testing: Zone-B-Left, Zone-C, and Zone-B-Right on the tested sample in (a) the bent state, and (b) the flat state.

in Fig. 6.3(b)). It should be pointed out that the crack formed only locally in the CNT network. The crack did not channel through the whole CNT film and was oriented orthogonal to the tensile direction (marked by the black double arrow). In addition, at the bottom in the crack opening, the exposed surface is the plastically deformed PET substrate. In the 2-layered sample, more local cracks were found (Fig. 6.3(c)), and these cracks appeared repetitively. Interestingly, the cracks themselves formed along a direction, which is roughly 45° to the tensile direction (Fig. 6.3(d)). As a result, the CNTs next to those cracks were aligned and oriented along a particular direction (marked by red-dashed line), which is also roughly 45° to the tensile direction but perpendicular to the crack front. More local cracks were found in the 3-layered sample as well, and they occurred more destructively. Different to the crack morphology of the 1- and 2-layered samples, in which cracks formed on the surface of the CNT film, the local cracks in the 3-layered sample appeared to form deeper than the surface of the CNT film (Fig. 6.3(e)+(f)) and oriented themselves in a direction that is orthogonal to the tensile direction. Inside a representative crack (marked by the yellow dashed box), most of the CNTs were pulled-out, resulting in an unbridged crack.

The surface morphology of the "w/o Agg_1L", "w/o Agg_2L", and "w/o Agg_3L" samples after the bending fatigue test at a higher tensile strain

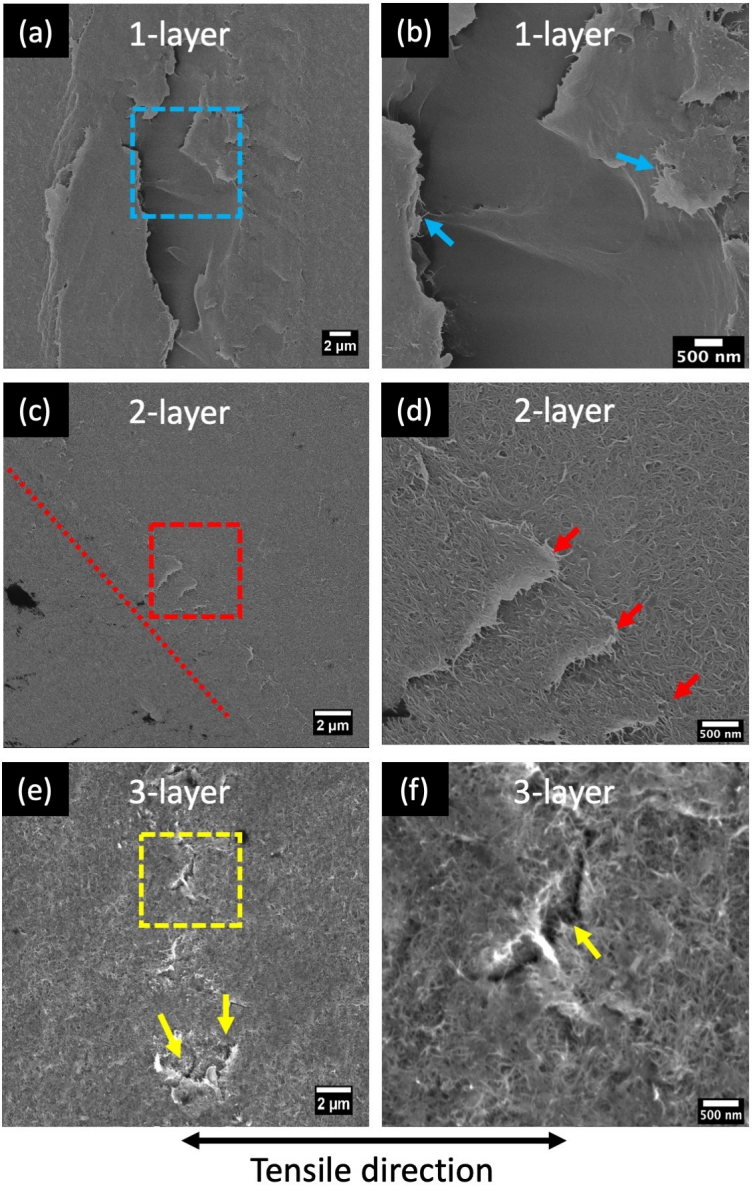

Figure 6.3: Surface morphology of Zone-B in 1-, 2- and 3-layered samples after imposing a strain amplitude of 2% for 1 million bending cycles.

amplitude of 3% is shown in Figure 6.4. Some damages in the appearance of parallel stripes were observed in every sample. These stripes spanned over a width of more than 1000 µm (1 mm) and exhibited a substructure.

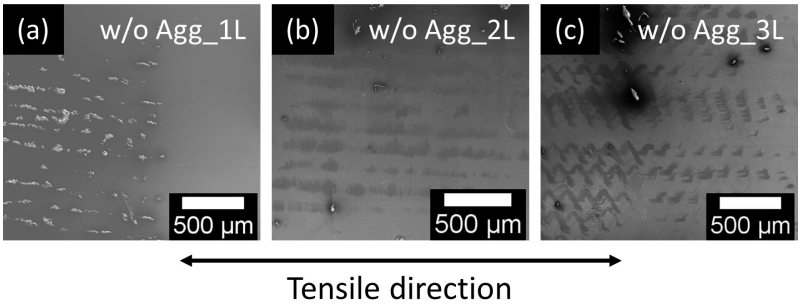

Figure 6.4: Surface morphology of Zone-B in 1-, 2- and 3-layered samples after imposing a strain amplitude of 3% for 300,000 bending cycles under lower magnification.

The substructure on the "w/o Agg_1L", "w/o Agg_2L", and "w/o Agg_3L" samples was further investigated at higher magnification and is shown in Figure 6.5. The morphology of the substructure is similar, and only the extent of the substructure is different. Under a scale of 10 µm, randomly distributed individual CNTs can be seen on the surface of the 1-layered sample (Fig. 6.5(a)). However, with higher magnification of the blue-boxed area, it can be seen that the individual CNTs protruded from the film surface (marked by blue arrows in Fig. 6.5(b)). The stripes in 2-layered samples consisted of alternating zones, which can be distinguished into dark zones and bright zones (Fig. 6.5(c)). Closer observation of the red-boxed area revealed that the bright zone consisted of disordered CNTs (left side in Fig. 6.5(d)), whereas the dark zone consisted of aligned CNTs (right side in Fig. 6.5(d)). Many CNTs were aligned along a direction marked by the red-dashed line, and a few strongly-aligned CNT bundles can be seen, as indicated by the red arrows. The most astonishing substructure appeared in the 3-layered sample. Many peak-valley-shaped stripes can be found, and they oriented parallel to each other (Fig. 6.4(c) and Fig. 6.5(e)). Higher

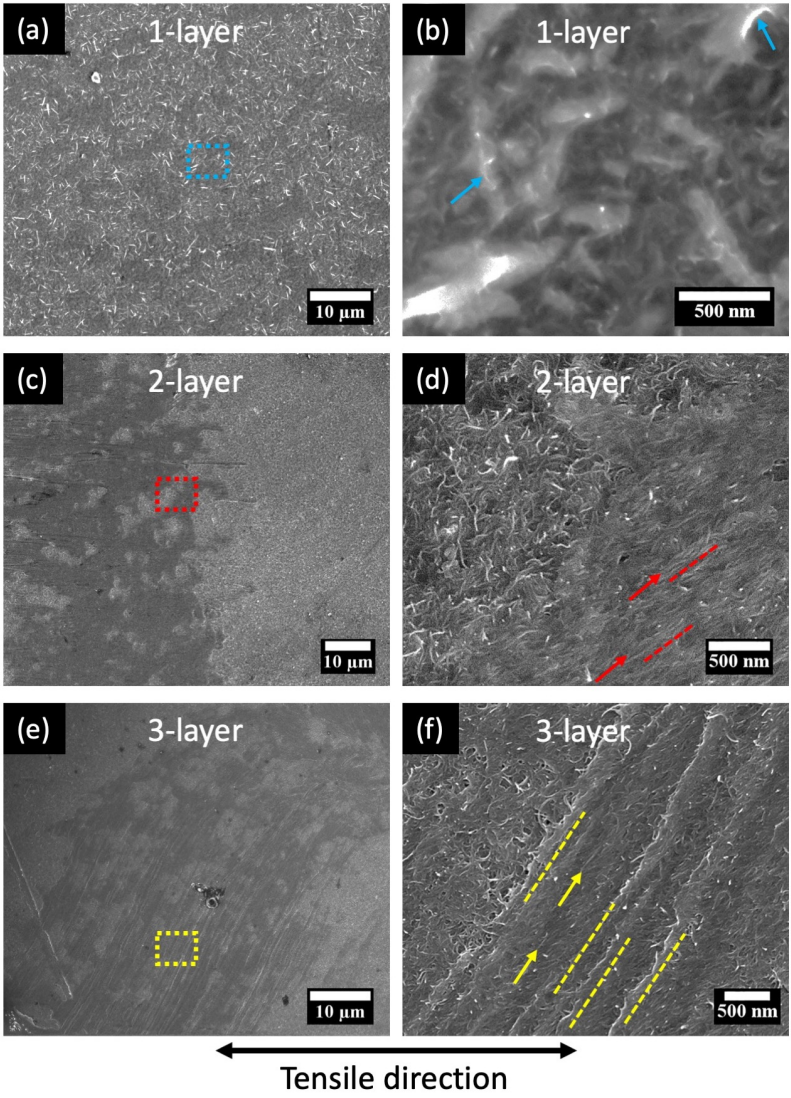

Figure 6.5: Surface morphology of Zone-B in 1-, 2- and 3-layered samples after imposing a strain amplitude of 3% for 300,000 bending cycles.

magnification of the yellow-boxed area (Fig. 6.5(e)) showed that the peak-valley-shaped stripes consisted of many locally structured CNT networks. These local CNT networks were not only aligned in a direction (marked by yellow-dashed lines in Fig. 6.5(f)), which is about 45° to the tensile direction, but also organized next to each other. In other words, many CNT bundles in the CNT network were deformed and thus aligned together in the same manner, forming edges side by side in the same direction. This way of local alignment of the CNT network is defined as "collective alignment of CNTs".

In order to investigate the influence of the bending fatigue on the CNT film at an earlier stage (lower cycles), the surface morphology of a "w/o Agg_1L" sample has been characterized, which was tested at a tensile strain amplitude of 1% for only 100,000 cycles. Two characteristic morphologies were found after bending fatigue testing.

The surface morphology with a representative local rupture, which is orthogonal to the tensile direction, is shown in Figure 6.6. It can be observed that the rupture has ripped the local CNT network apart (Fig. 6.6(a)). With higher magnification of the red-boxed area, it can be seen that the CNT network was separated into different islands, leaving gaps in between. A few CNTs were pulled out and remained on the border of the islands (marked by red arrows in Fig. 6.6(b)). Besides, it should be mentioned that the shown rupture did not channel through the sample and only disrupted the local CNT network.

The surface morphology of many individually aligned CNTs is shown in Figure 6.7(a). Such sites can always be found next to the local rupture, as shown in Figure 6.6. Closer observation revealed that (Fig. 6.7(b)), in contrast to the collective alignment of CNTs in 45° to the tensile direction, the individual CNTs were aligned orthogonal to the tensile direction. A few representative CNTs are indicated by the red arrows.

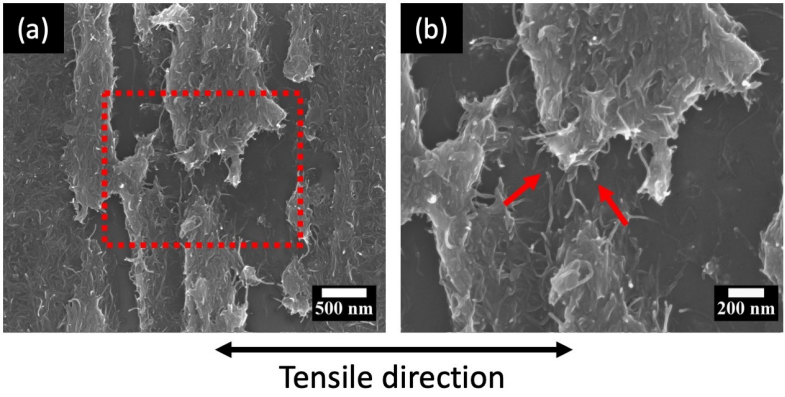

Figure 6.6: Local rupture in the CNT network of a "w/o Agg_1L" sample after imposing a strain amplitude of 1% for 100,000 bending cycles.

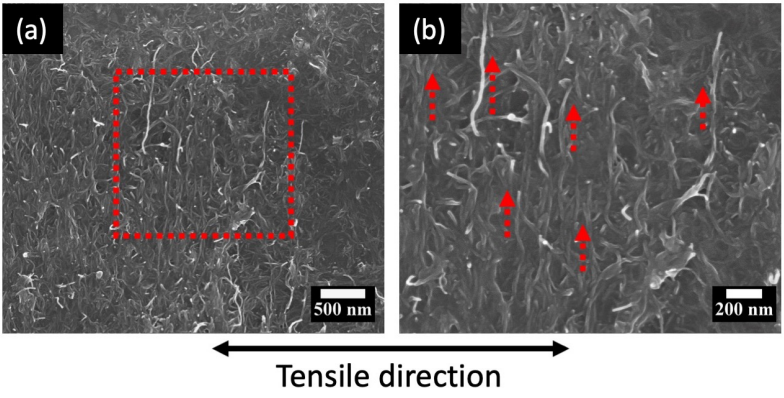

Figure 6.7: Local alignments of individual CNTs of a "w/o Agg_1L" sample after imposing a strain amplitude of 1% for 100,000 bending cycles.

6.3 Mechanical behavior of PET substrates during bending fatigue

Bending fatigue tests on bare PET substrates (DuPont Melinex® ST504, thickness: 125 µm) were conducted with three different strain amplitudes of 1%, 2%, and 3%, respectively. The bare PET substrates tested at strain amplitudes of 1% and 2% have sustained 1 million cycles without failure, whereas the bare PET substrates tested at a strain amplitude of 3% did not sustain to the end but failed at around 430,000 cycles.

A photograph of the bare PET substrates, which were imposed with the highest strain amplitude of 3%, is shown in Figure 6.8. It can be seen that three tested PET substrates ruptured in Zone-B (marked by red circles in Fig. 6.8(a)). The rupture location of a PET substrate was investigated under the optical microscope. Apparent shear band formation (marked by red arrows in Fig. 6.8(b)) can be observed near the rupture site, which manifested that the PET substrate has been severely fatigued before fracture.

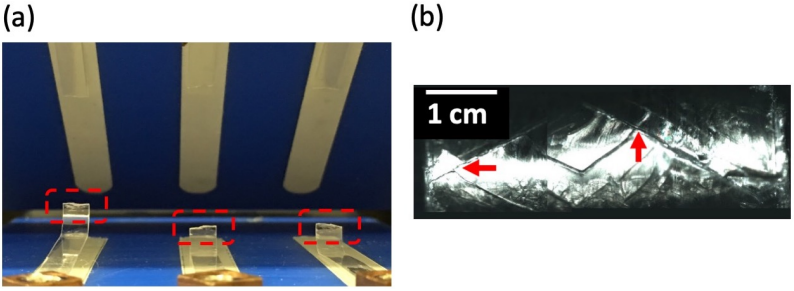

Figure 6.8: (a) Photograph of bare PET substrates after imposing a strain amplitude of 3% for 430,000 bending cycles, all three substrates showed a complete rupture in Zone-B (marked by red circles); (b) Optical micrograph showing the shear band formation (marked by red arrows) near the rupture site of the bare PET substrate.

To find out the reasons why PET substrates failed at a strain amplitude of 3%, two sets of bare PET substrates were tested at the strain amplitude of 3% for 100,000 and 400,000 bending cycles, respectively. For both sets of the

tested PET substrates, the same area in Zone-B (Fig. 3.7) was chosen, and the corresponding surface morphology was investigated in detail by HIM. The surface morphology of the bare PET substrate tested at the strain amplitude of 3% for 100,000 bending cycles is shown in Figure 6.9. Many wavy-like wrinkles can be observed, and they appeared repetitively in the orthogonal direction (Fig. 6.9(a)). Closer observation of the blue-boxed area revealed that the wrinkles formed as a result of the shear band formation of the polymer. Inside a representative wrinkle (Fig. 6.9(b)), the left and right part (marked by the dark blue and light blue ellipse) were oriented roughly 45° (marked by dashed lines) to the tensile direction but perpendicular to each other at the intersection (pointed by the white arrow).

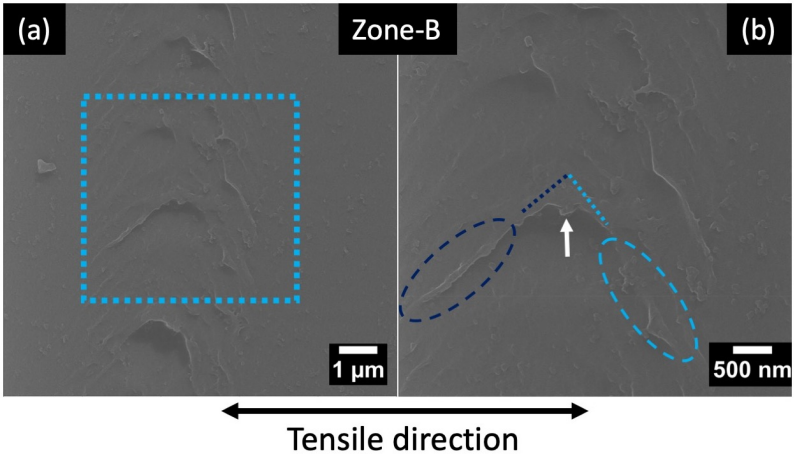

Figure 6.9: HIM micrographs of the PET surface after imposing a strain amplitude of 3% for 100,000 bending cycles: (a) wrinkles observed in Zone-B, (b) enlarged view of the blue-boxed area in (a), formation of wrinkles due to shear band formation of the PET substrate, the left and right part of the wrinkle were in roughly 45° to the tensile direction.

When the bare PET substrate was tested at the strain amplitude of 3% for 400,000 bending cycles, its surface morphology showed readily more severe damage in Zone-B. The surface morphology of Zone-B-Left of the tested

PET substrate is shown in Figure 6.10(a). A crack with a length of roughly 900 μm can be seen, and it is oriented roughly 45° to the tensile direction. A crack with such a lengthscale is classified as a major crack. Three shorter cracks with a length of around 110 μm can also be observed, and they were oriented almost perpendicular to the major crack. Due to the much shorter length, these cracks are classified as minor cracks. Higher magnification of the red-boxed area revealed that the polymer material was extruded near the intersection between the major crack and the minor crack, as shown in Figure 6.10(b). In addition, the minor crack lies underneath the major crack. The surface morphology of Zone-B-Right of the tested PET substrate is shown in Figure 6.10(c). Similar to the surface morphology of Zone-B-Left, a major crack and a minor crack can also be observed. The major crack has a length of about 900 μm and is oriented 45° to the tensile direction, whereas the minor crack has a length of around 110 μm and is almost perpendicular to the major crack. Likewise, significant extrusions of polymer material occurred at the intersection between the major and minor crack (Fig. 6.10(d)). The minor crack again lies underneath the major crack. In both Zones-B, the extrusion of polymer material and the intersection of major and minor cracks can be ascribed to the shear band deformation of the PET substrate.

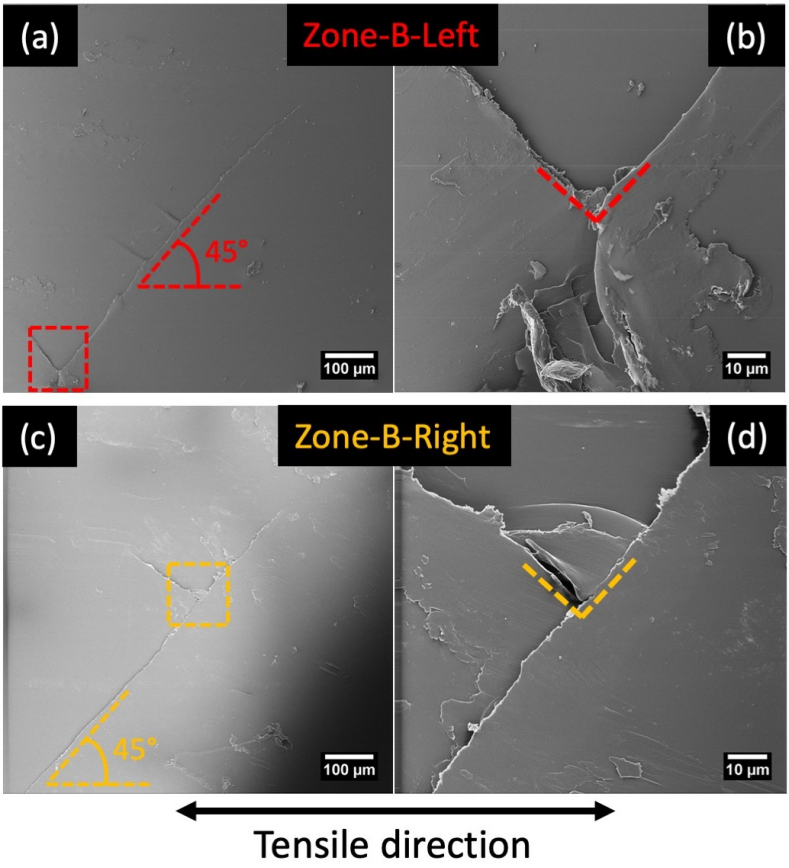

Figure 6.10: HIM micrographs of the PET surface after imposing a strain amplitude of 3% for 400,000 bending cycles: (a) formation of major and minor cracks in Zone-B-Left, (b) 10x magnification of the red-boxed area in (a); (c) formation of major and minor cracks in Zone-B-Right, (d) 10x magnification of the orange-boxed area in (c). Extrusions of polymers at the intersection between a major crack and a minor crack can be found.

6.4 Discussion

The electro-mechanical behavior of the 1-, 2-, and 3-layered CNT films is related to microstructural changes in the CNT network. These microstructural changes result from the strain transfer from the substrate, which is governed by the fatigue behavior of PET. Four distinct mechanisms are involved during bending fatigue testing: (1) cohesion among CNTs, (2) local alignment of the CNT network due to strain localization in the substrate, (3) local crack formation in the CNT network and the substrate, and (4) rupture of the PET substrate. The occurring sequence and the contribution of each mechanism depend on the applied strain amplitude, the number of bending cycles, and the number of the CNT layers.

6.4.1 Cohesion among CNTs

The continuous reduction in fractional resistance within the first 100,000 and subsequent bending cycles can be ascribed to the mechanical joining effect in the CNT network. Different mechanical joining effects exist at the nanoscale on the interface of materials, such as cold-welding and cohesion effect.

Cold welding is a mechanical joining effect occurring in materials at the nanoscale, which has been recently and experimentally found in Au nanomesh and AgNWs [173]. For example, Au nanomesh exhibited a significant decrease in fractional resistance up to -10% after 10,000 stretching cycles at a strain amplitudes of 50% [16], which was explained based on the deformation-induced cold welding within the mesh [174]. During cyclic bending, thin films consisting of metallic nanomaterials can also exhibit a decrease in fractional resistance. For thin-films consisting of AgNWs on PI substrates (AgNWs/PI), after cyclic bending with up to 2,000 cycles at tensile amplitudes of 1% and 2%, a continuous decrease in fractional resistance up to -0.3% and -0.8% was found [117]. Likewise, it has been shown that

mechanical welding, which is actually the cold welding effect, is responsible for the decrease in fractional resistance of the AgNW networks [117].
For thin-films consisting of SWCNTs on elastomeric PDMS substrate (SWCNTs/PDMS), the fractional resistance of the SWCNT film showed a significant decrease by 22% after 1,500 cycles of stretching and releasing [22]. The pronounced decrease in fractional resistance of the reported SWCNTs/PDMS sample was attributed to a period in which the nanotube bundles adopted their optimum morphology. This optimized morphology probably resulted in more efficient conducting paths through the CNT network by subsequent stretching cycles. However, it remains still unclear if the mechanism for the continuous reduction in fractional resistance of the CNT films in this study (Fig. 6.1) is similar to that for AgNWs/PI [117] and/or SWCNTs/PDMS [22].
A mechanism is proposed for explaining the reduction in fractional resistance of the CNT films tested in this work. CNTs, like AgNWs, are one-dimensional nanomaterials. Due to this characteristic feature, the CNT network is constituted via numerous mechanical junctions between individual CNTs. As discussed previously (refer to Chapter 5.3.2), an effective electrical conducting path in the CNT network is built up not only via tube-tube direct contact but much more via tube-tube tunneling. Thus, electrons have to be transported often through tube-tube tunneling. The formation of the CNT junctions is mainly ascribed to van-der-Walls forces and friction [175]. Upon cyclic bending, the induced deformation caused repetitive friction among CNTs in the junction region. The cohesion effect among CNTs is thereby triggered during the cyclic deformation of the CNT network. Thus, the intertube contact area is increased, and the gap among CNTs is reduced. The reduced tube-tube gap further promotes the cohesion effect among CNTs. As a result, these processes together lead to a reduction in both the contact resistance R_{DC} and the tunneling resistance R_T [143, 144, 147, 148]. According to equations 5.4 and 5.7, the total resistance R_{tot} of the CNT film is therefore decreased.

6.4.2 Fatigue damage of PET substrates

The specific type of PET substrates (Melinex® ST504, thickness: 125 µm) used in this study is semi-crystalline, and the elastic domain is around 3%. Semi-crystalline polymers, e.g., biaxially oriented and annealed PET foils, can exhibit strain-hardening under monotonic loading (Fig. 5.2). However, semi-crystalline PET can exhibit strain-softening behavior under cyclic loading, also termed as "cyclic softening" [176–178]. Cyclic softening in semi-crystalline PET is strongly promoted by large strain amplitudes and increasing cycle numbers.

The plastic deformation and fracture behavior of semi-crystalline polymers is still a subject of heavy debate, but the origin of their mechanical behavior is usually ascribed to their lamellar sub-structure [179–181]. The lamellar sub-structure is microscopically constituted by parallel crystalline lamellas that are sandwiched by an amorphous phase.

The deformation and yielding process of semi-crystalline polymers can be explained by the inter- and intra-lamellar shear of the lamellae, as shown in Figure 6.11. Under small deformation, the amorphous phase is initially strained because the crystalline phase is much stiffer than the amorphous phase. Three deformation modes in the amorphous phase during the initial deformation have been postulated in the literature [179, 182, 183]. Depending on the orientation of the lamellas, they can slip, shear apart, or the lamellar stack can be rotated (Fig. 6.11(b)-(d)). The crystalline phase takes part in the straining process under large deformation. Two lamellar deformation mechanisms occur when the crystalline phase is strained. The first process is the fine chain slip through the lamellae (Fig. 6.11(e)), whereas the second process is the coarse slip of lamellae (Fig. 6.11(f)). The intra-crystalline shear results in a fragmentation of the lamellae [179]. This deformation process is plastic and irreversible.

Semi-crystalline PET can undergo considerable levels of plastic deformation at room temperature and moderate strain rates [184]. Typically, the

plastic deformation develops inhomogeneously, so only local regions in the material are plastically deformed: craze formation due to normal stress yielding and shear band formation due to shear yielding [185].

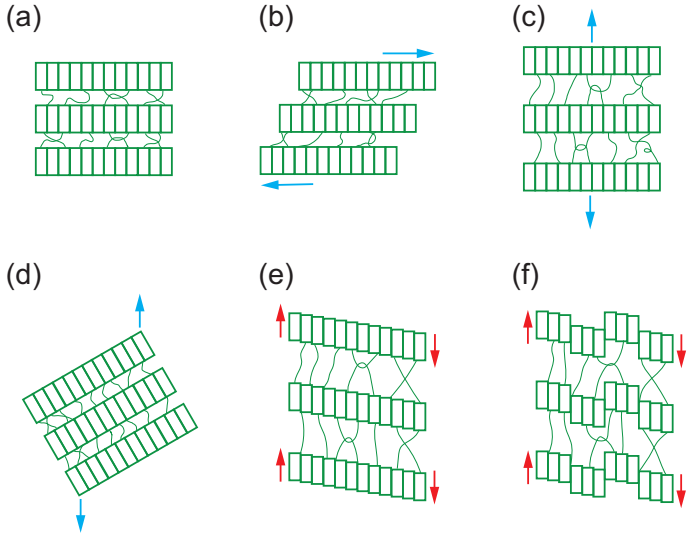

Figure 6.11: (a) Lamella before deformation; amorphous phase: (b) interlamellar slip (or shear), (c) interlamellar separation, and (d) stack rotation; crystalline phase: (e) fine chain slip, and (f) coarse slip (redrawn after References [179, 182, 183]).

For a strain amplitude $\varepsilon_a < 3\%$, since it is within the elastic limit of the PET substrates, the PET substrates are not fatigued even with increasing bending cycles. For a strain amplitude $\varepsilon_a \geq 3\%$, strain localization in the form of shear bands and subsequent crack formation within the PET substrate will occur and lead to fatigue damage. With increasing cycle numbers, the cracks propagate further until the rupture of the PET substrate. All these micromechanical processes have been observed in the experiment. Local plastic deformation can be found in the PET substrate which was imposed with 3% strain amplitude for 100,000 bending cycles (Fig. 6.9) and 400,000 bending cycles (Fig. 6.10), respectively. Additional to the localized plas-

tic deformation, the formation of large cracks in the size of about 1 mm and minor cracks in the size of around 100 µm can be found in Zone-B of the PET substrate. Typically, the PET substrate showed a total fracture at around 430,000 bending cycles. Moreover, the shown fatigue failures in the PET substrate occurred in different microstructures depending on the extent of the plastic deformation. Wrinkles and cracks are both caused by the shear band formation in the PET substrate. At an earlier stage of bending fatigue cycles, the polymer material on the surface of the PET substrate is plastically deformed to accommodate the shear band formation. This process leads to the particular microstructure of the wrinkles. Their left and right parts are oriented both in roughly 45° to the tensile direction but perpendicular to each other. Formation of major and minor cracks occurred at a later stage of bending fatigue cycles. They result from the highly-localized strain during the severe plastic deformation within the shear bands. Likewise, the major and minor cracks are both oriented in 45° to the tensile direction and perpendicular to each other. Besides, polymer materials are extruded at/near the intersection of the major and minor cracks during the severe plastic deformation.

As shown in the results, shear bands tend to form in Zone-B and is triggered by local shear yielding during plastic deformation. The formation of shear bands leads eventually to crack formation in the PET substrate (Fig. 6.10). Theoretically, shear bands represent a phenomenon of coexisting regions of a different strain rate. It is widely accepted in the literature that the most important triggering mechanism for the formation of shear bands is a relationship describing non-monotonic stress and strain rate [186]. The correlating mechanisms have been well-reviewed by K. Friedrich [184]. In summary, the PET substrates exhibit an elastoplastic behavior followed by ductile fatigue failure under cyclic bending at a higher strain amplitude, and this will also trigger strain localization in the CNT film at the fatigue damage sites of the PET substrate, leading to microstructural changes in the CNT network.

6.4.3 Local microstructural changes in the CNT network

Microstructural changes in the CNT network have been found locally in the strained region of the cyclically bent samples. Among them, local alignments of the CNT network and local cracks in the CNT network are observed. The two distinct microstructural changes are both caused by the strain localization in the PET substrate and can occur successively, as shown in Figure 6.12.

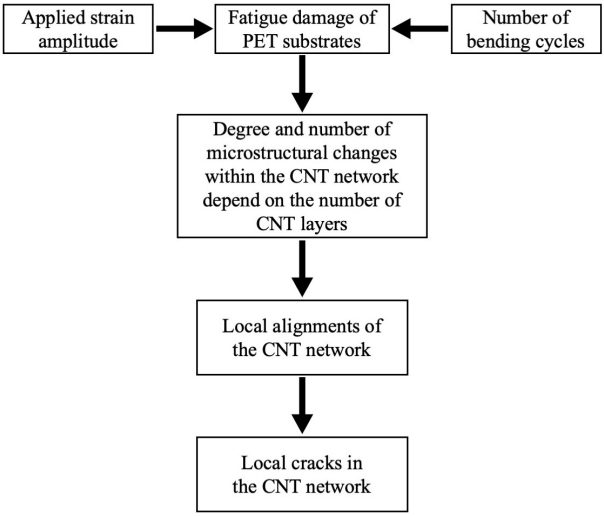

Figure 6.12: Block diagram illustrating the relationship between various factors and the local microstructure changes in the CNT network.

The local alignments of the CNT network denote the aligned microstructure of an individual CNT or many CNT bundles. It is a result of the microstructural accommodation of the CNT network in response to the localized plastic deformation of the underlying PET substrate. As already introduced (refer to Chapter 6.2), CNTs can be aligned locally in two ways: either a single CNT is aligned (individually), or a group of CNT bundles is aligned (collectively). It can be seen that the CNTs in the "w/o Agg_1L" sample (Fig.

6.7), which was tested at a strain amplitude of 1%, are individually aligned; whereas the CNTs in the "w/o Agg_2L" and "w/o Agg_3L" samples (Fig. 6.3 and 6.5), which were tested at a higher strain amplitude of 2% and 3%, are collectively aligned. This difference implied that the degree of local alignment of the CNT network is mainly affected by the number of CNT layers and the applied strain amplitude. Specifically, the difference in the alignment structure of the CNT network lies in the structural compliance of CNT films.

The structural compliance is different for CNT films with a different number of CNT layers. Due to lower film thickness and less CNT density of the 1-layered CNT film ("w/o Agg_1L"), there are fewer tube-tube contacts within the cross-section. Thus, the individual CNTs have more degree of freedom and can adapt to the induced deformation, which means the structural compliance of 1-layered CNT films is lower than that of 2-layered ("w/o Agg_2L") and 3-layered ("w/o Agg_3L") CNT films. As a result, the CNT networks in 1-layered CNT films tend to be aligned individually rather than collectively. Thicker CNT films, such as 2-layered and 3-layered CNT films, have a higher film thickness and a higher CNT density, so there are more tube-tube contacts within their cross-sections. Accordingly, they are stiffer than 1-layered CNT films; thus, the individual CNTs have fewer degrees of freedom, and the possibilities adapting to induced deformation for individual CNTs are restricted. Therefore, the CNT networks in 2-layered and 3-layered CNT films tend to be aligned collectively rather than individually. These are how the CNT networks accommodate induced deformation under a small strain amplitude.

During cyclic bending with a higher strain amplitude, e.g., $\varepsilon_a \geq 3\%$, the inhomogeneous plastic deformation in the underlying PET substrate is so severe that shear-band induced cracks can form in the PET substrate. The plastic deformation is localized within the shear bands, and the shear bands are perpendicular to each other but 45° to the tensile direction, thus forming a zigzag. This kind of zigzag-shaped and near-surface shear band has been

reported in the amorphous PET films rolled at 6% strain [187]. The morphology of the cyclic bent PET substrate (Fig. 6.10) indicates clearly that the shear band direction is in accordance with the alignment direction of CNTs in the CNT network, which is also 45° to the tensile direction. This similarity has indicated that the shear band formation in the substrate can directly modify local microstructures in the CNT network.

The local alignments of the CNT network have a scale that is larger than the length of CNTs themselves. Thus, they can affect the conducting path in the CNT network and could have a negative impact on the resistance evolution of the CNT films. This is reflected by the increase in fractional resistance after the initial decrease due to the cohesion among CNTs. The conducting path in the CNT network is mainly built up through tunneling resistance. However, the local alignments of the CNT network create many parallel CNT bundles within the cross-sectional area. This resulted in higher tunneling resistance since electrons have to tunnel through many parallel CNT bundles. Moreover, the entire width of the alignment structures has a size of 1-3 mm along the tensile direction (Fig. 6.4). Therefore, their influences on the electrical conductivity of the whole CNT film can be significant. As a result, the increased tunneling resistance R_T leads to an increase in the total resistance R_{tot} of the CNT films.

Besides local alignments of the CNT network, local cracks in the CNT network have also been observed in the cyclically bent CNT films. Local cracks in the CNT network formed when the CNTs cannot be further aligned, for accommodating the highly localized plastic deformation in the PET substrate. Whether for 1-, 2-, or 3-layered CNT films, the plastic deformation, shear band formation, and subsequent crack formation in the PET substrate are the same. However, the CNT films with different numbers of layers adapt to the plastic deformation of the underlying PET substrate differently. This difference is again related to the different structural compliance of the 1-, 2-, or 3-layered CNT films. At locations where a highly localized strain in the PET substrate is transferred into the CNT network, the adaptability of

the CNT network is lower for CNT films with more layers. Consequently, cracks may form earlier in thicker films. This process is similar to the crack bridging and subsequent pull-out effect of CNTs under large tensile strains. For the 1-layered CNT films (Fig. 6.6 and Fig. 6.3(a)), a partial rupture formed in the CNT network. Due to thinner thickness and lower density of CNTs, a higher localized strain induced by the plastic deformation in the PET substrate can force the local separation of the CNT network, forming a local and partial rupture, and no CNTs can bridge across the rupture. However, in the case of thicker films, such as 2- and 3-layered CNT films, due to higher film thickness and more CNT density, they are stiffer than thinner films. Thus, the stress in the CNT network gets higher. As a result, cracks can form in thicker films earlier than in thinner films. This is reflected from the experimental curves of the CNT films tested at 3% strain amplitude (Fig. 6.1(d)), as the increase in fractional resistance for 2- and 3-layered CNT films started earlier than that for 1-layered CNT film, indicating that the thicker CNT film is less resistant to crack formation than the thinner CNT film, and cracks formed earlier in thicker CNT films. For the 2-layered CNT film (Fig. 6.1(c)), many local cracks were found, which were oriented parallel with each other and 45° to the tensile direction. Whereas for the 3-layered CNT film (Fig. 6.3), both the film thickness and CNT density are the highest among the three samples. The even stiffer 3-layered film can take even higher loadings, and much more CNTs in the film have to be strained. Eventually, cracks inside the surface protrusion formed as a result of the highly localized strain transferred from the PET substrate. They may also form in thinner CNT films before local crack formation. However, due to the larger volume of the 3-layered CNT film, they appeared more apparently in thicker CNT films than in thinner CNT films. Irrespective of the number of CNT layers, the shapes of local cracks in the CNT network differ from the crack morphology in other conductive films, such as evaporated metallic films or metallic nanoparticulate films. No channel cracks

like the ones in evaporated Ag films [105, 113, 114] and AgNPs films [30] were observed in the CNT films.

Likewise, the local cracks in the CNT networks also have a negative impact on the resistance evolution of the CNT network. These crack formations shut down the conducting path locally and thus deteriorate the electrical conductivity of the CNT network. With the occurrence of more local cracks after more bending cycles, the conducting paths can be significantly disrupted, and this leads to a significant increase in fractional resistance. In summary, three aspects regarding the above mechanisms should be noted. Firstly, both local alignments of the CNT network and local cracks in the CNT network are results of the microstructural changes in the CNT network in response to the strain localization that is transferred from the fatigued PET substrate, and they are not due to intrinsic fatigue damage of the CNT network. Secondly, the local alignments of the CNT network occurred earlier than the local crack formation in the CNT network because the CNT network can be aligned and stretched as a whole before individual CNTs are locally strained. Lastly, the lifetime of the CNT film samples is determined by the final rupture of the PET substrate.

6.4.4 Resistance evolution during fatigue

Regarding the electro-mechanical behavior of the tested CNT films during cyclic bending, namely, the fractional resistance evolution with increasing cycle number, four major stages can be distinguished: (1) Rapid decrease in fractional resistance, (2) Gradual stagnation in fractional resistance, (3) Increase in fractional resistance, and (4) Abrupt increase in fractional resistance to infinity. Correspondingly, four distinct mechanisms are involved in the fractional resistance evolution, as shown in Figure 6.13.

Not every stage and its corresponding mechanism have been involved in the fractional resistance evolution of all CNT films, as their occurrence depends on the applied strain amplitude. For CNT films imposed with a strain

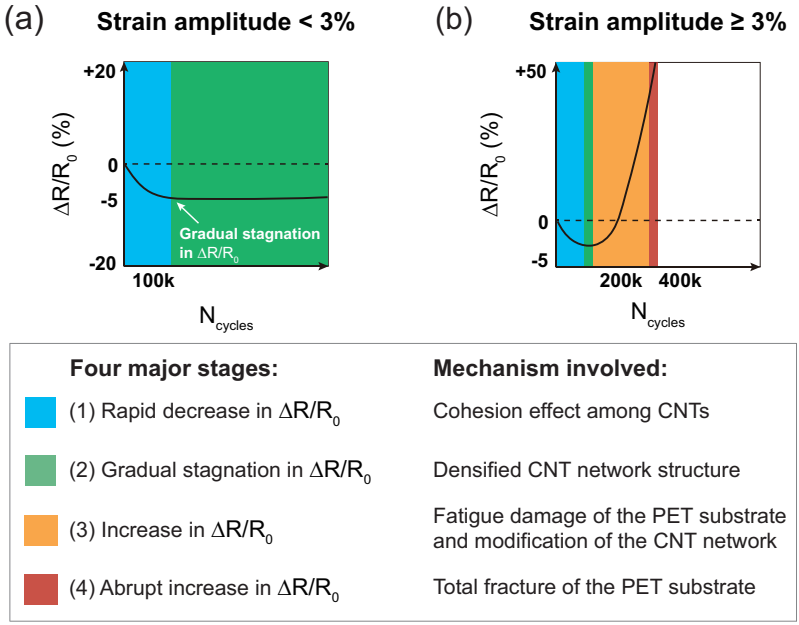

Figure 6.13: Schematic illustrating the effective mechanisms and their occurring sequences corresponding to the fractional resistance evolution stage during cyclic bending for CNT films imposed with a strain amplitude of (a) $\varepsilon_a < 3\%$, and (b) $\varepsilon_a \geq 3\%$, respectively.

amplitude of $\varepsilon_a < 3\%$, only the first and the second stage were involved (Fig. 6.13(a)). In the first stage, the rapid decrease in fractional resistance is due to the cohesion effect among CNTs. The CNT network has been densified, leading to a continuous reduction in fractional resistance. In the second stage, the decrease in fractional resistance has stagnated gradually. The gradual stagnation is because the space among the CNTs is becoming less so that the cohesion effect also slows down. Since the applied strain amplitude is within the elastic domain of the PET substrate, almost no fatigue of the PET substrate occurs with increasing bending cycles. Thus, the microstructure of the CNT network is not influenced and modified by the

PET substrate. As a result, the fractional resistance remains almost constant to the end of the bending fatigue test.

In contrast, for CNT films imposed with a strain amplitude of $\varepsilon_a \geq 3\%$, all four stages and their corresponding mechanisms were involved (Fig. 6.13(b)). In this case, the first stage is the same as the case for smaller strain amplitudes. In the second stage, the fractional resistance has also stagnated due to the densified CNT network. However, the gradual stagnation in fractional resistance did not sustain for many cycles, because the readily densified CNT network by cohesion effect is further modified in the following stage. In the third stage, the PET substrate started to form fatigue damage in the form of shear bands, and the plastic deformation accumulates locally with increasing bending cycles. As a result, local alignment of the CNT network and local crack formation in the CNT network occurs successively. They are a result of the microstructural changes of the CNT network in accommodating the strain localization and subsequent crack formation in the PET substrate. Both mechanisms contributed to the increase in fractional resistance in the third stage. In the fourth stage, cracks in the PET substrate had propagated already up to a millimeter scale, causing the rupture of the PET substrate. The total fracture of the PET substrate directly leads to an abrupt increase in fractional resistance to infinity, indicating the complete disruption of the CNTs/PET system.

So far, it can be concluded that two mechanisms, which are the intrinsic mechanism-cohesion effect among CNTs- and the extrinsic mechanism-fatigue damage formation in PET substrate- have played vital roles in the fractional resistance evolution during bending fatigue. However, the degree of both mechanisms is governed by the applied strain amplitude and the number of CNT layers. The fractional resistance as a function of the applied strain amplitude is analyzed and plotted in Figure 6.14. It can be seen that the fractional resistance evolution for all CNT films exhibits a transition (marked by the grey-dashed line) between the lower and higher strain regime. For 1-layered CNT films ("w/o Agg_1L"), the transition strain

amplitude is around 2%, whereas for 2- and 3-layered CNT films ("w/o Agg_2L" and "w/o Agg_3L"), the transition strain amplitude is found to be around 1.5%.

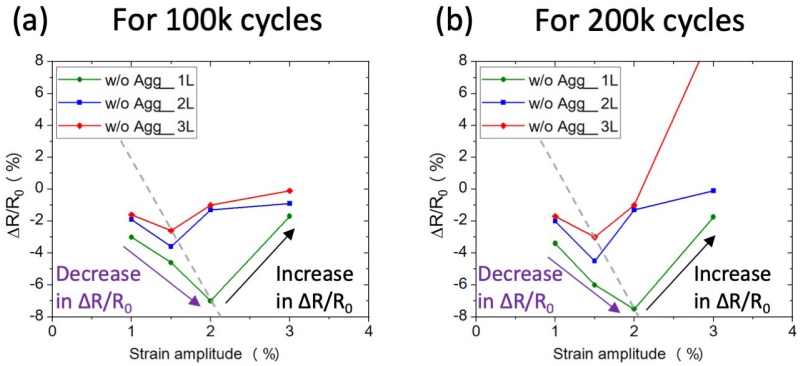

Figure 6.14: Plots of fractional resistance $\frac{\Delta R}{R_0}$ as a function of the applied strain amplitude ε_a: (a) for 100,000 bending cycles, and (b) for 200,000 bending cycles. A transition in fractional resistance evolution is discovered (marked by the grey-dashed line).

In the left part (left to the grey-dashed line), it can be seen that the fractional resistance decreases continuously with increasing strain amplitude, indicating that the cohesion effect among CNTs can be further promoted at a larger strain amplitude before approaching the transition strain amplitude. Moreover, in terms of the number of CNT layers, it can be observed that at the same strain amplitude and for a lower number of CNT layers, the decrease in fractional resistance is more significant. This implies that the cohesion effect among CNTs is stronger in thinner CNT films than in thicker CNT films, due to lower density and lower rigidity of the CNT network in thinner CNT films. In the right part (right to the grey-dashed line), it can be seen that the fractional resistance increases abruptly with increasing strain amplitude, indicating that the onset of fatigue damage formation in the PET substrate can deteriorate the CNT films. Likewise, in terms of the number of CNT layers, it can be concluded that at the same strain amplitude but for an increasing number of CNT layers, the increase in fractional resistance is

higher. This implies that the fatigue damage formation in the PET substrate is more influential on thicker CNT films than on thinner CNT films, which also explains why thicker CNT films failed earlier than thinner CNT films at larger strain amplitudes (Fig. 6.1(c)+(d)).

6.4.5 Comparison with literature results

The results of this work are compared with the previous work from T. Haas *et al.* and B. J. Kim *et al.* [30, 116], as shown in Figure 6.15. It can be seen that, although the CNT films were tested at 1.5% strain amplitude, which is higher than that for evaporated silver and silver nanoparticle (AgNPs) films, they exhibited unrivaled performance in resisting bending fatigue. The evaporated Ag film and AgNP film exhibited 100% and 58% increase in fractional resistance, and survived only up to 400,000 and 480,000 bending cycles, respectively. In comparison, due to cohesion effect among CNTs and the absence of fatigue damage in the CNT network, not only the CNT films have sustained 1 million bending cycles, but also the fractional resistance of the CNT films has been decreased.

A more convincible comparison is shown in Figure 6.16, in which 1-layered CNT films ("w/o Agg_1L") are compared with silver nanowire (AgNWs) films reported by B. Hwang [117]. Both AgNWs and CNTs films are tested on the same type of bending fatigue tester at the same strain amplitudes of 1%, 2%, and 3%, respectively. It can be seen that under small amplitudes, such as 1% and 2%, the fractional resistance of the CNT film is significantly lower than that of the AgNWs films. A quantitative comparison of the fractional resistance between AgNWs films and CNT films is given in Table 6.1. The fractional resistance of AgNWs films tested at 1% and 2% strain amplitude up to 500,000 bending cycles are 1.6% and 2.8%, respectively, whereas the fractional resistances of CNT films also tested at 1% and 2% strain amplitude up to 500,000 bending cycles are -4% and -1.1%, respectively. This indicates that at smaller strain amplitudes, not only the CNT

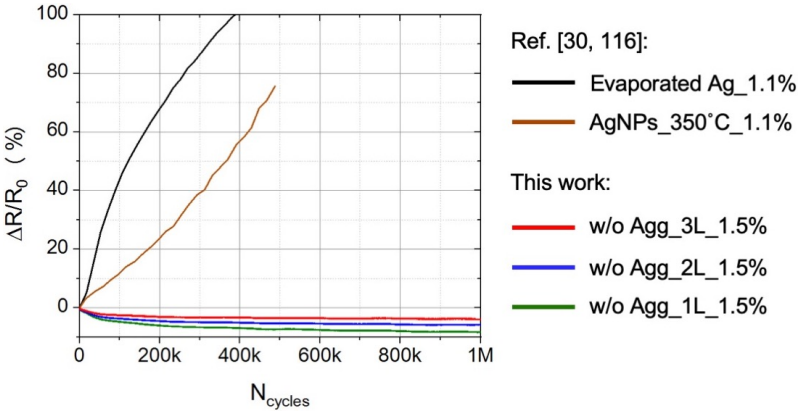

Figure 6.15: Comparison of the fractional resistance evolution during bending fatigue testing among evaporated Ag film tested at 1.1% strain amplitude, inkjet-printed and 350°C sintered AgNPs film tested at 1.1% strain amplitude, and the "w/o Agg_1L", "w/o Agg_2L" and "w/o Agg_3L" samples tested at 1.5% strain amplitude, respectively.

films are fatigue-free to 1 million bending cycles, but also their conductivities have been improved during cyclic bending. For the CNT film tested at 3% strain amplitude, its fractional resistance is still much lower than for the AgNWs film. Up to 200,000 cycles, the fractional resistance of the CNT film is around -0.6%, whereas the fractional resistance of the AgNWs film is already 7.7%. Likewise, this implies that even at higher strain amplitudes, the fractional resistance of the CNT films is beneficial compared to that of AgNWs films. The significant increase in fractional resistance of the CNT film after 200,000 cycles is only due to the crack formation and subsequent rupturing process of the PET substrate.

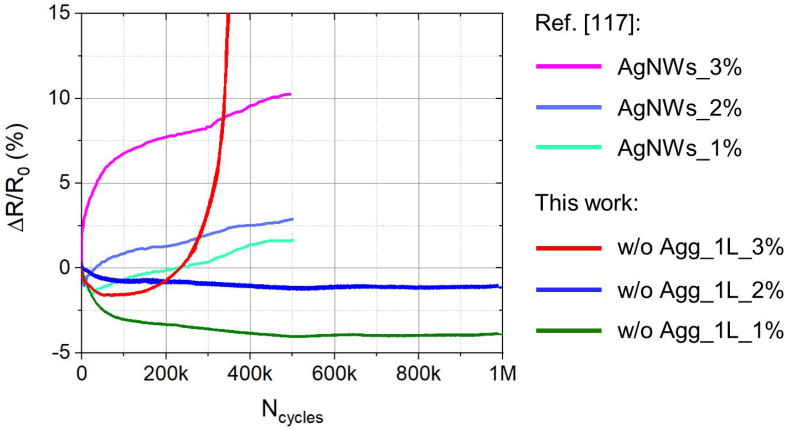

Figure 6.16: Comparison of the fractional resistance evolution during bending fatigue testing between a group of AgNWs films and a group of the "w/o Agg_1L" samples (1-layered CNT films), both groups were tested at 1%, 2%, and 3% strain amplitude, respectively.

Table 6.1: Quantitative comparison between the fractional resistance of AgNWs films and of 1-layered CNT films.

ε_a for N_f cycles	$\frac{\Delta R}{R_0}$ of AgNWs films	$\frac{\Delta R}{R_0}$ of CNT films
1% for 0.5 million cycles	1.6%	-4%
2% for 0.5 million cycles	2.8%	-1.1%
3% for 200k cycles	7.7%	-0.6%

6.4.6 Concluding remarks

Based on the shown results and the above discussions, the significant findings on the fatigue behavior of CNT-based conductive films are summarized in the following.

Firstly, the most astonishing finding in this study is that CNT-based conductive films are free of fatigue. CNT-based conductive films on the 125-µm

thick PET substrate are fatigue-free at 1% and 2% strain amplitudes up to 1 million bending cycles, due to the absence of fatigue damage in the PET substrate. At a higher strain amplitude of 3%, CNT-based conductive films have still sustained at least 200,000 bending cycles even with the rupture of the PET substrate. They are fatigue-free to the limited cycles only because the microstructure of the CNT network is disrupted by the plastic deformation and fatigue damage in the PET substrate.

Secondly, another important finding is the cohesion effect among CNTs, which has not yet been discussed in the literature. The continuous decrease in fractional resistance of the CNT-based conductive films can be ascribed to the cohesion effect. The cohesion effect is very pronounced at the initial 100,000 or 200,000 bending cycles, depending on the applied strain amplitude. The cohesion effect among CNTs becomes stronger at a higher strain amplitude within 3%, or for CNT films with fewer layers. At a strain amplitude higher than 3%, the cohesion effect will be exhausted by the fatigue damage of the PET substrate. In subsequent bending cycles, the cohesion effect can continuously densify the CNT network and decrease the tunneling resistance among CNTs, resulting in an improvement in the electrical conductivity of the CNT network. This is quite unusual and unique for conductive films under fatigue conditions.

Thirdly, the electro-mechanical reliability of CNT-based conductive films is superior when compared to AgNPs films and even to AgNWs films, since the CNT films can adapt to strains better than metallic nanoparticulate and nanowire films and are inherently fatigue-free. This capability of the CNT films is benefited from the entangled and curvilinear structure and low bending stiffness of the CNT network. The CNT network has significant enhancement in fatigue resistance due to the ability of the CNT network to stretch the network rather than straining individual CNTs. The CNT network can re-orient to accommodate strain before straining individ-

ual CNTs. Unless being massively modified by the strain localization in the PET substrate at higher strain amplitudes, almost no fatigue damage form in CNT films.

Fourthly, the electro-mechanical reliability of CNT-based conductive films is only limited by the PET substrate, and their lifetime is determined by the fatigue and subsequent rupture of the PET substrate. At higher strain amplitudes, crack formation and propagation in the PET substrate could disrupt the CNT network and lead to total failure of the whole system. If CNT films were fabricated on a polymer substrate, which will not fatigue and rupture at a higher strain amplitude than 3%, they could sustain even higher strain amplitudes and much more than 1 million bending cycles.

Finally, it has been shown that the industry-standard substrates for printed electronics-PET foils are not ideal for flexible electronic devices demanding high reliability at higher strain amplitudes. Alternative flexible substrates are required. However, it is still very challenging to choose a flexible substrate that meets all the critical requirements, including large stretchability, excellent fatigue resistance, excellent thermal stability, good surface condition, and easy to post-process. A few commonly used elastomers might be good candidates (refer to Chapter 2.1), such as polydimethylsiloxane (PDMS) and thermoplastic polyurethane (TPU), since they both offer a wide range of elasticity (100%-400%). However, the hydrophobic surface condition of PDMS inhibits the application of inkjet printing. Though the PDMS surface can be converted to hydrophilic after UV-ozone treatment, the quality of printed pattern on PDMS is generally poor compared to that on PET substrates. Instead, TPU can be a better choice. Future studies on using TPU as flexible/stretchable substrates for flexible devices await systematic investigation.

7 Summary and outlook

In this doctoral study, novel experimental techniques involving fabrication, characterization, and electro-mechanical testing of CNT-based conductive films have been systematically investigated. There were many challenges encountered, and also several new findings discovered. These aspects and insights are summarized in the following.

Two different fabrication methods, namely, inkjet-printing and spin-coating, have been conducted, to fabricate highly flexible and durable conductive traces and films based on CNT dispersions.

Inkjet-printing has been revealed as a facile method to fabricate conductive traces consisting of MWCNTs on the PET substrate. It has offered several advantages while creating some challenges. Firstly, the average particle size of the CNT agglomerates has to suffice the requirement of the printhead. Agglomerate size, which should be 1/100th of the nozzle diameter, can be achieved by applying high power amplitude ultra-sonication. However, there is a limit, which is the average length of the MWCNTs (Nanocyl® NC7000™). Thus, continuous jetting of inks became unstable with time, due to the clogging issue of MWCNTs in the orifice of the printhead during longtime printing. Secondly, the printability of the CNT-ink is influenced by the ink properties, in which different properties have to be counter-balanced. The two most essential ink properties are viscosity and surface tension. Since the CNT-inks in this work were all water-based, the surface tension all meet the requirement for inkjet-printing. However, it was

required to increase the viscosity of the self-made MWCNT-ink. Adding rheology modifiers was not an option since they are hard to be removed after printing and can deteriorate the conductivity of the CNT films. The viscosity can be directly increased by increasing the weight loading of MWCNTs. A printable CNT-ink with 0.1wt% MWCNTs could be achieved. However, higher loading of CNTs leads to the clogging of the printhead very quickly. Thirdly, post-printing factors such as droplet spacing, coffee-stain effect, and sintering temperature have to be optimized, in order to form uniform lines. It is experimentally found that for a printhead with 70 µm nozzle diameter, a uniform line can form on PET substrate with a droplet spacing of roughly 60 µm at a sintering temperature around 50 °C. Based on the stable formation of uniform lines, large-area conductive traces (62 mm×4 mm) can be successfully deposited. Lastly, the conductivity of the printed trace is determined for different inks, printing parameters, and the number of printed layers. With only one printed layer of MWCNTs, very few MWCNTs were deposited, and no percolating network of MWCNTs is formed. With up to three passes of printing, the sheet resistance is still around 400 Kiloohms/sq. Based on an extrapolated method, it is shown that the sheet resistance can be further reduced down to around 440 Ohms/sq. if up to 5 passes were printed without the clogging issue.

In comparison, spin-coating does not suffer from as many challenges and has produced stable and consistent results. The spin-coating process is more tolerant with respect to varying ink properties and is not constrained by the agglomerate size and viscosity. It has been shown that large-area CNT conductive films in the size of $70 \times 70\ mm^2$ on PET substrate can be successfully prepared. The commercial CNT dispersion-Nanocyl® Aquacyl™ AQ0101 containing a loading of 1.0 wt% MWCNTs (also Nanocyl® NC7000™) has been deposited via spin-coating. Two different batches of CNT conductive films were fabricated, each batch includes samples with 1, 2, and 3 layers of MWCNTs. The first batch-"w/ Agg" was prepared via

a direct spin-coating after a short-time re-sonication of the AQ0101 dispersion. With up to 3 layers, the sheet resistance for the "w/ Agg" batch can be reduced down to around 400 Ohms/sq. The second batch-"w/o Agg" was prepared with an additional pretreatment step. The AQ0101 dispersion was firstly re-sonicated for a short time, and subsequently centrifugated. Only the supernatant from the centrifugated dispersion was used for the subsequent spin-coating. With also up to 3 layers, the sheet resistance for the "w/o Agg" batch is roughly 1.1 Kiloohms/sq. Though the sheet resistance of the "w/o Agg" samples is higher than that of the "w/ Agg" samples for the same number of layers, the film quality of the "w/o Agg" samples is much better. As shown by the SEM characterization, not only the large CNT agglomerates in the "w/ Agg" samples have been avoided, but also the homogeneity in thickness has been improved significantly. This result has proved the effectiveness of the pretreatment step in better controlling the CNT film quality. Besides, the "w/o Agg" samples possess a significantly improved electro-mechanical reliability than the "w/ Agg" samples.

The electro-mechanical reliability of the spin-coated CNT-based conductive films has been tested by *in-situ* resistance measurements during micro-tensile and bending fatigue testing. Detailed SEM, FIB, and HIM investigations have revealed the microstructure evolution during static and cyclic tensile deformation and the correlating mechanisms for the electrical resistance evolution of the "w/ Agg" samples and the "w/o Agg" samples.

The results of the micro-tensile tests have shown that all samples from both batches could sustain their electrical conductivity up to 50% tensile strain. Interestingly, the resistance-strain (R-S) curves of the "w/ Agg" and "w/o Agg" samples show a much lower increase in fractional resistance compared to that of metallic thin-films. The R-S relationship for metallic thin-films is characterized by the geometrical change and the constant volume during plastic deformation and subsequent additional increase in fractional resis-

tance due to crack formation and delamination. A new theoretical curve based on the assumption of a constant effective cross-section and a constant resistivity during tensile deformation has been introduced originally in this study, in order to fit and explain the electro-mechanical behavior of CNT-based conductive films under tensile loading. It was found that the R-S relationships of 1-layered (1L) and 2-layered (2L) films from both batches evolved below the "Constant cross-section" curve, indicating better electro-mechanical performance than the theoretical prediction. This improvement is due to the decrease in resistivity of the CNT network by straining. The 3-layered (3L) sample from both batches exhibited a non-linear increase in fractional resistance at higher tensile strains. The R-S curve of "w/ Agg_3L" evolved below the "Constant cross-section" curve at smaller strain (<20%) and showed a substantial increase at larger strain (>20%). The R-S curve of "w/o Agg_3L" evolved below the "Constant cross-section" curve at roughly 40% strain and then showed a slight increase up to 50% strain. The R-S curves of these two samples deviate above the theoretical curve due to the local damage formation in the CNT network. However, the local damage formation in the "w/ Agg_3L" sample is much more severe than that in the "w/o Agg_3L" sample. Overall, the fractional resistance evolution of the "w/o Agg" samples is better than that of the "w/ Agg" samples, and the intrinsic electrical conductivity of the CNT films even improves during straining. Detailed morphological characterizations have revealed the mechanisms behind this improvement. It is found that cracks tend to form within and along agglomerates and propagate further within the "w/ Agg" samples, whereas almost no cracks but only local neckings form within the "w/o Agg" samples. The bridging effect of CNTs plays a vital role in maintaining the conductivity of the "w/ Agg" samples and the "w/o Agg" samples up to different strain levels. Upon straining the "w/ Agg" samples to 50%, individual CNTs are pulled out from both sides of the cracks due to crack growth, and the CNTs can not bridge across the cracks anymore. Thus, open cracks of more than 10 μm in length are responsible for the

significant increase in fractional resistance of the "w/ Agg_3L" sample at a strain higher than 20%. However, these local cracks have not destroyed the whole percolating network of CNTs. On the other hand, the bridging effect of CNTs is always active for the "w/o Agg" samples; thus, their increase in fractional resistance is much lower, and the corresponding increase in fractional resistance is only due to the geometrical change of the CNT network.

The results of bending fatigue tests have shown that on the 125-µm thick PET substrate, CNT-based conductive films are fatigue-free at 1% and 2% strain amplitudes up to 1 million bending cycles and are fatigue-free at 3% strain amplitude till 200,000 bending cycles. The significant increase in fractional resistance for the samples imposed with a strain amplitude of 3% was only caused by the fatigue and rupture of the PET substrate. During the entire bending fatigue cycles, the electro-mechanical behavior of the CNT-based conductive films have experienced four major stages: (1) Rapid decrease in fractional resistance, (2) Gradual stagnation in fractional resistance, (3) Increase in fractional resistance, and (4) Abrupt increase in fractional resistance to infinity. However, the successive occurrence of these stages is governed by the applied strain amplitude and the number of CNT layers. For CNT films imposed with a strain amplitude of $\varepsilon_a < 3\%$, only Stage 1 and Stage 2 are involved. In Stage 1, the rapid decrease in fractional resistance is due to the cohesion effect among CNTs. In Stage 2, the decrease in fractional resistance has gradually stagnated, resulting in an almost constant fractional resistance. For CNT films imposed with a strain amplitude of $\varepsilon_a \geq 3\%$, not only Stage 1 and Stage 2 are involved in the beginning but also Stage 3 and 4 occur subsequently with increasing bending cycles. In Stage 3, strain localization due to shear band formation within the plastically deformed PET substrate leads to the local alignment of the CNT network, local crack formation in the CNT network, as well as crack formation and propagation in the PET substrate, which altogether causes the increase in fractional resistance. In Stage 4, the total rupture of the PET

substrate has led to the abrupt increase in fractional resistance to infinity. Therefore, the fatigue behavior of the PET substrate plays a decisive role in the electro-mechanical reliability of CNT-based conductive films. If the PET substrates do not fatigue and rupture at higher strain amplitudes, CNT-based conductive films could sustain much more than 1 million bending cycles, probably at an even higher strain amplitude than 3%. This superior electro-mechanical performance can not be rivaled by metallic counterparts, including AgNPs films and AgNWs films.

In summary, the electro-mechanical properties of CNT-based conductive traces/films are determined by the fabrication process, the morphology of the CNT network, and the deformation behavior of the polymer substrate. When the process parameters for preparing CNT conductive traces/films are optimized, the electrical conductivity can be significantly improved by a multiple layer deposition. Without the fatigue and rupture of the polymeric substrate, the electrical conductivity of CNT-based conductive films could sustain monotonic tensile strains of more than 50% and could be free of fatigue damage at a higher strain amplitude for more than 1 million bending cycles. Most importantly, two interesting phenomena related to CNT-based conductive films have been originally discovered in this study: (1) The intrinsic conductivity of CNT films on PET substrates even improves during tensile straining; (2) The cohesion effect among CNTs also improves the electrical conductivity of CNT films during cyclic bending.

As an outlook of this doctoral study, future work should pay more attention to not only improving the electrical conductivity of the CNT films but also developing new flexible substrates. It has been shown the industry-standard substrates-PET foils are not ideal for flexible devices demanding high reliability at higher strain amplitudes. Alternative flexible substrates are necessary. Developing new flexible substrates is not a straightforward process and is very challenging. A variety of essential requirements for the

flexible substrates have to be met, including large stretchability, excellent fatigue resistance, excellent thermal stability, good surface condition, and easy to post-process. Fewer polymer substrate can satisfy all the above requirements simultaneously. New systems of conductive films and flexible substrates can be developed based on the available polymers. Among them, elastomers, including polydimethylsiloxane (PDMS) and thermoplastic polyurethane (TPU), could be promising. Nevertheless, systematic studies and investigations should be conducted for applying these elastomers as the substrates for flexible devices.

Bibliography

[1] S. R. Forrest. The path to ubiquitous and low-cost organic electronic appliances on plastic. *Nature*, 428(6986):911–918, April 2004.

[2] B. D. Gates. Flexible electronics. *Science*, 323(5921):1566–1567, March 2009.

[3] B. Y. Ahn, E. B. Duoss, M. J. Motala, X. Guo, S.-Il Park, Y. Xiong, J. Yoon, R. G. Nuzzo, J. A. Rogers, and J. A. Lewis. Omnidirectional printing of flexible, stretchable, and spanning silver microelectrodes. *Science*, 323(5921):1590–1593, March 2009.

[4] M. S. Miller, J. C. O'Kane, A. Niec, R. S. Carmichael, and T. B. Carmichael. Silver nanowire/optical adhesive coatings as transparent electrodes for flexible electronics. *ACS Applied Materials & Interfaces*, 5(20):10165–10172, October 2013.

[5] Z. Cui, Y. Han, Q. Huang, J. Dong, and Y. Zhu. Electrohydrodynamic printing of silver nanowires for flexible and stretchable electronics. *Nanoscale*, 10(15):6806–6811, April 2018.

[6] A. Kamyshny and S. Magdassi. Conductive nanomaterials for printed electronics. *Small*, 10(17):3515–3535, September 2014.

[7] S. H. Chae and Y. H. Lee. Carbon nanotubes and graphene towards soft electronics. *Nano Convergence*, 1(1):15, April 2014.

[8] A. Kamyshny and S. Magdassi. Conductive nanomaterials for 2D and 3D printed flexible electronics. *Chemical Society Reviews*, 48(6):1712–1740, March 2019.

[9] S. Wagner and S. Bauer. Materials for stretchable electronics. *MRS Bulletin*, 37(3):207–213, March 2012.

[10] J. Jones, S. P. Lacour, S. Wagner, and Z. Suo. Stretchable wavy metal interconnects. *Journa of Vacuum Science & Technology A*, 22(4):1723–1725, 2004.

[11] D.-Y. Khang, H. Jiang, Y. Huang, and J. A. Rogers. A stretchable form of single-crystal silicon for high-performance electronics on rubber substrates. *Science*, 311(5758):208–212, January 2006.

[12] S. P. Lacour, S. Wagner, R. J. Narayan, T. Li, and Z. Suo. Stiff subcircuit islands of diamondlike carbon for stretchable electronics. *Journal of Applied Physics*, 100(1):014913, July 2006.

[13] J. A. Rogers, T. Someya, and Y. Huang. Materials and mechanics for stretchable electronics. *Science*, 327(5973):1603–1607, March 2010.

[14] D.-H. Kim, J. Xiao, J. Song, Y. Huang, and J. A. Rogers. Stretchable, curvilinear electronics based on inorganic materials. *Advanced Materials*, 22(19):2108–2124, May 2010.

[15] Z. Suo. Mechanics of stretchable electronics and soft machines. *MRS Bullutin*, 37(3):218–225, March 2012.

[16] C. F. Guo, Q. Liu, G. Wang, Y. Wang, Z. Shi, Z. Suo, C.-W. Chu, and Z. Ren. Fatigue-free, superstretchable, transparent, and biocompatible metal electrodes. *PNAS*, 112(40):12332–12337, October 2015.

[17] A. Kamyshny and S. Magdassi. *Nanomaterials for 2D and 3D printing*, chapter 7, pages 119–160. Wiley-VCH, Weinheim, Germany, 2017.

[18] K. D. Harris, A. L. Elias, and H.-J. Chung. Flexible electronics under strain: a review of mechanical characterization and durability enhancement strategies. *Journal of Materials Science*, 51(6):2771–2805, March 2016.

[19] S. Wunscher, R. Abbel, J. Perelaer, and U. S. Schubert. Progress of alternative sintering approaches of inkjet-printed metal inks and their application for manufacturing of flexible electronic devices. *Journal of Materials Chemistry C*, 2(48):10232–10261, September 2014.

[20] S. Logothetidis. Flexible organic electronic devices: Materials, process and applications. *Materials Science and Engineering B*, 152(1):96–104, August 2008.

[21] W. A. MacDonald, M. K. Looney, D. MacKerron, R. Eveson, R. Adam, K. Hashimito, and K. Rakos. Latest advances in substrates for flexible electronics. *Journal of the Society for Information Display*, 15(12):1075–1083, December 2007.

[22] D. J. Lipomi, M. Vosgueritchian, B. C-K. Tee, S. L. Hellstrom, J. A. Lee, C. H. Fox, and Z. Bao. Skin-like pressure and strain sensors based on transparent elastic films of carbon nanotubes. *Nature Nanotechnology*, 6(12):788–792, October 2011.

[23] S. J. Benight, C. Wang, J. B. H. Tok, and Z. Bao. Stretchable and self-healing polymers and devices for electronic skin. *Progress in Polymer Science*, 38(12):1961–1977, December 2013.

[24] Y. Leterrier, L. Médico, F. Demarco, J.-A. E. Månson, U. Betz, M. F. Escolá, M. Kharrazi Olsson, and F. Atamny. Mechanical integrity of transparent conductive oxide films for flexible polymer-based displays. *Thin Solid Films*, 460(1-2):156–166, July 2004.

[25] T. Li and Z. Suo. Ductility of thin metal films on polymer substrates modulated by interfacial adhesion. *International Journal of Solids and Structures*, 44(6):1696–1705, March 2007.

[26] S. Iijima. Helical microtubules of graphitic carbon. *Nature*, 354(6348):56–58, November 1991.

[27] K. S. Novoselov, A. K. Geim, S. V. Morozov, D. Jiang, Y. Zhang, S. V. Dubonos, I. V. Grigorieva, and A. A. Firsov. Electric field effect in atomically thin carbon films. *Science*, 306(5696):666–669, October 2004.

[28] D. Arthur, R. P. Silvy, P. Wallis, Y. Tan, J.-D. R. Rocha, D. Resasco, R. Praino, and W. Hurley. Carbon nanomaterial commercialization: Lessons for graphene from carbon nanotubes. *MRS Bulletin*, 37(12):1297–1306, December 2012.

[29] J.-H. Lee, N.-R. Kim, B.-J. Kim, and Y.-C. Joo. The improved mechanical performance of solution-processed MWCNT/Ag nanoparticle composite films with oxygen-pressure-controlled annealing. *Carbon*, 50(1):98–106, January 2012.

[30] Thomas Haas. *Mechanische Zuverlässigkeit von gedruckten und gasförmig abgeschiedenen Schichten auf flexiblem Substrat*. PhD thesis, Karlsruhe Institute of Technology, Karlsruhe, Germany, June 2014.

[31] S. Zhang, H. Zhang, G. Yao, F. Liao, M. Gao, Z. Huang, K. Li, and Y. Lin. Highly stretchable, sensitive, and flexible strain sensors based on silver nanoparticles/carbon nanotubes composites. *Journal of Alloys and Compounds*, 652:48–54, December 2015.

[32] B. Hwang, X. Li, S. H. Kim, and S. Lim. Effect of carbon nanotube addition on mechanical reliability of Ag nanowire network. *Materials Letters*, 198:202–205, July 2017.

[33] P. T. Hoang, N. Salazar, T. N. Porkka, K. Joshi, T. Liu, T. J. Dickens, and Z. Yu. Engineering crack formation in carbon nanotube-silver nanoparticle composite films for sensitive and durable piezoresistive sensors. *Nanoscale Research Letters*, 11(1):422–428, September 2016.

[34] T. Yamada, Y. Hayamizu, Y. Yamamoto, Y. Yomogida, A. Izadi-Najafabadi, D. N. Futaba, and K. Hata. A stretchable carbon nan-

otube strain sensor for human-motion detection. *Nature Nanotechnology*, 6(5):296–301, May 2011.

[35] L. Cai, L. Song, P. Luan, Q. Zhang, N. Zhang, Q. Gao, D. Zhao, X. Zhang, M. Tu, F. Yang, W. Zhou, Q. Fan, J. Luo, W. Zhou, P. M. Ajayan, and S. Xie. Super-stretchable, transparent carbon nanotube-based capacitive strain sensors for human motion detection. *Scientific Reports*, 3(3048), October 2013.

[36] M. Amjadi, Y. J. Yoon, and I. Park. Ultra-stretchable and skin-mountable strain sensors using carbon nanotubes-Ecoflex nanocomposites. *Nanotechnology*, 26(37):375501, September 2015.

[37] J. P. Bastos, S. Manghooli, M. Jaysankar, J. G. Tait, W. Qiu, R. Gehlhaar, M. De Volder, G. Uytterhoeven, J. Poortmans, and U. W. Paetzold. Low-cost electrodes for stable perovskite solar cells. *Applied Physics Letters*, 110(23):233902, June 2017.

[38] S. Azoubel, S. Shemesh, and S. Magdassi. Flexible electroluminescent device with inkjet-printed carbon nanotube electrodes. *Nanotechnology*, 23(34):334003, August 2012.

[39] M. M. J. Treacy, T. W. Ebbesen, and J. M. Gibson. Exceptionally high Young's modulus observed for individual carbon nanotubes. *Nature*, 381(6584):678–680, June 1996.

[40] A. Krishnan, E. Dujardin, T. W. Ebbesen, P. N. Yianilos, and M. M. J. Treacy. Young's modulus of single-walled nanotubes. *Physical Review B*, 58(20):14013–14019, November 1998.

[41] M.-F. Yu, O. Lourie, M. J. Dyer, K. Moloni, T. F. Kelly, and R. S. Ruoff. Strength and breaking mechanism of multiwalled carbon nanotubes under tensile load. *Science*, 287(5453):637–640, January 2000.

[42] M.-F. Yu, B. S. Files, S. Arepalli, and R. S. Ruoff. Tensile loading of ropes of single wall carbon nanotubes and their mechanical properties. *Physical Review Letters*, 84(24):5552–5555, June 2000.

[43] E. T. Thostenson, Z. Ren, and T.-W. Chou. Advances in the science and technology of carbon nanotubes and their composites: a review. *Composites Science and Technology*, 61(13):1899–1912, October 2001.

[44] T. W. Odom, J.-L. Huang, P. Kim, and C. M. Lieber. Atomic structure and electronic properties of single-walled carbon nanotubes. *Nature*, 391(6662):62–64, January 1998.

[45] G. D. Nessim. Properties, synthesis, and growth mechanisms of carbon nanotubes with special focus on thermal chemical vapor deposition. *Nanoscale*, 2(8):1306–1323, August 2010.

[46] P. L. McEuen, M. Fuhrer, and H. Park. Single-walled carbon nanotube electronics. *IEEE Transactions on Nanotechnology*, 1(1):78–85, March 2002.

[47] A. Bachtold, M. Henny, C. Terrier, C. Strunk, C. Schonenberger, J.-P. Salvetat, J.-M. Bonard, and L. Forro. Contacting carbon nanotubes selectively with low-ohmic contacts for four-probe electric measurements. *Applied Physics Letters*, 73(2):274–276, July 1998.

[48] Q. Li, X. Zhang Y. Li, S. B. Chikkannanavar, Y. Zhao, A. M. Dangelewicz, L. Zheng, S. K. Doorn, Q. Jia, D. E. Peterson, P. N. Arendt, and Y. Zhu. Structure-dependent electrical properties of carbon nanotube fibers. *Advanced Materials*, 19(20):3358–3363, October 2007.

[49] L. Hu, D. S. Hecht, and G. Grüner. Carbon nanotube thin films: fabrication, properties, and applications. *Chemical Reviews*, 110(10):5790–5844, July 2010.

[50] A. P. Graham, G. S. Duesberg, W. Hoenlein, F. Kreupl, M. Liebau, R. Martin, B. Rajasekharan, W. Pamler, R. Seidel, W. Steinhoegl, and E. Unger. How do carbon nanotubes fit into the semiconductor roadmap? *Applied Physics A: Materials Science & Processing*, 80(6):1141–1151, March 2005.

[51] D. S. Bethune, C. H. Kiang, M. S. de Vries, G. Gorman, R. Savoy, J. Vazquez, and R. Beyers. Cobalt-catalysed growth of carbon nanotubes with single-atomic-layer walls. *Nature*, 363(6430):605–607, June 1993.

[52] C. Journet, W. K. Maser, P. Bernier, A. Loiseau, M. Lamy de la Chapelle, S. Lefrant, P. Deniard, R. Lee, and J. E. Fischer. Large-scale production of single-walled carbon nanotubes by the electric-arc technique. *Nature*, 388(6644):756–758, August 1997.

[53] A. Thess, R. Lee, P. Nikolaev, H. J. Dai, P. Petit, J. Robert, C. H. Xu, Y. H. Lee, S. G. Kim, A. G. Rinzler, D. T. Colbert, G. E. Scuseria, D. Tomanek, J. E. Fischer, and R. E. Smalley. Crystalline ropes of metallic carbon nanotubes. *Science*, 273(5274):483–487, July 1996.

[54] C. D. Scott, S. Arepalli, P. Nikolaev, and R. E. Smalley. Growth mechanisms for single-wall carbon nanotubes in a laser-ablation process. *Applied Physics A: Material Science Process*, 72(5):573–580, March 2001.

[55] S. Roy, M. David-Pur, and Y. Hanein. Carbon nanotube growth inhibition in floating catalyst based chemical vapor deposition and its application in flexible circuit fabrication. *Carbon*, 116:40–49, May 2017.

[56] Y. Yamamoto, S. Inoue, and Y. Matsumura. Thermal decomposition products of various carbon sources in chemical vapor deposition synthesis of carbon nanotube. *Diamond and Related Materials*, 75:1–5, May 2017.

[57] P. Nikolaev. Gas-phase production of single-walled carbon nanotubes from carbon monoxide: a review of the HiPco process. *Journal of Nanoscience and Nanotechnology*, 4(4):307–316, April 2004.

[58] S. Magdassi. *The Chemistry of Inkjet Inks*. World Scientific Pub. Co., Singapore; Hackensack, NJ; London, 2010.

[59] R. Sweet. Fluid droplet recorder, U.S. Patent No. 3596275, 1971.

[60] S. Zoltan. Pulsed droplet ejecting system, U.S. Patent No. 3683212, 1972.

[61] N. Stemme. Arrangement of writing mechanisms for writing on paper with a colored liquid, U.S. Patent No. 3747120, 1973.

[62] E. L. Kyser and S. B. Sears. Method and apparatus for recording with writing fluids and drop projection means therefor, U.S. Patent No. 3946398, 1976.

[63] R. P. Tortorich and J.-W. Choi. Inkjet printing of carbon nanotubes. *Nanomaterials*, 3(3):453–468, July 2013.

[64] M. Gao, L. Li, and Y. Song. Inkjet printing wearable electronic devices. *Journal of Materials Chemistry C*, 5(12):2971–2993, March 2017.

[65] T. J. Simmons, D. Hashim, R. Vajtai, and P. M. Ajayan. Large area-aligned arrays from direct deposition of single-wall carbon nanotube inks. *Journal of the American Chemical Society*, 129(33):10088–10089, August 2007.

[66] M. F. Islam, E. Rojas, D. M. Bergey, A. T. Johnson, and A. G. Yodh. High weight fraction surfactant solubilization of single-wall carbon nanotubes in water. *Nano Letters*, 3(2):269–273, January 2003.

[67] L. Vaisman, G. Marom, and H. D. Wagner. Dispersions of surface-modified carbon nanotubes in water-soluble and water-insoluble

polymers. *Advanced Functional Materials*, 16(3):357–363, January 2006.

[68] E. A. Whitsitt and A. R. Barron. Silica coated single walled carbon nanotubes. *Nano Letters*, 3(6):775–778, May 2003.

[69] R. Rastogi, R. Kaushal, S. K. Tripathi, A. L. Sharma, I. Kaur, and L. M. Bharadwaj. Comparative study of carbon nanotube dispersion using surfactants. *Journal of Colloid and Interface Science*, 328(2):421–428, December 2008.

[70] H. Wang, W. Zhou, D. L. Ho, K. I. Winey, J. E. Fischer, C. J. Glinka, and E. K. Hobbie. Dispersing single-walled carbon nanotubes with surfactants: a small angle neutron scattering study. *Nano Letters*, 4(9):1789–1793, August 2004.

[71] J. Yu, N. Grossiord, C. E. Koning, and J. Loos. Controlling the dispersion of multi-wall carbon nanotubes in aqueous surfactant solution. *Carbon*, 45(3):618–623, March 2007.

[72] A. Iborra, G. Diaz, D. Lopez, J. M. Giussi, and O. Azzaroni. Copolymer based on lauryl methacrylate and poly(ethylene glycol) methyl ether methacrylate as amphiphilic macrosurfactant: synthesis, characterization and their application as dispersing agent for carbon nanotubes. *European Polymer Journal*, 87:308–317, February 2017.

[73] D. H. Napper. Steric stabilization. *Journal of Colloid and Interface Science*, 58(2):390–407, February 1977.

[74] Margaret Robins and Annette Fillery-Travis. *Colloidal Dispersions*. Cambridge University Press, Cambridge, UK, 1989.

[75] S. Ramaswamy. Issues in the statistical mechanics of steady sedimentation. *Advances in Physics*, 50(3):297–341, March 2001.

[76] G. Meichsner, T. G. Mezger, and J. Schröder. *Lackeingenschaften messen and steuern*. Vincentz Network, Hannover, Germany, 2003.

[77] T. Shimoda, K. Morii, S. Seki, and H. Kiguchi. Inkjet printing of light-emitting polymer displays. *MRS Bulletin*, 28(11):821–827, November 2003.

[78] E. Tekin, P. J. Smith, and U. S. Schubert. Inkjet printing as a deposition and patterning tool for polymers and inorganic particles. *Soft Matter*, 4(4):703–713, February 2008.

[79] B. Derby. Inkjet printing of functional and structural materials: Fluid property requirements, feature stability, and resolution. *Annual Review of Materials Research*, 40(1):395–414, August 2010.

[80] Y.-F. Liu, M.-H. Tsai, Y.-F. Pai, and W.-S. Hwang. Control of droplet formation by operating waveform for inks with various viscosities in piezoelectric inkjet printing. *Applied Physics A*, 111(2):509–516, January 2013.

[81] J. E. Fromm. Numerical calculation of the fluid dynamics of drop-on-demand jets. *IBM Journal of Research and Development*, 28(3):322–333, May 1984.

[82] B. Derby and N. Reis. Inkjet printing of highly loaded particulate suspensions. *MRS Bulletin*, 28(11):815–818, November 2003.

[83] Ph. Buffat and J.-P. Borel. Size effect on the melting temperature of gold particles. *Physical Review A*, 13(6):2287–2298, June 1976.

[84] K. Dick, T. Dhanasekaran, Z. Zhang, and D. Meisel. Size-dependent melting of silica-encapsulated gold nanoparticles. *Journal of the American Chemical Society*, 124(10):2312–2317, March 2002.

[85] I. Reinhold. *Nanomaterials for 2D and 3D printing*, chapter 2, pages 27–49. Wiley-VCH Verlag, Weinheim, Germany, 2017.

[86] F. M. Wolf, J. Perelaer, S. Stumpf, D. Bollen, F. Kriebel, and U. S. Schubert. Rapid low-pressure plasma sintering of inkjet-printed silver nanoparticles for RFID antennas. *Journal of Materials Research*, 28(9):1254–1261, May 2013.

[87] J. Perelaer, M. Klokkenburg, C. E. Hendriks, and U. S. Schubert. Microwave flash sintering of inkjet-printed silver tracks on polymer substrates. *Advanced Materials*, 21(47):4830–4834, December 2009.

[88] Y. Farraj, M. Bielman, and S. Magdassi. Inkjet printing and rapid ebeam sintering enable formation of highly conductive patterns in roll to roll process. *RSC Advances*, 7(25):15463–15467, March 2017.

[89] M. J. Coutts, M. B. Cortie, M. J. Ford, and A. M. McDonagh. Rapid and controllable sintering of gold nanoparticle inks at room temperature using a chemical agent. *Journal of Physical Chemistry C*, 113(4):1325–1328, January 2009.

[90] K. Kordas, T. Mustonen, G. Toth, H. Jantunen, M. Lajunen, C. Soldano, S. Talapatra, S. Kar, R. Vajtai, and P. M. Ajayan. Inkjet printing of electrically conductive patterns of carbon nanotubes. *Small*, 2(8-9):1021–1025, August 2006.

[91] A. Stern, S. Azoubel, E. Sachyani, G. Livshits, D. Rotem, S. Magdassi, and D. Porath. Conductivity enhancement of transparent 2D carbon nanotube networks occurs by resistance reduction in all junctions. *Journal of Physical Chemistry C*, 122(26):14872–14876, June 2018.

[92] Y. Leterrier. Durability of nanosized oxygen-barrier coatings on polymers. *Progress in Materials Science*, 48(1):1–55, December 2003.

[93] D. Vella, J. Bico, A. Boudaoud, B. Roman, and P. M. Reis. The macroscopic delamination of thin films from elastic substrates. *PNAS*, 106(27):10901–10906, July 2009.

[94] Z. Suo, E. Y. Ma, H. Gleskove, and S. Wagner. Mechanics of rollable and foldable film-on-foil electronics. *Applied Physics Letters*, 74(8):1177–1179, February 1999.

[95] N. Lu, X. Wang, Z. Suo, and J. Vlassak. Metal films on polymer substrates stretched beyond 50%. *Applied Physics Letters*, 91(22):221909, November 2007.

[96] Beckwith, G. Thomas, N. Lewis Buck, and Roy D. Marangoni. *Mechnical Measurements, 3rd Edition*, page 360. Addison-Wesley Publishing Co. Reading, MA, 1982.

[97] C. Niu. Carbon nanotube transparent conducting films. *MRS Bulletin*, 36(10):766–773, October 2011.

[98] S. Suresh. *Fatigue of Materials*. Cambridge University Press, Cambridge, UK, 2 edition, 1998.

[99] W. D. Nix. Mechanical properties of thin films. *Metallurgical Transactions A*, 20(11):2217–2245, November 1989.

[100] R.-M. Keller, S. P. Baker, and E. Arzt. Quantitative analysis of strengthening mechanisms in thin Cu films: Effects of film thickness, grain size, and passivation. *Journal of Materials Research*, 13(5):1307–1317, May 1998.

[101] E. Arzt. Size effects in materials due to microstructural and dimensional constraints: A comparative review. *Acta Materialia*, 46(16):5611–5626, October 1998.

[102] O. Kraft, R. Schwaiger, and P. Wellner. Fatigue in thin films: Lifetime and damage formation. *Materials Science and Engineering: A*, 319-321:919–923, December 2001.

[103] Ruth Schwaiger. *Fatigue Behavior of Sub-Micron Silver and Copper Films*. PhD thesis, University of Stuttgart, Stuttgart, December 2001.

[104] O. Kraft and C. Volkert. Mechanical testing of thin films and small structures. *Advanced Engineering Materials*, 3(3):99–110, March 2001.

[105] G.-D. Sim, Y. Hwangbo, H.-H. Kim, S.-B. Lee, and J. J. Vlassak. Fatigue of polymer-supported Ag thin films. *Scripta Materialia*, 66(11):915–918, June 2012.

[106] O. Kraft, P. Wellner, M. Hommel, R. Schwaiger, and E. Arzt. Fatigue behavior of polycrystalline thin copper films. *Zeitschrift für Metallkunde*, 93(5):392–400, May 2002.

[107] R. Schwaiger and O. Kraft. Size effects in the fatigue behavior of thin Ag films. *Acta Materialia*, 51(1):195–206, January 2003.

[108] P. Lall, A. Angral, and J. Suhling. Board trace fatigue models and design guidelines for electronics under shock-impact. In *Proceedings of ITHERM 2010*, Las Vegas, NV, June 2010. IEEE.

[109] B.-J. Kim, H.-A-S. Shin, S.-Y. Jung, Y. Cho, O. Kraft, I.-S. Choi, and Y.-C. Joo. Crack nucleation during mechanical fatigue in thin metal films on flexible substrates. *Acta Materialia*, 61(9):3473–3481, May 2013.

[110] G. P. Zhang, C. A. Volkert, R. Schwaiger, P. Wellner, E. Arzt, and O. Kraft. Length-scale-controlled fatigue mechanisms in thin copper films. *Acta Materialia*, 54(11):3127–3139, June 2006.

[111] G. P. Zhang, C. A. Volkert, R. Schwaiger, R. Mönig, and O. Kraft. Fatigue and thermal fatigue damage analysis of thin metal films. *Microelectronics Reliability*, 47(2007):2007–2013, June 2007.

[112] D. Wang, C. A. Volkert, and O. Kraft. Effect of length scale on fatigue life and damage formation in thin Cu films. *Materials Science and Engineering: A*, 493(1-2):267–273, October 2008.

[113] N. Lu, Z. Suo, and J. J. Vlassak. The effect of film thickness on the failure strain of polymer-supported metal films. *Acta Materialia*, 58(5):1679–1687, March 2010.

[114] G.-D. Sim, S. Won, and S.-B. Lee. Tensile and fatigue behaviors of printed Ag thin films on flexible substrates. *Applied Physics Letters*, 101(19):191907, November 2012.

[115] O. Glushko, A. Klug, E. J. W. List-Kratochvil, and M. J. Cordill. Monotonic and cyclic mechanical reliability of metallization lines on polymer substrates. *Journal of Materials Research*, 32(9):1760–1769, May 2017.

[116] B.-J. Kim, T. Haas, A. Friederich, J.-H. Lee, D.-H. Nam, J. R. Binder, W. Bauer, I.-S. Choi, Y.-C. Joo, P. A. Gruber, and O. Kraft. Improving mechanical fatigue resistance by optimizing the nanoporous structure of inkjet-printed Ag electrodes for flexible devices. *Nanotechnology*, 25(12):125706, March 2014.

[117] B. Hwang, H.-A-S. Shin, T. Kim, Y.-C. Joo, and S. M. Han. Highly reliable Ag nanowire flexible transparent electrode with mechanically welded junctions. *Small*, 10(16):3397–3404, August 2014.

[118] M. Park, W. Kim, B. Hwang, and S. M. Han. Effect of varying the density of Ag nanowire networks on their reliability during bending fatigue. *Scripta Materialia*, 161:70–73, March 2019.

[119] C. F. Guo and Z. Ren. Flexible transparent conductors based on metal nanowire networks. *Materials Today*, 18(3):143–154, April 2015.

[120] S. Khan and L. Lorenzelli. Recent advances of conductive nanocomposites in printed and flexible electronics. *Smart Materials and Structures*, 26(8):Article ID. 083001, August 2017.

[121] S. K. Eshkalak, A. Chinnappan, W.A.D.M. Jayathilaka, M. Khatibzadeh, E. Kowsari, and S. Ramakrishna. A review on inkjet printing of CNT composites for smart applications. *Applied Materials Today*, 9:372–386, December 2017.

[122] J. Stringer and B. Derby. Formation and stability of lines produced by inkjet printing. *Langmuir*, 26(12):10365–10372, May 2010.

[123] M. S. Dresselhaus, G. Dresselhaus, R. Saito, and A. Jorio. Raman spectroscopy of carbon nanotubes. *Physics Reports*, 409(2):47–99, March 2005.

[124] C. M. White, R. Banks, I. Hamerton, and J. F. Watts. Characterisation of commercially CVD grown multi-walled carbon nanotubes for paint applications. *Progress in Organic Coatings*, 90:44–53, January 2016.

[125] F. A. Jenkins and H. E. White. *Fundamentals of Optics, 3rd Edition*, page 297. McGraw Hill, New York, 1957.

[126] ISO 13320:2009 Particle size analysis – Laser diffraction methods. Standard, International Organization for Standardization, Geneva, Switzerland, October 2009.

[127] R. McKennell. Cone-Plate Viscometer. *Analytical Chemistry*, 28(11):1710–1714, November 1956.

[128] H.-J. Butt, K. Graf, and M. Kappl. *Physics and chemistry of interfaces, English Edition, 2. Revision*, chapter 2, pages 15–16. Wiley-VCH Verlag, Weinheim, Germany, 2006.

[129] A. Pietrikova, P. Lukacs, D. Jakubeczyova, B. Ballokova, J. Potencki, G. Tomaszewski, J. Pekarek, K. Prikrylova, and M. Fides. Surface analysis of polymeric substrates used for inkjet printing technology. *Circuit World*, 42(1):9–16, February 2016.

[130] G. H. Michler. Electron microscopy in polymer science. *Applied Spectroscopy Reviews*, 28(4):327–384, December 1993.

[131] C. Gaillard, P. A. Stadelmann, C. J. G. Plummer, and G. Fuchs. Practical method for high-resolution imaging of polymers by low-voltage scanning electron microscopy. *Scanning*, 26(3):122–130, May 2004.

[132] B. W. Ward, John A. Notte, and N. P. Economou. Helium ion microscope: A new tool for nanoscale microscopy and metrology. *Journal of Vacuum Science and Technology B*, 24(6):2871, November 2006.

[133] M. S. Joens, C. Huynh, J. M. Kasuboski, D. Ferranti, Y. J. Sigal, F. Zeitvogel, M. Obst, C. J. Burkhardt, K. P. Curran, S. H. Chalasani, L. A. Stern, B. Goetze, and J. A. J. Fitzpatrick. Helium ion microscopy for the imaging of biological samples at sub-nanometer resolution. *Scientific Reports*, 3(1):3514, December 2013.

[134] G. Hlawacek, V. Veligura, R. van Gastel, and B. Poelsema. Helium ion microscopy. *Journal of Vacuum Science and Technology B*, 32(2):020801, February 2014.

[135] S. Brunauer, P. H. Emmett, and E. Teller. Adsorption of gases in multimolecular layers. *Journal of the American Chemical Society*, 60(2):309–319, February 1938.

[136] S. Lowell, Joan E. Shields, Martin A. Thomas, and Matthias Thommes. *Characterization of Porous Solids and Powders: Surface Area, Pore Size and Density*, volume 16 of *Particle Technology*. Springer, Dordrecht, Netherlands, 1 edition, 2004.

[137] M. Thommes, K. Kaneko, A. V. Neimark, J. P. Olivier, F. Rodriguez-Reinoso, J. Rouquerol, and K. S. W. Sing. Physisorption of gases, with special reference to the evaluation of surface area and pore size distribution (IUPAC technical report). *Pure and Applied Chemistry*, 87(9-10):1051–1069, July 2015.

[138] D. Soltman and V. Subramanian. Inkjer-printed line morphologies and temperature control of the coffee ring effect. *Langmuir*, 24(5):2224–2231, January 2008.

[139] N. Rouhi, D. Jain, and P. J. Burke. High-performance semiconducting nanotube inks: Progress and prospects. *ACS Nano*, 5(11):8471–8487, October 2011.

[140] T. Kim, H. Song, J. Ha, S. Kim, D. Kim, S. Chung, J. Lee, and Y. Hong. Inkjet-printed stretchable single-walled carbon nanotube

electrodes with excellent mechanical properties. *Applied Physics Letters*, 104(11):113103, March 2014.

[141] H. Assender, V. Bliznyuk, and K. Porfyrakis. How surface topography relates to materials' properties. *Science*, 297(5583):973–976, August 2002.

[142] C. Li, E. T. Thostenson, and T.-W. Chou. Effect of nanotube waviness on the electrical conductivity of carbon nanotube-based composites. *Composites Science and Technology*, 68(6):1445–1452, May 2008.

[143] W. Obitayo and T. Liu. A reivew: Cabon nanotube-based piezoresistive strain sensors. *Journal of Sensors*, 2012(652438):1–15, April 2012.

[144] G. Sapra, R. Vig, and M. Sharma. Simulation and analysis of strain sensitivity of CNT-based strain sensors. *International Journal of Nanoscience*, 15(5&6):1660005, October 2016.

[145] C. Berger, Y. Yi, Z. L. Wang, and W. A. De Heer. Multiwalled carbon nanotubes are ballistic conductors at room temperature. *Applied Physics A*, 74(3):363–365, March 2002.

[146] M. Zamkov, A. S. Alnaser, B. Shan, Z. Chang, and P. Richard. Probing the intrinsic conductivity of multiwalled carbon nanotubes. *Applied Physics Letters*, 89(9):093111, August 2006.

[147] M. S. Fuhrer, J. Nygård, L. Shih, M. Forero, Young-Gui Yoon, M. S. C. Mazzoni, Hyoung Joon Choi, Jisoon Ihm, Steven G. Louie, A. Zettl, and Paul L. McEuen. Crossed nanotube junctions. *Science*, 288(5465):494–497, April 2000.

[148] A. Buldum and J. P. Lu. Contact resistance between carbon nanotubes. *Physical Review B*, 63(16):161403, April 2001.

[149] J. G. Simmons. Generalized formula for the electric tunnel effect between similar electrodes separated by a thin insulating film. *Journal of Applied Physics*, 34(6):1793–1803, 1963.

[150] P. Sheng, E. K. Sichel, and J. I. Gittleman. Fluctuation-induced tunneling conduction in carbon-polyvinylchloride composites. *Physical Review Letters*, 40(18):1197–1200, May 1978.

[151] Y. Yu, G. Song, and L. Sun. Determinant role of tunneling resistance in electrical conductivity of polymer composites reinforced by well dispersed carbon nanotubes. *Journal of Applied Physics*, 108(8):084319, October 2010.

[152] X. Wang, J. Li, H. Song, H. Huang, and J. Gou. Highly stretchable and wearable strain sensor based on printable carbon nanotube layers/polydimethylsiloxane composites with adjustable sensitivity. *ACS Applied Materials & Interfaces*, 10(8):7371–7380, February 2018.

[153] P. Dharap, Z. Li, S. Nagarajaiah, and E. V. Barrera. Nanotube film based on single-wall carbon nanotubes for strain sensing. *Nanotechnology*, 15(3):379–382, January 2004.

[154] J.-H. Pu, X.-J. Zha, M. Zhao, S. Li, R.-Y. Bao, Z.-Y. Liu, B.-H. Xie, M.-B. Yang, Z. Guo, and W. Yang. 2D End-to-end carbon nanotube conductive networks in polymer nanocomposites: A conceptual design to dramatically enhance sensitivities of strain sensors. *Nanoscale*, 10(5):2191–2198, February 2018.

[155] L. Ma, W. Yang, Y. Wang, H. Chen, Y. Xing, and J. Wang. Multidimensional strain sensor based on carbon nanotube film with aligned conductive networks. *Composites Science and Technology*, 165:190–197, September 2018.

[156] L. Jin, A. Chortos, F. Lian, E. Pop, C. Linder, Z. Bao, and W. Cai. Microstructural origin of resistance-strain hysteresis in carbon nanotube thin film conductors. *PNAS*, 115(9):1986–1991, February 2018.

[157] L. Licea-Jimenez, P. Y. Henrio, A. Lund, T. M. Laurie, S. A. Perez-Garcia, L. Nyborg, H. Hassander, H. Bertilsson, and R. W. Rychwal-

ski. MWNT reinforced melamine-formaldehyde containing alpha-cellulose. *Composites Science and Technology*, 67(5):844–854, April 2007.

[158] P. Slobodian, P. Riha, A. Lengalova, R. Olejnik, D. Kimmer, and P. Saha. Effect of compressive strain on electric resistance of multi-wall carbon nanotube networks. *Journal of Experimental Nanoscience*, 6(3):294–304, May 2011.

[159] N. Hu, Y. Karube, C. Yan, Z. Masuda, and H. Fukunaga. Tunneling effect in a polymer/carbon nanotube nanocomposite strain sensor. *Acta Materialia*, 56(13):2929–2936, August 2008.

[160] W. Ding, L. Calabri, K. M. Kohlhaas, X. Chen, D. A. Dikin, and R. S. Ruoff. Modulus, fracture strength, and brittle vs. plastic response of the outer shell of arc-grown multi-walled carbon nanotubes. *Experimental Mechanics*, 47(1):25–36, February 2007.

[161] R. Andrews and M. C. Weisenberger. Carbon nanotube polymer composites. *Current Opinion in Solid State and Materials Science*, 8(1):31–37, January 2004.

[162] A. Chortos, G. I. Koleilat, R. Pfattner, D. Kong, P. Lin, R. Nur, T. Lei, H. Wang, N. Liu, Y.-C. Lai, M.-G. Kim, J. W. Chung, S. Lee, and Z. Bao. Mechanically durable and highly stretchable transistors employing carbon nanotube semiconductor and electrodes. *Advanced Materials*, 28(22):4441–4448, June 2016.

[163] L. Cai, J. Li, P. Luan, H. Dong, D. Zhao, Q. Zhang, X. Zhang, M. Tu, Q. Zeng, W. Zhou, and S. Xie. Highly transparent and conductive stretchable conductors based on hierarchical reticulate single-walled carbon nanotube architechture. *Advanced Functional Materials*, 22(24):5238–5244, December 2012.

[164] R. Zhang, H. Deng, R. Valenca, J. Jin, Q. Fu, E. Bilotti, and T. Peijs. Strain sensing behaviour of elastomeric composite films containing

carbon nanotubes under cyclic loading. *Composites Science Technology*, 74:1–5, January 2013.

[165] M. Amjadi, A. Pichitpajongkit, S. Lee, S. Ryu, and I. Park. Highly stretchable and sensitive strain sensor based on silver nanowire-elastomer nanocomposite. *ACS Nano*, 8(5):5154–5163, April 2014.

[166] Shu Li. *Electrical properties of carbon nanotube networks: Characterization, modeling and sensor applications*. PhD thesis, Florida State University, Tallahassee, FL, 2012.

[167] F. Du, J. E. Fischer, and K. I. Winey. Effect of nanotube alignment on percolation conductivity in carbon nanotube/polymer composites. *Physical Review B*, 72(12):121404, September 2005.

[168] S. Kumar, J. Y. Murthy, and M. A. Alam. Percolating conduction in finite nanotube networks. *Physical Review Letter*, 95(6):066802, August 2005.

[169] N. Pimparkar, Q. Cao, S. Kumar, J. Y. Murthy, J. Rogers, and M. A. Alam. Current-voltage characteristics of long-channel nanobundle thin-film transistors: a "bottom-up" perspective. *IEEE Electron Device Letters*, 28(2):157–160, February 2007.

[170] A. N. Volkov and L. V. Zhigilei. Scaling laws and mesoscopic modeling of thermal conductivity in carbon nanotube materials. *Physical Review Letters*, 104(21):215902, May 2010.

[171] F. Lian, J. P. Llinas, Z. Li, D. Estrada, and E. Pop. Thermal conductivity of chirality-sorted carbon nanotube networks. *Applied Physics Letters*, 108(10):103101, March 2016.

[172] O. Glushko and M. J. Cordill. Electrical resistance of metal films on polymer substrates under tension. *Experimental Techniques*, 40(1):303–310, February 2016.

[173] D. V. Wagle and G. A. Baker. Cold welding: a phenomenon for spontaneous self-healing and shape genesis at the nanoscale. *Materials Horizons*, 2(2):127, January 2015.

[174] C. F. Guo, Y. Lan, T. Sun, and Z. Ren. Deformation-induced cold-welding for self-healing of super-durable flexible transparent electrodes. *Nano Energy*, 8:110–117, September 2014.

[175] O. Suekane, A. Nagataki, H. Mori, and Y. Nakayama. Static friction force of carbon nanotube surfaces. *Applied Physics Express*, 1(6):064001, May 2008.

[176] S. Rabinowitz and P. Beardmore. Cyclic deformation and fracture of polymers. *Journal of Materials Science*, 9(1):81–99, January 1974.

[177] P. Beardmore and S. Rabinowitz. *Plastic Deformation of Materials*, volume 6 of *Treatise on Materials Science and Technology*. Academic Press, New York, 1975.

[178] P. Beardmore. Fatigue behavior of polymers. In J. T. Fong, editor, *Fatigue Mechanisms*, volume ASTM STP 675, pages 453–470. Proceedings of an ASTM-NBM-NSF symposium, Kansas City, MO, May 1978, American Society for Testing and Materials, 1979.

[179] P. B. Bowden and R. J. Young. Deformation mechanisms in crystalline polymers. *Journal of Materials Science*, 9(12):2034–2051, December 1974.

[180] S. Lee and G. C. Rutledge. Plastic deformation of semicrystalline polyethylene by molecular simulation. *Macromolecules*, 44(8):3096–3108, March 2011.

[181] S. Jabbari-Farouji, J. Rottler, O. Lame, A. Makke, M. Perez, and J.-L. Barrat. Plastic deformation mechanisms of semicrystalline and amorphous polymers. *ACS Macro Letters*, 4(2):147–150, January 2015.

[182] L. Lin and A. S. Argon. Structure and plastic deformation of polyethylene. *Journal of Materials Science*, 29(2):294–323, January 1994.

[183] H. H. Kausch, R. Gensler, Ch. Grein, C. J. G. Plummer, and P. Scaramuzzino. Crazing in semicrystalline thermoplastics. *Journal of Macromolecular Science, Part B*, 38(5-6):803–815, March 1999.

[184] Klaus Friedrich. Crazes and shear bands in semi-crystalline thermoplastics. In H. H. Kausch, editor, *Crazing in Polymers*, volume 52-53 of *Advances in Polymer Science*, pages 225–274. Springer-Verlag, Berlin, Heidelberg, Germany, 1983.

[185] J. M. Schultz. *Polymer Materials Science*, page 466. Prentice Hall, Inc., Englewood Cliffs, NJ, 1974.

[186] I. Dobovsek. Some aspects of shear yielding and emergence of shear bands in solid polymers. *Acta Physica Polonica A*, 128(4):619–623, October 2015.

[187] S. L. Bazhenov, A. V. Efimov, I. V. Sosnovskii, A. V. Bol'shakova, A. S. Kecheck'yan, and A. L. Volynskii. Formation of shear bands in amorphous polyethylene terephthalate films while rolling. *Doklady Physical Chemistry*, 463(1):158–160, August 2015.

List of Figures

List of Tables

8 Appendix

8.1 Appendix 1: List of symbols and abbreviations

The list of units, symbols, and the list of abbreviations are in alphabetical order.

Unit symbol	Unit
%:	per cent
°:	degree
°C:	degree Celsius
A:	ampere
A:	average area of the cross section
a1,a2:	unit vectors of graphene lattice
ch:	lattice vector of graphene
cP:	centi Poise
e,q:	elementary charge
eV:	electron volt
ε:	strain
$\Delta\varepsilon$:	strain change
F:	Farad
g:	gram

Unit symbol	Unit
H:	Henry
hr:	hour
Hz:	Hertz
J:	current density
J:	joule
k:	Boltzmann's constant
K:	kelvin
kg:	kilogram
L:	litre
L:	length of a shape
m:	metre
min:	minute
mL:	mililitre
mN:	milinewton
N:	newton
nm:	nanometer
η:	viscosity
p:	pressure
P:	Poise
ρ:	resistivity
Pa:	pascal
σ:	surface tension
ppm:	parts per million
R:	resistance
R_0:	initial resistance
ΔR:	change in resistance

Unit symbol	Unit
s:	second
σ:	conductivity
T:	temperature
µm:	micrometer or micron
V:	volt
ν:	Poisson's ratio
W:	watt
Ω:	Ohm

Abbreviations	Full name
AC:	alternating current
AFM:	atomic force microscope or atomic force microscopy
AgNP:	silver nanoparticle
Aspect ratio:	width/height ratio of a shape
Av.:	Average
BET:	Brunauer-Emmett-Teller
CAD:	computer-aided design
CNT:	carbon nanotube
CTAB:	hexadecyl trimethylammonium bromide
CVD:	chemical vapor deposition
DC:	direct current
DI:	de-ionized
DoD:	drop-on-demand or droplet-on-demand
DTAB:	dodecyl trimethylammonium bromide
DUT:	device-under-test

Abbreviations	Full name
DWCNT:	double-walled carbon nanotube or double-wall carbon nanotube
EM:	electron microscope or electron microscopy
E-skin:	electronic skin
FIB:	focused ion beam
GF:	gauge factor
HCF:	high cycle fatigue
HIM:	helium ion microscope or helium ion microscopy
HMI:	human-machine interface
ICP:	intrinsic conductive polymer
ITO:	indium tin oxide
IJ:	inkjet
Kapton:	commercial name of polyimide
LabVIEW:	Laboratory Virtual Instrumentation Engineering Workbench
LCF:	low cycle fatigue
LED:	light emitting diode
LV-SEM:	low voltage scanning electron microscope
MATLAB:	numerical computing environment developed by MathWorks
MG:	metallic grid
MNP:	metallic nanoparticle
MNW:	metallic nanowire
MSDS:	material safety data sheet
MWCNT:	multi-walled carbon nanotube or multi-wall carbon nanotube
NP:	nanoparticle

Abbreviations	Full name
NW:	nanowire
OLED:	organic light emitting diode
PCB:	printed circuit board
PDMS:	polydimethylsiloxane
PECVD:	plasma enhanced chemical vapor deposition
PEDOT:PSS:	poly(3,4-ethylenedioxythiophene) polystyrene sulfonate
PET:	polyethylene terephthalate
PEN:	polyethylene naphthalate
PI:	polyimide
PTFE:	polytetrafluoretyhylene
PU:	polyurethane
PVD:	physical vapor deposition
RBM:	radial breathing mode
R2R:	roll-to-roll
R-S:	resistance-strain
rpm:	round per minute or revolutions per minute
SEM:	scanning electron microscope or scanning electron microscopy
SWCNT:	single-walled carbon nanotube or single-wall carbon nanotube
SMD:	surface mount device
SDBS:	sodium dodecyl benzenesulfonate
SDS:	sodium dodecyl sulfate
Std.:	Standard
TEM:	transmission electron microscope or transmission electron microscopy
TFE:	thin-film electrode

Abbreviations	Full name
TFT:	thin-film transistor
TLD:	through-the-lens-detector
TPU:	thermoplastic urethane
Triton X-100:	octyl phenol ethoxylate
wt%:	percent in weight or weight percentage
XRD:	x-ray diffraction

8.2 Appendix 2: Used raw materials, chemicals, instruments and equipment

Table 8.1: Used raw materials and chemicals

Name	Supplier
MWCNTs: NC7000™	Nanocyl S.A., Belgium.
Aquacyl™ AQ0101	Nanocyl S.A., Belgium.
Triton™ X-100	Sigma-Aldrich, USA.
SDS	Sigma-Aldrich, USA.
SDBS	Sigma-Aldrich, USA.

Table 8.2: Used instruments and equipment

Type	Model and Brand
Inkjet printer	AD-P-8000, Microdrop, Germany.
Printhead	MD-K-140, Microdrop, Germany.
Horn-sonicator	Sonopuls HD2200, Bandelin, Germany.
Spin-coater	CPS10, Semitec, Germany.

Type	Model and Brand
Rheometer	Physica MCR300, Anton Paar, Austria.
Tensiometer	K100, Kruss GmbH, Germany.
Raman spectrometer	LabRAM HR Evolution, Horiba, Japan.
Laser scattering spectroscopy	Patrica LA-950, Horiba, Japan.
3D confocal laser scattering microscope	VK-9710K, Keyence, Japan.
Four-point probe	Jandel, Bridge Technologies, USA.
Nanovolmeter	2182A, Keithley Instruments, USA.
Precision current source	6220, Keithley Instruments, USA.
Linear nano-translational stage	M-112.1VG, PI, Germany.
SEM/FIB	Nova Nanolab 200, FEI, USA.
HIM	Orion NanoFab, Carl Zeiss, Germany.

8.3 Appendix 3: Datasheet of Melinex® ST504/ST506 PET Films

Melinex® ST504 is only one-side treated, whereas Melinex® ST506 is both-side treated. Both types of films are available in thickness of 125 μm, 175 μm, and 250 μm. The typical values of the properties for both types of films are given in Table 8.3. Many values are important references for technical reasons and relevant to the experimental procedure and data in this work.

Table 8.3: Typical values of properties of PET substrates

Property	**Test Method**	**Unit**	**Value**
Melting point	BS2782	°C	255
Coefficient of thermal expansion (between 20 and 50 °C)		cm/cm deg C	19×10^{-6} (MD)
Residual Shrinkage (after 30mins at 150 °C)		%	MD 0.10 TD 0.03
Haze	ASTM D 1003-78	%	1.0
Total Light Transmission	ASTM D1003	%	>85
Gloss 60°	ASTM D523		150
Dielectric strength	ASTM D149	Kv/mm	105
Dielectric constant	ASTM D150	2.9	
Volume resistivity	ASTM D257	ohm m	10^{15}
Area yield		m2/kg	5.72
Relative Density	ASTM D1505-79	kgf/mm2	1.39
Tensile strength at break	ASTM D882-83	per 1% RH	>17.7->14.1
Flexural strength (MIT fold)	ASTM D2176		<20,000
Water vapour permeability 38°C/90%rh			4.0
Coefficient of hygroscopic expansion			8×10^{-6}
Elongation at break	ASTM D882-83	%	MD 96, TD 126
F5 (force to elongate 5% of gauge length)	ASTM D882	kgf/mm2	MD 10, TD:10.2

8.4 Appendix 4: IPC-TM-650 Test Methods Manual

The bending fatigue tester is designed based on the IPC-TM-650 test method (TM 2.4.3E). The detailed test principles and apparatus design recommended from the "IPC–Association Connecting Electronics Industries®" is given here.

1 Scope To determine the number of flexes to conductor failure of etched flexible printed board conductor patterns.

2 Applicable Documents None

3 Test Specimen The test specimen **shall** consist of an etched conductor pattern in accordance with Figure 1. A minimum of six specimens with the long dimension of the conductors oriented in the transverse direction of the base material **shall** be prepared using standard commercial practices.

For double-sided clad constructions, a separate sample specimen **shall** be prepared for each side. The opposite (untested) side **shall** be completely etched of copper.

4 Apparatus Flexural Endurance Tester (see Figure 2) or equivalent.

5 Procedures

5.1 Examine the etched conductor specimen for any preexisting fractures and look for evidence of process anomalies (such as pin holes and nicks), which could cause premature fracture. If such fractures or anomalies are found, the specimen **shall** be discarded and a new specimen selected.

5.2 Attach (solder, clamp, etc.) a short length of insulated wire to the extreme ends of the conductor pattern of each of the six specimens.

5.3 Using the flexure test equipment as seen in Figure 2, mount the specimen so that the inside diameter of the loop is

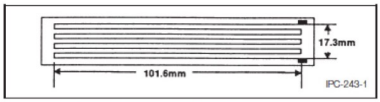

Figure 1 Flexural Endurance Test Pattern.
(NOTE: Conductors are 1.5 mm ± 0.1 mm [approximately, 0.059 in ± 0.004 in] wide on 2.5 mm ± 0.1 mm [approximately, 0.01 in ± 0.004 in] centers.)

6 mm ± 1 mm [approximately, 0.25 in ± 0.04 in] and connect the two wires to the relay. The horizontal oscillation of the reciprocating bar causes the flexible test specimen to move in what can be described as a rolling, flexible action.

5.4 Test three specimens per clad side with the conductor on the inside of the loop. The reciprocating travel should not exceed 10 cycles per minute. The loop **shall** travel 25 mm ± 5 mm [effectively, 1 in ± 0.2 in].

5.5 The number of cycles to failure is when electrical discontinuity of the conductor occurs.

5.6 Report the average number of cycles to failure for the three specimens tested per clad side.

6 Note Master set of drawings of a similar test fixture as seen in Figure 2 is available from the IPC office. This fixture is not commercially available.

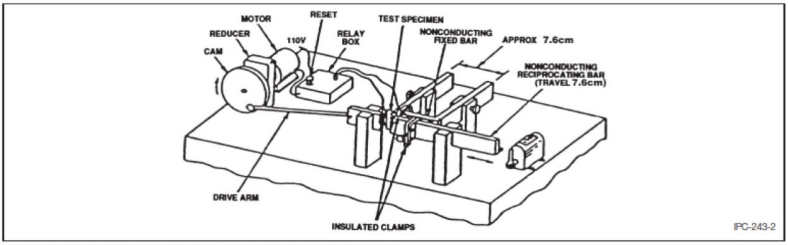

Figure 2 Typical Flexural Endurance Test Fixture Equipment

8.5 Appendix 5: Look-up table of the bending strain

Table 8.4: A look-up table of the bending strain as a function of the gap distance

Strain amplitude	Gap distance (in mm) for substrates with thickness of:		
%	125µm	175µm	250µm
0.10	125	175	250
0.20	62.5	87.5	125
0.50	25	35	50
1.00	12.5	17.5	25
1.50	8.333333333	11.66666667	16.66666667
2.00	6.25	8.75	12.5
3.00	4.166666667	5.833333333	8.333333333
4.00	3.125	4.375	6.25
5.00	2.5	3.5	5
6.00	2.083333333	2.916666667	4.166666667
7.00	1.785714286	2.5	3.571428571
8.00	1.5625	2.1875	3.125
9.00	1.388888889	1.944444444	2.777777778
10.00	1.25	1.75	2.5

8.6 Appendix 6: CAD-models of the custom-made and the commercial tensile stage

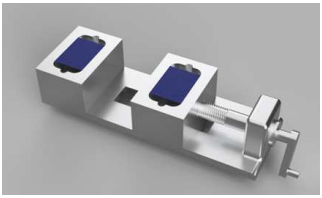

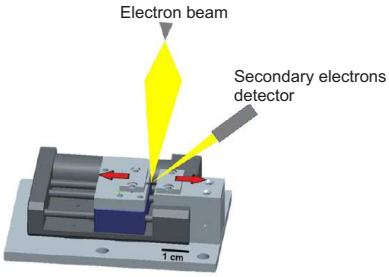

Figure 8.1: CAD-models of (top) the custom-made manual tensile stage for re-loading the sample inside the SEM, and (bottom) the micro-translation stage (M-112.1VG, PI GmbH, Germany) featuring a linear servo motor for the *in-situ* micro-tensile testing inside the SEM.